MAG. RER. NAT. DARJAN KOZIC

# QUANTIFICATION OF THE MATERIAL INHOMOGENEITY EFFECT IN THIN METALLIC FILM STACKS

MONTANUNIVERSITÄT LEOBEN

# QUANTIFICATION OF THE MATERIAL INHOMOGENEITY EFFECT IN THIN METALLIC FILM STACKS

MAG. RER. NAT. DARJAN KOZIC

November 2017

Materials Center Leoben Forschung GmbH
Roseggerstrasse 12
A-8700 Leoben

# AFFIDATIV

I declare in lieu of oath, that I wrote this thesis and performed the associated research by my self, using only literature cited in this document.

*Leoben, November 2017*

Darjan Kozic

*Dedicated to Eva and my parents.*

*You must let what happens happen. Everything must be equal in your eyes,*
*good and evil, beautiful and ugly, foolish and wise.*

— Michael Ende

# ACKNOWLEDGMENTS

---

This thesis was conducted in the years between 2013 and 2017 during my occupation at the Materials Center Leoben (MCL) Forschung GmbH. I greatfully acknowledge the funding by the Austrian Federal Government and the Styrian Provincial Government within the research activities of the COMET K2 Competence Center MPPE (Project A7.17).

I would like to express my gratitude to my supervisor Prof. Thomas Antretter from the Institute of Mechanics at the Montanuniversität Leoben for the possibility to work as his PhD student, his excellent support and valuable advice.

Furthermore, I would like to thank my former superior Dr. Ronald Schöngrundner for his dedication and guidance throughout my first years at the MCL. I express the same gratitude towards my colleague Dr. Hans-Peter Gänser, who was always willing to discuss my questions, helping to cope with organizational difficulties and encouraging a likeable atmosphere. In the same context, I would like to thank Priv. Doz. Dr. Roland Brunner and assoz. Prof. Daniel Kiener for their support and valuable discussions.

I dedicate a special thanks to my former colleague Walter Ochensberger and some further colleagues at the MCL, Masoud Sistaninia and René Hammer. Through the on- and off-topic discussions during the enjoyable coffee and tea breaks we were able to grow a personal relationship. In addition, I want to thank Dr. Werner Ecker for the opportunity to work and continue working in his group. Last but not least, I very much appreciate the support of my current superior Prof. Otmar Kolednik.

I have the privilege to thank all my friends. They have supported and cheered me up in times of desperation, especially Matthias Puhr, Andrea Janics, Harald Ferstl and Robert and Miriam Wimmer-Teubenbacher.

I am very grateful to my parents for the support and possibilities they have given me throughout the course of my life and education. Their trust and caring as well as forthcoming advice was and will always be most valuable to me.

I am especially grateful to my wife Eva for her undisputed support and strength she has given me over the past years. Her friendship, encouragement, belief and affection were the cornerstone for the successful conclusion of my thesis.

# ABSTRACT

This thesis deals with the characterization of thin metallic film systems with respect to their mechanical properties. This incorporates investigations about the intrinsic properties, internal loading conditions and the response to external mechanical loading of the material systems.

Compressive and tensile residual stresses in thin films have implications on the reliability of microelectronic components. Residual stresses can have a negative or a positive effect on the performance and lifetime of the structures. In this thesis, a method is developed to efficiently determine residual stresses in thin films. This is realized by combining micro-mechanical experiments and computational methods. Experimental results, obtained with the so-called Ion beam Layer Removal method, are utilized to inversely determine the residual stresses numerically with finite element simulations or analytically with the Euler-Bernoulli beam theory. It is shown that the residual stresses in various thin film systems can be locally resolved with high precision.

The material behavior of thin films is determined by their size and the internal structure. The nanocrystalline nature of the investigated materials allows for a classical approach to derive the yield and hardening behavior. The force-displacement response from spherical nanoindentation experiments is used in an optimization routine – coupled to finite element analysis – to numerically determine the flow curve of the thin films while also considering the residual stresses. It is shown that the flow behavior of miniaturized materials is different compared to macroscopic or bulk materials.

To describe the fracture behavior of the thin film stacks under external loading, the concept of configurational forces is applied. The investigation is especially focused on the influence of the residual stress state and material properties on the crack driving force. A crack can experience shielding or anti-shielding in the vicinity of an interface. This impact on the crack driving force is described by the interface inhomogeneity term. Another contribution to the term is given by the jump of the residual stress at the interfaces. In addition, the residual stress gradient in the layers further influences the crack driving force. This contribution to the crack driving force is given by the gradient inhomogeneity term.

The mechanical behavior of thin film components has an integral significance for the performance and life span of high-end microelectronic devices. This thesis offers tools for thin film stack characterization which can be readily applied in the design chain of components.

# KURZZUSAMMENFASSUNG

Diese Arbeit beschäftigt sich mit der Bestimmung der mechanischen Eigenschaften von dünnen metalischen Schichtsystemen. Dies beinhaltet Untersuchungen der Materialsysteme in Bezug auf ihre intrinsischen Eigenschaften, interne Belastungen und die Reaktion auf externe Belastungen.

Druck- und Zugeigenspannungen in dünnen Schichten beeinflussen die Zuverlässigkeit von mikroelektronischen Komponenten. Eigenspannungen können sowohl einen negativen als auch einen positiven Effekt auf die Leistungsfähigkeit und Lebensdauer der Strukturen haben. In dieser Arbeit wird eine Methode entwickelt, mit der man die Eigenspannungen in dünnen Schichten effektiv bestimmen kann. Um dies zu realisieren, werden mikromechanische Experimente und Rechenmethoden kombiniert. Experimentelle Ergebnisse der sogenannten Ion beam Layer Removal Methode werden herangezogen, um invers die Eigenspannungen numerisch, mit Hilfe von Finite Elemente Simulationen, oder analytisch, nach der Euler-Bernoulli Balkentheorie, zu bestimmen. Es wird gezeigt, dass die Eigenspannungen in verschiedenen dünnen Schichtsystemen mit hoher Genauigkeit lokal aufgelöst werden können.

Das Materialverhalten von dünnen Schichten ist durch ihre Dicke und Mikrostruktur bestimmt. Da die untersuchten Materialien nanokristallin sind, kann das Fließ- und Verfestigungsverhalten mit einem klassischen Zugang abgeleitet werden. Dabei wird das Kraft-Verschiebungs Verhalten aus sphärischen Nanoindentierungsexperimenten in einer Optimierungsroutine – die an eine Finite Elemente Analyse gekoppelt ist – benutzt, um die Fließkurve der dünnen Schichten numerisch zu bestimmen, wobei die Eigenspannungen mitberücksichtigt werden. Es wird gezeigt, dass sich das Fließverhalten von miniaturisierten Materialien von dem der makroskopischen oder Bulk-Materialien unterscheidet.

Um das Bruchverhalten in den dünnen Schichtsystemen zu beschreiben, wird das Konzept der Configurational Forces herangezogen. Das Hauptaugenmerk liegt besonders in der Untersuchung vom Einfluss der Eigenspannungen und des Materialverhaltens auf die risstreibende Kraft. Ein Riss kann von einer Grenzfläche abgeschirmt oder angezogen werden. Die Auswirkung auf die risstreibende Kraft wird durch den Grenzflächeninhomogenitätsterm beschrieben. Der Sprung der Eigenspannungen an den Grenzflächen macht einen zusätzlichen Beitrag zu diesem Term aus. Weiters beeinflusst der Eigenspannungsgradient innerhalb der Schichten die risstreibende Kraft. Dieser Beitrag zur risstreibenden Kraft ist durch den Gradiententerm gegeben.

Das mechanische Verhalten von Dünnschichtkomponenten trägt wesentlich zur Leistungsfähigkeit und Lebensspanne von Highend-Mikroelektronikgeräten bei. Das in dieser Arbeit präsentierte Konzept stellt ein Werkzeug für die Charakterisierung von Dünnschichtsystemen dar, welches in der Designkette von Komponenten eingesetzt werden kann.

# PUBLICATIONS

Parts of the work presented in this thesis were already investigated and published in research papers or conference proceedings. In the following, the concerning publications are listed:

[1] D. Kozic, H.-P. Gänser, R. Brunner, D. Kiener, T. Antretter, and O. Kolednik. "Crack arresting abilities of thin metalic films stacks due to the influence of material and residual stress inhomogeneities." In: *TBA* (2018).

[2] D. Kozic, V. Maier-Kiener, R. Konetschnik, H.-P. Gänser, T. Antretter, R. Brunner, and D. Kiener. "Extracting flow curves from nano-sized metal layers in thin film systems." In: *Scripta Materialia* 130 (2017), pp. 143–147. ISSN: 13596462. DOI: `10.1016/j.scriptamat.2016.11.008`.

[3] D. Kozic, R. Treml, V. Maier-Kiener, R. Schöngrundner, R. Brunner, D. Kiener, T. Antretter, and H.-P. Gänser. "Fracture and material behavior of thin film composites." In: *2016 17th International Conference on Thermal, Mechanical and Multi-Physics Simulation and Experiments in Microelectronics and Microsystems, EuroSimE 2016*. 2016. ISBN: 9781509021062. DOI: `10.1109/EuroSimE.2016.7463352`.

[4] R. Treml, D. Kozic, J. Zechner, X. Maeder, B. Sartory, H. P. Gänser, R. Schöngrundner, J. Michler, R. Brunner, and D. Kiener. "High resolution determination of local residual stress gradients in single- and multilayer thin film systems." In: *Acta Materialia* 103 (2016), pp. 616–623. DOI: `10.1016/j.actamat.2015.10.044`.

[5] R. Treml, D. Kozic, R. Schöngrundner, O. Kolednik, H.-P. Gänser, R. Brunner, and D. Kiener. "Miniaturized fracture experiments to determine the toughness of individual films in a multilayer system." In: *Extreme Mechanics Letters* 8 (2016), pp. 235–244. ISSN: 23524316. DOI: `10.1016/j.eml.2016.01.004`.

[6] D. Kozic, R. Treml, R. Schöngrundner, R. Brunner, D. Kiener, J. Zechner, T. Antretter, and H.-P. Gänser. "Fracture mechanics of thin film systems on the sub-micron scale." In: *2015 16th International Conference on Thermal, Mechanical and Multi-Physics Simulation and Experiments in Microelectronics and Microsystems, EuroSimE 2015*. 2015. ISBN: 9781479999507. DOI: `10.1109/EuroSimE.2015.7103088`.

[7] D. Kozic, R. Treml, R. Schöngrundner, R. Brunner, D. Kiener, T. Antretter, and H.-P. Gänser. "Evaluation of the residual stress distribution in thin films by means of the ion beam layer removal method." In: *2014 15th International Conference on*

*Thermal, Mechanical and Multi-Physics Simulation and Experiments in Microelectronics and Microsystems, EuroSimE 2014*. 2014. ISBN: 9781479947904. DOI: 10.1109/EuroSimE.2014.6813785.

[8] R. Schöngrundner, R. Treml, T. Antretter, D. Kozic, W. Ecker, D. Kiener, and R. Brunner. "Critical assessment of the determination of residual stress profiles in thin films by means of the ion beam layer removal method." In: *Thin Solid Films* 564 (2014), pp. 321–330. DOI: 10.1016/j.tsf.2014.06.003.

# CONTENTS

# Part I

# PREAMBLE

# 1

# INTRODUCTION

Since Moore's law was postulated in the late 60's, [1], the microelectronics (ME) industry is driven by the idea to regularly increase the number of components in an integrated curcuit (IC) by a factor of two, while reducing the costs to a minimum. The goal is to accomplish this every $12 - 24$ months. Lately, this time interval has increased to approximately 30 months, as the silicon based technology is slowly reaching its saturation limit. Meanwhile, the integration has extended into the $3^{rd}$ dimension and the number of components per 3D IC is still increasing, making the complexity of the embedded components very high. In this context, the era of Moore's law has transitioned into the often mentioned era called "More Than Moore", see e. g. [2].

In addition, the manufacturers are currently focused on increasing the versatility of 3D ICs. During its lifetime, a ME device has to perform reliably under different conditions while fulfilling its many designated functions. The response of components to environmental influences is one of the key issues concerning the reliability of the device. Such components incorporate various miniaturized materials with a wide span of material properties. The combination of thin metallic films, ceramics for isolation purposes and bonding materials is creating a complex environment. The electronic, magnetic and optical properties of the used materials have been extensively investigated. On the other hand, the mechanical properties of the materials and their composites have often been disregarded.

The fabrication process of 3D ICs is a good example where significant straining emerges which can lead to device failure. The strains result in different types of stresses, such as residual stresses due to the deposition process, thermal strains due to deposition at elevated temperatures and subsequent cooling or external stresses caused in the process of embedding. The proper knowledge about the magnitude and distribution of the stress state is necessary when investigating the failure behavior of a component.

The embedded materials, e. g. thin films, also differ with respect to their stress-strain behavior. Moreover, the individual materials behave in a different fashion if compared to conventional or bulk materials. This is caused by the variation of the internal structure, such as grain size and their distribution, and external dimensions, e. g. the film thickness. As the failure behavior of a component is also determined by the properties of the used materials, their stress-strain relation has to be properly determined. This means that conventional methods which yield a linear elastic material behavior have to be reconsidered and extended or replaced by methods that determine elastic–plastic properties.

Finally, the failure behavior of the components has to be quantitatively described. The loading parameter that describes the fracture behavior of a body incorporating material inconsistencies, such as cracks, is called crack driving force, see e. g. [3]. Unlike in homogeneous bodies, the crack driving force in multi-material components does not only depend on the externally applied load [4, 5]. Internal loading conditions, such as residual stresses, govern additional contributions to the overall crack driving force. Additionally, the material properties determine how a crack behaves at the transition from one material to the other. In any case, a crack can be prevented from propagation or, on the other hand, accelerated to extend even faster. In order to determine the crack driving force in elastic–plastic inhomogeneous structures, conventional methods have to be replaced with more sophisticated approaches.

In this work, the problems concerning the mechanical behavior of thin metallic film stacks are investigated. By developing appropriate analytical and numerical tools the failure behavior in such material systems can be quantitatively determined.

This thesis is structured in the following way: In the remainder of Part i the basics of continuum mechanics and fracture mechanics are explained and a short introduction to the concept of configurational forces is given. In addition, the composition of the investigated thin film stacks is presented. After that, the emergence and calculation of residual stresses in layered structures is explained in Part ii. Simple model materials are examined before the residual stress distributions are calculated for more sophisticated material combinations. Part iii is dedicated to the investigation of the stress-strain behavior of the thin films. This is focused on how to determine the flow curve of the given materials. The yield and hardening behavior is critically discussed and compared with results from other investigations. Based on the results from Part ii and Part iii, the fracture behavior in the thin film stacks is subsequently determined in Part iv. The numerical implementation of the configurational force concept is explained before the finite element model for the material systems is introduced. The discussion is focused on the implications of the material inhomogeneities, i. e. the residual stress distribution and material arrangement, on the crack driving force. Finally, Part v gives a general conclusion of the thesis followed by an outlook.

# 2

# SHORT INTRODUCTION TO CONTINUUM MECHANICS

The branch of continuum mechanics is concerned with the deformation of solids, liquids and gases subjected to stress. This thesis is focused on the description of solid continua, where the theories of elasticity and plasticity allow for an adequate description of the stress and deformation behavior of most engineering materials, such as metals.

The plain fundamentals of continuum mechanics which are needed in the course of the thesis shall be introduced in this chapter. For the sake of simplicity, detailed derivations of equations are omitted. For extensive explanations and calculations the reader is referred to the books of Bonet and Wood [6], Chadwick [7] or Malvern [8]. This chapter is mainly following the structure and language of Bonet and Wood [6].

## 2.1 DEFORMATION GRADIENT

Imagine a body $\mathcal{B}_0$ in its initial state at time $t_0$, as shown in Figure 1. The body $\mathcal{B}_0$ is a set of material points which are described by the coordinates $\mathbf{X}$, with respect to the Cartesian basis $X_i$. If the body $\mathcal{B}_0$ is in some way subjected to internal or external loading it will deform into the body $\mathcal{B}$ (see Figure 1). The material points in this body are described by the coordinates of an another Cartesian basis $x_i$. As shown in Figure 1, the initial as well as the deformed form of a body are represented by identical coordinate systems, i. e. $X_i$ and $x_i$, where $i = 1, 2, 3$. From now on, we refer to $x_i$ as the global coordinate system.

In finite deformation analysis, it is very important to make a precise distinction between a configuration before deformation $(\mathcal{B}_0)$ and a configuration during or after deformation $(\mathcal{B})$. Reference to the latter or current configuration of the body is also often referred to as the spatial or *Eulerian* description and reference to the former or reference configuration is also called the material or *Lagrangian* description. The reference description refers to the behavior of a material point. The current description, on the other hand, refers to the behavior at a spatial position, see [6].

The motion can be described as a nonlinear one-to-one mapping between the initial and current material point position,

$$\mathbf{x} = \mathbf{x}\,(\mathbf{X}, t)\,. \tag{1}$$

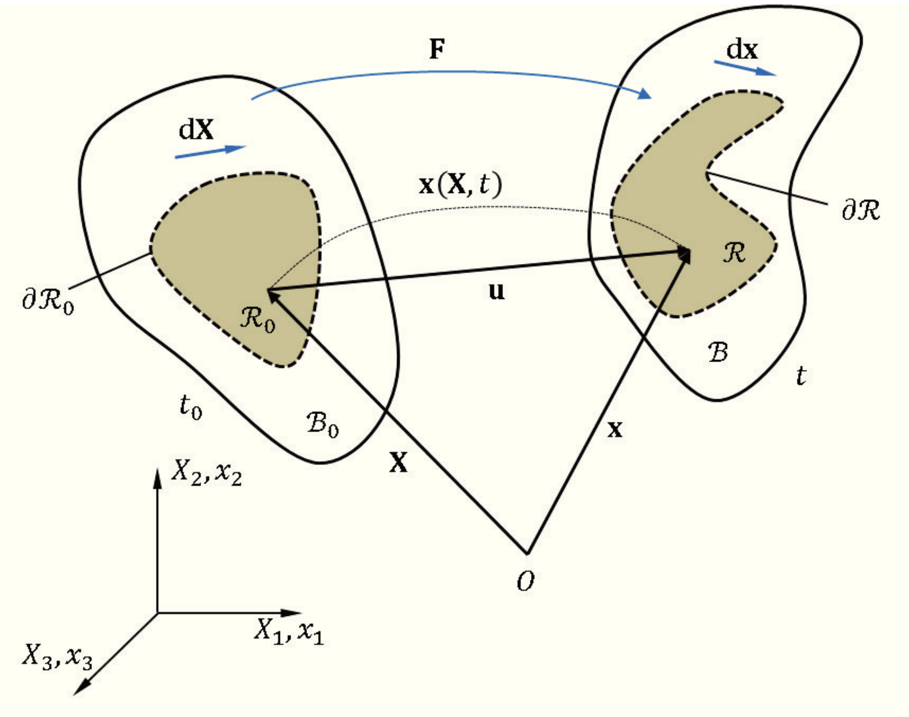

Figure 1: Reference configuration $\mathcal{B}_0$ and current configuration $\mathcal{B}$. A material point at the position $\mathbf{X}$ of $\mathcal{B}_0$ is projected at time $t$ into its current position $\mathbf{x}$ of $\mathcal{B}$ by the nonlinear mapping $\mathbf{x} = \mathbf{x}\,(\mathbf{X}, t)$. Additionally, the deformation gradient $\mathbf{F}$ maps line elements from $\mathcal{B}_0$ into tangent vectors of $\mathcal{B}$, given by Equation 3.

For a constant value of $t$, Equation 1 is a mapping between the reference and current description of the bodies. If, however, the particle position $\mathbf{X}$ is fixed, Equation 1 describes the time dependent motion of this material point.

Just like the material point positions in the deformed and undeformed body can be related, also the distance between two neighboring points in the current $(d\mathbf{x})$ and reference $(d\mathbf{X})$ configuration can be related to each other, as shown in Figure 1. This is accomplished by introducing the deformation gradient $\mathbf{F}$, which is defined as

$$\mathbf{F} = \frac{\partial \mathbf{x}}{\partial \mathbf{X}}. \tag{2}$$

The deformation gradient transforms vectors in the reference configuration into vectors in the current configuration, i. e.

$$d\mathbf{x} = \mathbf{F} d\mathbf{X}. \tag{3}$$

Therefore, $\mathbf{F}$ is a key quantity in finite deformation analysis, as it is involved in all equations relating quantities before and after deformation, see [6]. Also, in finite deformation analysis it does not matter how large the displacement $\mathbf{u} = \mathbf{x} - \mathbf{X}$ is, see Figure 1. It can even exceed the initial dimensions of the body, which is often the case, e. g. in metal forming.

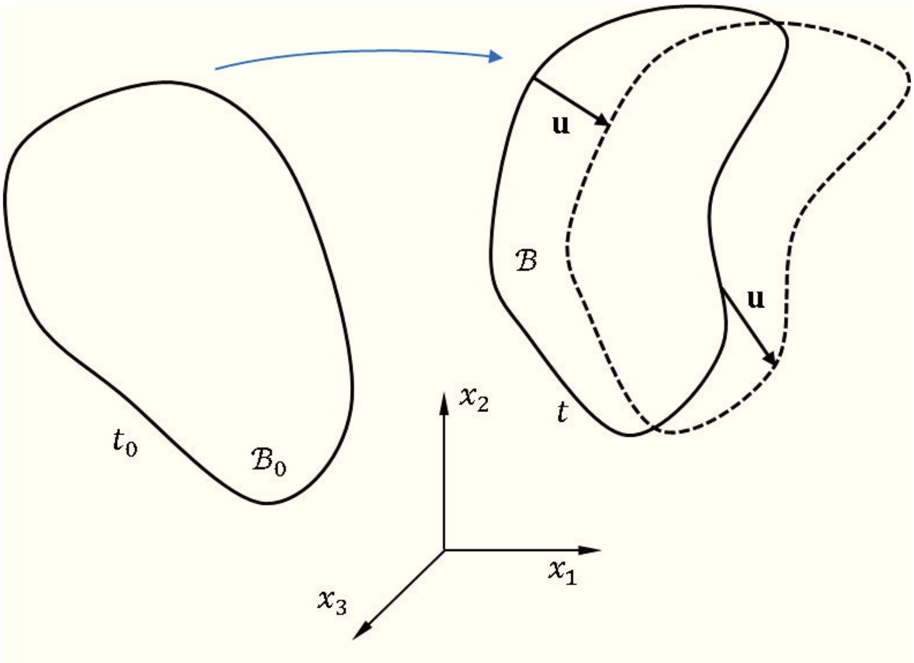

Figure 2: Deformation of the current configuration in the case of small strain theory. Accordingly, the deformation gradient **F** is determined by the displacement field **u**.

In numerical analysis, it is often beneficial or even necessary that linearized equations are used for the calculations. Consider a small displacement **u** from the current configuration $\mathbf{x} = \mathbf{x}(\mathbf{X}, t)$, as shown in Figure 2. It follows that the linearized version of the deformation gradient **F** is

$$\mathbf{F} = \nabla \mathbf{u}, \tag{4}$$

see Bonet and Wood [6] for a detailed derivation.

## 2.2 POLAR DECOMPOSITION AND STRAIN

The meaning of the deformation gradient is further disclosed in terms of its decomposition into stretch and rotation components. The tensor **F** shall be expressed in terms of **R**, which is the rotational tensor and **U** or **V**, denoting the right or left stretch tensor, respectively:

$$\mathbf{F} = \mathbf{R}\mathbf{U} = \mathbf{V}\mathbf{R}. \tag{5}$$

Additionally, the right and left *Cauchy-Green tensors* are defined, respectively:

$$\mathbf{C} = \mathbf{F}^{\mathrm{T}}\mathbf{F}, \tag{6}$$

$$\mathbf{b} = \mathbf{F}\mathbf{F}^{\mathrm{T}}. \tag{7}$$

From Equation 3, it follows that

$$d\mathbf{x} = \mathbf{R}\mathbf{U}d\mathbf{X} = \mathbf{V}\mathbf{R}d\mathbf{X}. \tag{8}$$

It is clear that in Equation 8 $d\mathbf{X}$ is first streched or strained by $\mathbf{U}$ and subseqnently rotated by $\mathbf{R}$ into $d\mathbf{x}$. The transformation $\mathbf{VR}$, however, performs the rotation first and after that the stretch. From the definition of the right *Cauchy-Green tensor* from Equation 6 and the left *Cauchy-Green tensor* from Equation 7 as well as Equation 5, it can be shown that

$$\mathbf{C} = \mathbf{F}^{\mathsf{T}}\mathbf{F} = \mathbf{U}^{\mathsf{T}}\mathbf{R}^{\mathsf{T}}\mathbf{R}\mathbf{U} = \mathbf{U}^2 \tag{9}$$

$$\mathbf{b} = \mathbf{F}\mathbf{F}^{\mathsf{T}} = \mathbf{V}\mathbf{R}\mathbf{R}^{\mathsf{T}}\mathbf{V}^{\mathsf{T}} = \mathbf{V}^2. \tag{10}$$

From Equation 9 and Equation 10 it can be concluded that $\mathbf{C}$ and $\mathbf{b}$ are also measures of the strain, see Bonet and Wood [6]. In an equivalent fashion, Equation 11 proves the same argument,

$$ds^2 - dS^2 = d\mathbf{X}\left(\left(\mathbf{C} - \mathbf{1}\right)d\mathbf{X}\right) = d\mathbf{x}\left(\left(\mathbf{1} - \mathbf{b}^{-1}\right)d\mathbf{x}\right), \tag{11}$$

where, $ds^2$ and $dS^2$ are the squared lengths of the linear elements at $\mathbf{x}$ and $\mathbf{X}$, respectively. The tensors

$$\mathbf{E} = \frac{1}{2}\left(\mathbf{C} - \mathbf{1}\right), \tag{12}$$

$$\mathbf{e} = \frac{1}{2}\left(\mathbf{1} - \mathbf{b}^{-1}\right), \tag{13}$$

are called the *Lagrangian strain tensor* or *reference strain tensor* and *Eulerian strain tensor* or *spatial strain tensor*, respectively.

Equivalently to the linearization of the deformation gradient in Equation 4, e. g. also the *Lagrangian strain* can be linearized, see [6] for a detailed derivation,

$$\varepsilon = \frac{1}{2}\left(\nabla\mathbf{u} + \left(\nabla\mathbf{u}\right)^{\mathsf{T}}\right). \tag{14}$$

Since the current and reference configuration are represented in the same coordinate system in this thesis, the linearized *Eulerian strain* is equal to the linearized *Lagrangian strain*.

## 2.3 STRESS

Consider the body $\mathcal{B}$ from Figure 1 which is in its current configuration. Figure 3a shows a cut, performed on the body $\mathcal{B}$. A point on the infinitesimally small area element $da$ with its outward normal vector $\mathbf{n}$ is exposed to a traction vector $\mathbf{t}$, which is defined as

$$\mathbf{t} = \lim_{da \to 0} \frac{d\mathbf{p}}{da}, \tag{15}$$

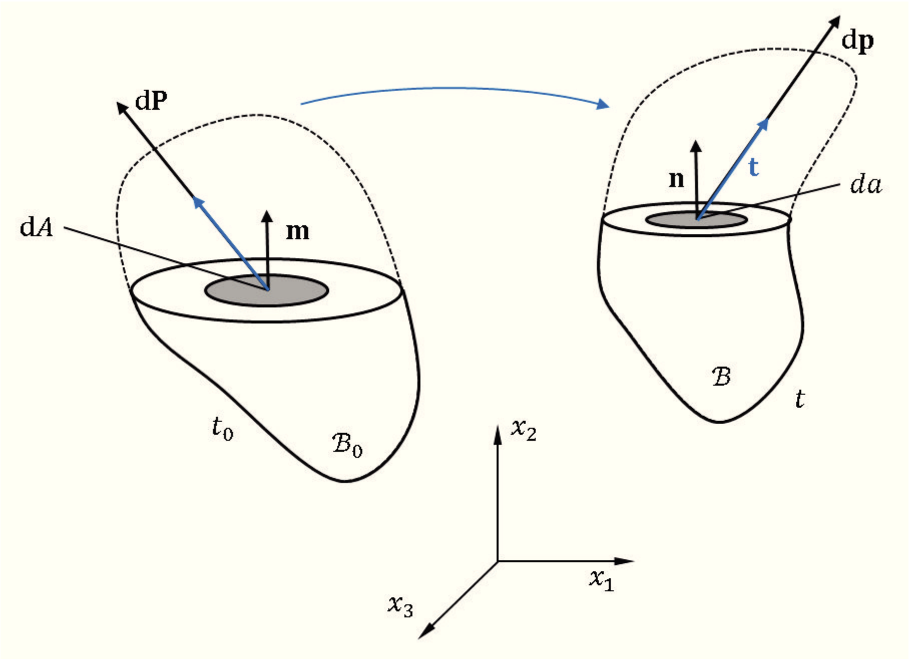

(a) Cut bodies, $\mathcal{B}_0$ in the reference configuration and $\mathcal{B}$ in the current configuration, to showcase the traction on the respective infinitesimally small area elements $dA$ and $da$.

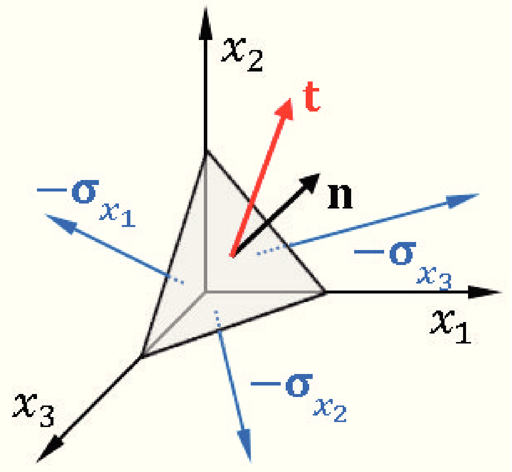

(b) Cauchy tetrahedron with **t** acting on the surface.

Figure 3: Representation of the traction vector **t** from which the Cauchy stress tensor $\boldsymbol{\sigma}$ is derived.

where $d\mathbf{p}$ is the reaction force acting on $da$. The presence of a bulk stress tensor arises from the balance of deformational forces around a material point on the elemental tetrahedron as shown in Figure 3b. Here, three linearly independent cuts are performed around a material point. The traction vector **t** acts on the surface. From this equilibrium the Cauchy stress tensor $\boldsymbol{\sigma}$ relates the surface traction vector **t** and the normal vector **n**:

$$\mathbf{t} = \boldsymbol{\sigma}\mathbf{n}. \tag{16}$$

The Cauchy stress tensor acts at a material point in the current configuration. In the course of the thesis, some derivations are performed with a different stress measure, which relates the element force vector $d\mathbf{p}$ to the reference area element $dA$ in body $\mathcal{B}_0$, as shown in Figure 3a. The resulting traction vector is $\mathbf{s} = \mathbf{S}\mathbf{m}$, whereby $\mathbf{m}$ is the normal to $dA$. $\mathbf{s}$ is the so-called $1^{st}$ Piola-Kirchhoff traction vector and $\mathbf{S}$ is called $1^{st}$ Piola-Kirchhoff stress tensor which is derived from the Cauchy stress tensor, see Bonet and Wood [6]:

$$\mathbf{S} = J\boldsymbol{\sigma}\mathbf{F}^{-\mathrm{T}}, \tag{17}$$

where

| | |
|---|---|
| $J$ | Jacobian, $\det\mathbf{F}$, |
| $\mathbf{F}^{-\mathrm{T}}$ | Transposed to the inverse of the deformation gradient. |

## 2.4 BALANCE LAWS

This section mainly follows the discussion and derivations from the lecture notes about continuum mechanics, written by Abeyaratne [9].

### 2.4.1 *Conserved quantities*

Consider that $\Omega(\mathcal{R}, t)$ is the value of an extensive physical property associated with a region $\mathcal{R}$ inside the body $\mathcal{B}$ at time $t$, as shown in Figure 4. Under suitable conditions a density $\omega(\mathbf{x}, t)$ of this property can be defined with the relation

$$\Omega(\mathcal{R}, t) = \int_{\mathcal{R}} \omega(\mathbf{x}, t)\, dv, \tag{18}$$

where $dv$ is a volume element of the region $\mathcal{R}$. The quantities which are represented by $\Omega$ are the mass, linear and angular momentum, as well as the energy and entropy inside $\mathcal{R}$. Almost all of the quantities obey the following form

$$\int_{\mathcal{R}} \alpha dv + \int_{\partial\mathcal{R}} \beta da = \frac{d}{dt}\int_{\mathcal{R}} \omega dv, \tag{19}$$

where

| | |
|---|---|
| $\alpha$ | Bulk generation of $\Omega$ at material points in $\mathcal{R}$, |
| $\beta$ | Generation of $\Omega$ at material points on the boundary $\partial\mathcal{R}$, |
| $da$ | Surface element on $\partial\mathcal{R}$. |

An equation like Equation 19 is known as a *global balance law*:

- *Global*, as it is defined for the collection of material points in $\mathcal{R}$, rather than singled out material points.

- *Balance*, as it describes how the rate of increase of the amount of $\Omega$ in $\mathcal{R}$ is *balanced* by the generation of $\Omega$ at material points inside of $\mathcal{R}$ and its surface $\partial\mathcal{R}$.

To be able to perform calculations it is convenient to define *local field equations*. In the following subsections, the focus lies on the definition of the localized versions of the global balance laws. For full derivations, the reader is referred to Abeyaratne [9].

### 2.4.2 *Balance of mass*

The conservation of mass postulates that the mass of any $\mathcal{R}$ does not depend on time or motion. Therefore we can write:

$$\frac{d}{dt}\int_{\mathcal{R}} \rho\left(\mathbf{x}, t\right) dv = 0, \tag{20}$$

where $\rho\left(\mathbf{x}, t\right)$ is the mass density. Equation 20 is the global balance of mass. The local version of Equation 20 or the field equation is written as

$$\dot{\rho} + \rho\nabla\cdot\mathbf{v} = 0, \tag{21}$$

in which $\dot{\rho}$ represents the material time derivative and $\nabla\cdot\mathbf{v}$ is the divergence of the material point velocity.

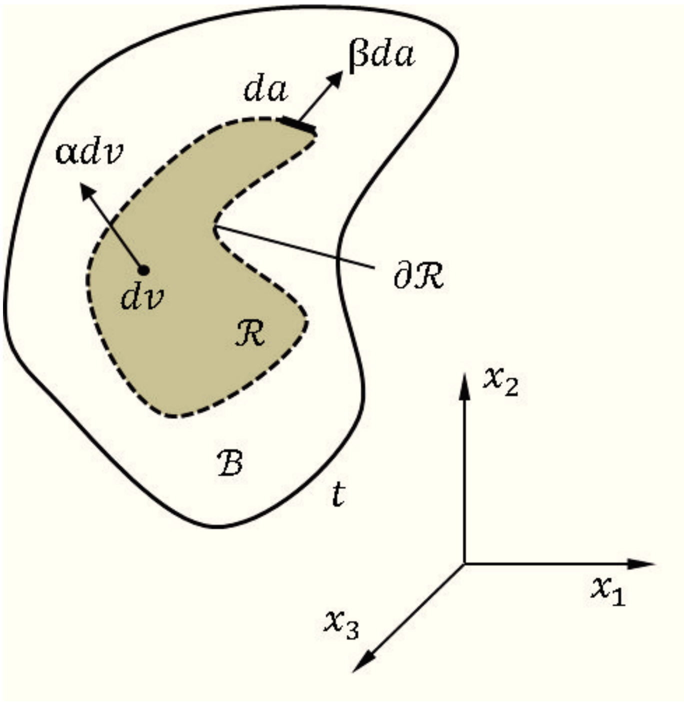

Figure 4: Densities $\alpha$ and $\beta$ which define extensive physical quantities $\Omega$ inside the region $\mathcal{R}$ and on its boundary $\partial\mathcal{R}$, respectively, of a body $\mathcal{B}$.

### 2.4.3 *Specification of a force*

There are two types of forces acting on part $\mathcal{R}$:

- *Body forces* which act at the material points inside of $\mathcal{R}$.
- *Traction forces* which act at the material points on the boundary $\partial\mathcal{R}$.

A force is classified by how it contributes to: 1. the resultant force, 2. the resultant moment around a fixed point and 3. how it performs power. The traction was already defined in Section 2.3. Therefore, the contact force per unit area is denoted by **t** and the contributions corresponding to the list above are:

$$\int_{\partial\mathcal{R}} \mathbf{t} da, \qquad \int_{\partial\mathcal{R}} \mathbf{x}\times\mathbf{t} da, \qquad \int_{\partial\mathcal{R}} \mathbf{t}\cdot\mathbf{v} da, \tag{22}$$

where

$\mathbf{x}$ position,

$\mathbf{v}$ material point velocity.

The body force, on the other hand, shall be denoted with **b** and the following integral terms describe their complete contribution:

$$\int_{\mathcal{R}} \rho\mathbf{b} dv, \qquad \int_{\mathcal{R}} \mathbf{x}\times\rho\mathbf{b} dv, \qquad \int_{\mathcal{R}} \rho\mathbf{b}\cdot\mathbf{v} dv, \tag{23}$$

where $\rho$ is the mass density in the current configuration. In conclusion, the resulting force on $\mathcal{R}$ is

$$\int_{\partial\mathcal{R}} \mathbf{t} da + \int_{\mathcal{R}} \rho\mathbf{b} dv, \tag{24}$$

the resulting moment around a fixed point of the forces is

$$\int_{\partial\mathcal{R}} \mathbf{x}\times\mathbf{t} da + \int_{\mathcal{R}} \mathbf{x}\times\rho\mathbf{b} dv, \tag{25}$$

and the total performed work of the external forces reads

$$\int_{\partial\mathcal{R}} \mathbf{t}\cdot\mathbf{v} da + \int_{\mathcal{R}} \rho\mathbf{b}\cdot\mathbf{v} dv. \tag{26}$$

### 2.4.4 *Balance of linear and angular momentum*

The definition of the balance law of linear momentum requires that in an inertial frame the resultant force on any part of the body equals the rate of increase of its linear momentum. By using Equation 24, the balance law of linear momentum reads

$$\int_{\partial\mathcal{R}} \mathbf{t}da + \int_{\mathcal{R}} \rho\mathbf{b}dv = \frac{\mathrm{d}}{\mathrm{d}t}\int_{\mathcal{R}} \rho\mathbf{v}dv. \tag{27}$$

Equivalently, the conservation of angular momentum in $\mathcal{R}$ is defined as the balance between the resulting moment around a fixed point defined in Equation 25 and the rate of increase of its angular momentum:

$$\int_{\partial\mathcal{R}} \mathbf{x}\times\mathbf{t}da + \int_{\mathcal{R}} \mathbf{x}\times\rho\mathbf{b}dv = \frac{\mathrm{d}}{\mathrm{d}t}\int_{\mathcal{R}} \mathbf{x}\times\rho\mathbf{v}dv. \tag{28}$$

Now consider that the traction vector $\mathbf{t}$ is defined by Equation 16 and that all fields are smooth. Additionally, it follows from the balance of angular momentum that the Cauchy stress tensor $\boldsymbol{\sigma}$ is symmetric, i. e. $\boldsymbol{\sigma} = \boldsymbol{\sigma}^{\mathsf{T}}$. The proof for that is shown in [9] and is not repeated here. Following those requirements, the global balance law of linear momentum from Equation 27 can be written in its local form

$$\nabla\cdot\boldsymbol{\sigma} + \rho\mathbf{b} = \rho\dot{\mathbf{v}}. \tag{29}$$

In a similar fashion, the balance laws can be postulated in terms of the $1^{st}$ Piola-Kirchhoff stress tensor $\mathbf{S}$ as defined in Equation 17 in Section 2.3. For example, the local form of the conservation of linear momentum is written as

$$\nabla\cdot\mathbf{S} + \rho_0\mathbf{b} = \rho_0\dot{\mathbf{v}}, \tag{30}$$

where $\rho_0$ is the mass density of any region $\mathcal{R}_0$ in the body $\mathcal{B}_0$ defined in the reference configuration, see e. g. Figure 3a. In contrast to the Cauchy stress tensor, the $1^{st}$ Piola-Kirchhoff stress tensor is non-symmetric, i. e. $\mathbf{S}\mathbf{F}^{\mathsf{T}} = \mathbf{F}\mathbf{S}^{\mathsf{T}}$.

### 2.4.5 *Conservation of energy – First law of thermodynamics*

As the thermodynamic quantities, which are calculated in the course of the thesis are acting in the reference configuration, the first and second law of thermodynamics are also defined in the reference configuration, in terms of the $1^{st}$ Piola-Kirchhoff stress tensor $\mathbf{S}$.

The first law of thermodynamics states that at each point in time during a motion, the sum of the working rate and the rate of heating on any region $\mathcal{R}_0$ in a body $\mathcal{B}_0$ has to be equal to the rate of increase of the total energy of $\mathcal{R}_0$, see [9]:

$$\int_{\mathcal{R}_0} \mathbf{S}\cdot\dot{\mathbf{F}}dV + \int_{\partial\mathcal{R}_0} \mathbf{q}_0\cdot\mathbf{m}dA + \int_{\mathcal{R}_0} \rho_0 r dV = \int_{\mathcal{R}_0} \rho_0\dot{\gamma}dV, \tag{31}$$

where

| | |
|---|---|
| $\mathbf{S}\cdot\dot{\mathbf{F}}$ | stress power density, |
| $\mathbf{q}_0$ and $r$ | externally supplied heat to $\mathcal{R}_0$, |
| $\dot{\gamma}$ | rate of increase of specific internal energy, |
| $dV$ | volume element of the region $\mathcal{R}_0$, |
| $dA$ | area element on the boundary $\partial\mathcal{R}_0$. |

By applying the divergence theorem to the second term on the left hand side of Equation 31 the conservation law can be written in its localized form

$$\mathbf{S}\cdot\dot{\mathbf{F}} + \nabla\cdot\mathbf{q}_0 + \rho_0 r = \rho_0\dot{\gamma}. \tag{32}$$

### 2.4.6 *Dissipation inequality – Second law of thermodynamics*

The second law of thermodynamics states that at each point in time during a motion, the sum of the rates of entropy flux and entropy supply cannot exceed the rate of increase of the entropy in the region $\mathcal{R}_0$, see [9]:

$$\int_{\mathcal{R}_0} \frac{\rho_0 r}{\theta} \mathrm{d}V + \int_{\partial\mathcal{R}_0} \frac{\mathbf{q}_0\cdot\mathbf{m}}{\theta} dA \leqslant \frac{\mathrm{d}}{\mathrm{d}t}\int_{\mathcal{R}_0} \rho_0\eta \mathrm{d}V, \tag{33}$$

where

| | |
|---|---|
| $\theta$ | absolute temperature, |
| $\eta$ | specific entropy. |

Equation 33 is a form of the *Clausius-Duhem inequality* and it states that the net rate of entropy production or dissipation is larger or equal to zero; thus the name dissipation inequality. Now, the divergence theorem is applied again for the second term on the left hand side of the inequality. Additionally, the Helmholtz free-energy $\phi = \gamma - \eta\theta$ shall be introduced for later purposes, where it is equal to the strain energy density in the model. By utilizing Equation 32, the second law of thermodynamics can be written in the following local form:

$$\mathbf{S}\cdot\dot{\mathbf{F}} - \dot{\phi} \geqslant 0. \tag{34}$$

## 2.5 CONSTITUTIVE EQUATIONS

A constitutive equation relates two physical quantities for a specific material which is subjected to loading. Specifically in this thesis, we are interested in the relation between the stress and strain of solid materials.

### 2.5.1 *Linear elastic materials*

One of the first constitutive relations was introduced by Robert Hooke. Hooke's law describes the stress-strain behavior of a linear elastic material. In a generalized form, the stress components in their respective directions depend on a linear combination of all the strains. In this case the stresses are related to the strains via 81 coefficients. Due to some symmetries this number can be reduced to 21 independent coefficients. In this thesis the materials are assumed to behave isotropic, and for an elastically isotropic material all the coefficients can be expressed in terms of two constants:

| | |
|---|---|
| $E$ | Young's modulus, |
| $\nu$ | Poisson's ratio. |

For a comprehensive study of the constitutive equations for generalized linear elastic materials, the reader is referred to the book of Malvern [8].

### 2.5.2 *Elastic–plastic materials*

The calculations in this thesis are concerning the mechanical behavior of thin metallic films. Thus, this subsection is focusing on the description of plasticity in metals, i. e. metal plasticity. The books of Malvern [8] and Lubliner [10] cover the constitutive behavior of various types of plastically deformable materials, which is not repeated here.

A typical stress-strain diagram for a metal is presented in Figure 5. Theoretically, the material is described by Hooke's law until the elastic limit $\sigma_{el}$ is reached. This value is normally called the yield strength of a material. However, the exact point of yielding is difficult to determine from experiments. In order to perform experiments with reproducible results for the yield strength, the so-called offset yield strength $\sigma_0$ was introduced. The linear part of the original curve is shifted by an offset strain value $\delta$. The point where this parallel line crosses the original curve determines $\sigma_0$. For metals, this value is most commonly chosen to be $\delta = 0.2\%$.

If the material is not strained beyond the yield stress, it returns to its initial state after unloading, i. e. all the strain is recovered. Beyond the point of yielding, most commonly, the stress has to be further increased in order to additionally deform the material. This phenomenon is known as work-hardening or strain-hardening. If the material is loaded up to e. g. point $A$, see Figure 5, a part of the strain or deformation which is accumulated by the material cannot be recovered anymore upon unloading, called the plastic strain $\varepsilon_p$. This strain is acquired by drawing a parallel line to the linear elastic part of the original curve. The plastic strain $\varepsilon_p$ is measured at the point where this line cuts the abscissa. By drawing a line parallel to the ordinate, the remaining or recovered elastic strain $\varepsilon_e$ can be determined, as shown in Figure 5.

In Part iii of the thesis, the material behavior of thin tungsten and copper films is investigated. The stress-strain relation there is given by the well-known Ramberg-Osgood material model [11]:

$$\varepsilon = \frac{\sigma}{E} + \delta \left( \frac{\sigma}{\sigma_0} \right)^m , \tag{35}$$

where

| | |
|---|---|
| $\sigma$ | uniaxial true stress, |
| $\sigma_0$ | offset yield strength, |
| $\varepsilon$ | total strain, |
| $E$ | Young's modulus, |
| $\delta$ | yield offset, |
| $m$ | inverse hardening parameter. |

The Ramberg-Osgood material model is designed to give a continuously rising stress with increasing strain, mainly depending on the hardening parameter. This model is not able to predict an ultimate strength of the material before the point of fracture at high strains. However, for low strains the model gives a reasonable prediction of the resulting flow stresses.

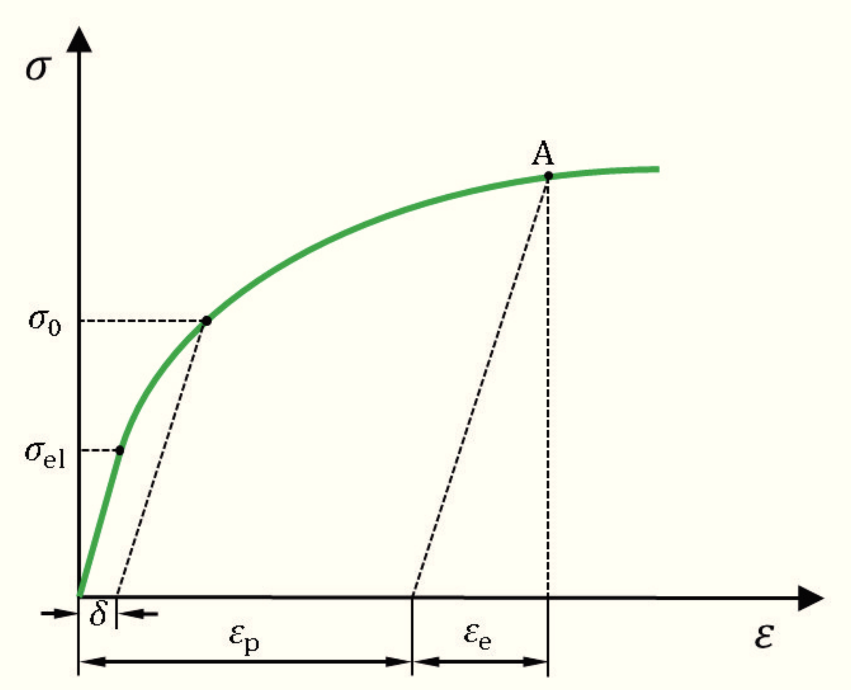

Figure 5: Exemplary tensile stress-strain relation.

# 3

# FUNDAMENTALS OF FRACTURE MECHANICS

Fracture mechanics is based on the tools of continuum mechanics, discussed in the previous chapter. It allows for the description of the behavior of cracks in different types and compositions of materials. The topic of fracture mechanics is one of the most active fields of research and was already extensively investigated in the past. The basics of fracture mechanics are collected in different books and publications, see e. g. [12, 13]. The article by Kolednik, [3], gives a very good overview of fracture mechanics.

In this chapter, the most relevant concepts and terms of fracture mechanics are introduced, to prepare the reader for the discussions in the upcoming parts of this thesis.

## 3.1 DEFINITION OF THE CRACK DRIVING FORCE

Imagine a homogeneous body with an initial crack under loading, as shown in Figure 6. Generally, this crack with an initial length $a_0$ will extend if the crack driving force $D$ equals or exceeds the crack growth resistance $R$ [3, 14]. The crack driving force $D$ describes a loading parameter deduced from the strain energy or the work of applied loading in a body. The crack growth resistance $R$ will prevent crack propagation. It usually depends on the crack extension $\Delta a$ and the geometries of the body, see Figure 6. If $D < R$, the crack will remain stationary. On the contrary, if $D = R$, the crack will exhibit stable growth, and if $D > R$, the crack growth becomes unstable.

As it is suggested in Figure 6, only cracks under *Mode I* loading are investigated in this thesis. This is the crack opening mode and the most critical one, see e. g. [12].

## 3.2 REGIMES OF FRACTURE MECHANICS

In a simple distinction, fracture mechanics can be divided into linear elastic fracture mechanics (LEFM) and elastic–plastic or nonlinear fracture mechanics (E–PFM, NLFM), see e. g. [3]. The concept of LEFM applies if the plastic deformation during crack growth is zero or limited. In this case, the size of the plastic zone $r_{\mathrm{pl}}$ is very small compared to the crack length $a$ and the ligament length $b$, $r_{\mathrm{pl}} << a, b$, in which case *small-scale yielding* (ssy) conditions apply, see Figure 7a. E–PFM, on the other side, is used if the body experiences significant plastic deformation, $r_{\mathrm{pl}} >> a, b$, or, in general, nonlinear behavior. In a homogeneous body with a long crack the prevailing conditions are either

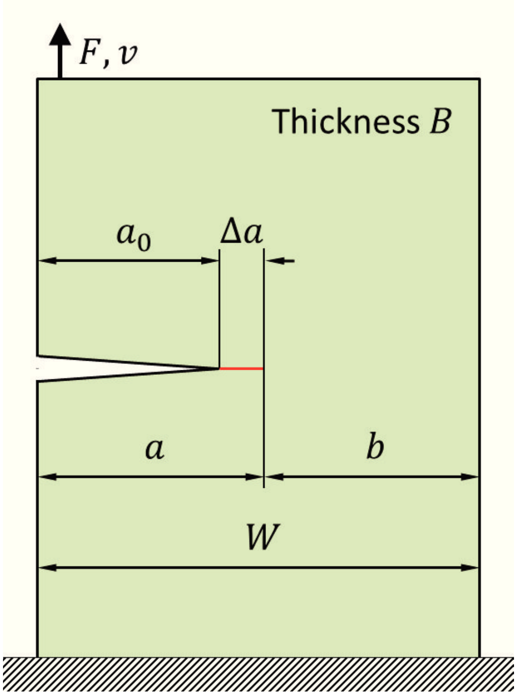

Figure 6: A homogeneous body under *Mode I* loading with its current crack length $a$, ligament length $b$ and width $W$.

large-scale yielding (lsy) or general yielding (gy), as shown in Figure 7b. Under the lsy conditions, the onset of plastic deformation is at the back face of the body, while gy applies when the crack tip plastic zone and back face plasticity merge into one plastic zone. In a special case where the crack is very short, as shown in Figure 7c, E–PFM has to be applied, as also a small plastic zone does not comply with the conditions from Figure 7a. As already mentioned, this thesis is ultimately dealing with the crack driving force in thin metallic film stacks. In a layered composite, as shown in Figure 7c, the materials deform in a different way and often the lsy condition cannot be defined by the onset of back face plasticity. In this case lsy applies if the size of the plastic zone $r_{\mathrm{pl}}$ compares to or is higher than the crack length $a$.

### 3.2.1 *Linear elastic fracture mechanics*

The stresses close to the crack tip of a linear elastic body are calculated by, see [15]

$$\sigma_{ij} = \frac{K}{\sqrt{2\pi r}} f_{ij}\left(\theta\right), \tag{36}$$

with the polar coordinates $(r, \theta)$, the angular stress functions $f_{ij}\left(\theta\right)$ and

$$K = \sigma_{\mathrm{ap}} \sqrt{\pi a} f_{\mathrm{K}}. \tag{37}$$

$K$ describes the intensity of the near-tip field and is therefore called stress intensity factor. It depends on the applied stress $\sigma_{\mathrm{ap}}$ the crack length $a$, and the geometry of

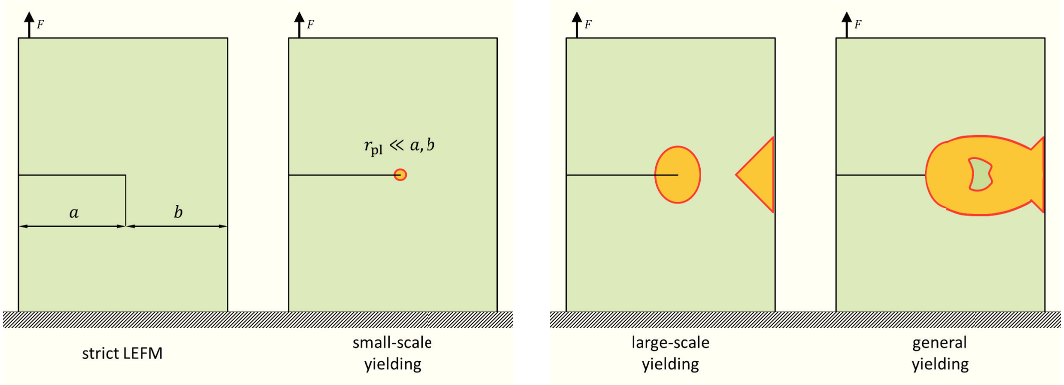

(a) LEFM

(b) E-PFM

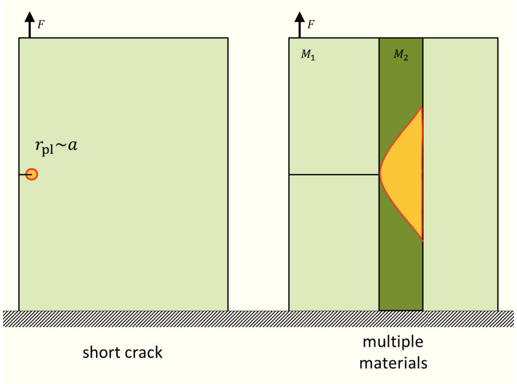

(c) Special cases of E-PFM

Figure 7: Different regimes of fracture mechanics.

the body, represented by $f_K$. However, the equation for the near-tip stresses implies a singular behavior of the stress field, as $r \to 0$, which is not the case in reality. Plastic deformation generated at the crack tip keeps the stresses finite, but for as long as the plastic zone is reasonably small the stress intensity factor $K$ is a valid measure for the crack driving force. Moreover, as the stresses or strains at the crack tip equal or exceed a critical value $K = K_{\text{Ic}}$, fracture occurs. The material parameter $K_{\text{Ic}}$ is called fracture toughness and describes the resistance of the material against fracture. Connecting this stress and strain deformation concept to the energy based perspective of a crack driving force $D$, one finds the relation

$$G = \frac{K^2}{E_b}, \tag{38}$$

where $G$ is the LEFM equivalent to the generalized definition of the crack driving force $D$, called elastic energy release rate, see [16]. $E_b = E/\left(1 - \nu^2\right)$ is the biaxial Young's modulus for plane strain conditions, where $\nu$ is the Poisson's ratio.

### 3.2.2 *Nonlinear and elastic–plastic fracture mechanics*

In the regime where plastic deformation becomes relevant, the concept of LEFM will fail. Therefore, the stress intensity factor $K$ has to be extended into a parameter valid for NLFM and E–PFM. Based on the deformation theory of plasticity, in 1968 a fracture parameter called $J$-integral was introduced by Rice [17]. Similar to $K$, the $J$-integral describes the intensity of the near-tip field and crack growth occurs if the corresponding critical value is reached. The $J$-integral describes a contour integral on an arbitrary path around the crack tip. It was shown by Rice [17], that the $J$-integral is the equivalent to the energy release rate of work done on a nonlinear elastic body containing a crack per unit fracture area. This can be understood as a more generalized version of the elastic energy release rate $G$. For LEFM, the $J$-integral is identical to $G$; consequently, a relationship between the stress intensity factor $K$ and the $J$-integral can be established:

$$J_{\mathrm{el}} = \frac{K^2}{E_{\mathrm{b}}}. \tag{39}$$

There are some limitations concerning the conventional $J$-integral proposed by Rice when applying it to real elastic–plastic materials, pointed out by Simha et al. [18] and Kolednik et al. [19]. The conventional J-integral is based on the theory of plastic deformation, assuming nonlinear elastic behavior for elastic–plastic materials. For non-proportional loading conditions, this theory will predict wrong total strains. For a proper description for elastic–plastic materials incremental theory of plasticity is necessary. Additionally, this nonlinear elastic $J$-integral does not directly describe a crack driving force for real elastic–plastic materials. It acts as a measure of the intensity of the crack tip field, comparable to the stress intensity factor $K$ in LEFM.

## 3.3 CONFIGURATIONAL FORCE CONCEPT AND THE J-INTEGRAL

Material imperfections, smooth or discontinuous material variations as well as residual stresses, are known to have an influence on the crack driving force in a body, see e.g. [4, 5, 19–25]. A very good way to describe the impact of material inhomogeneities on the fracture behavior is provided by the configurational force concept, which is based on the ideas of Eshelby [26], and adopted by Gurtin [27] and Maugin [28]. This concept makes it theoretically possible to describe any kind of inhomogeneous behavior in a body. Examples for inhomogeneities or imperfections in a material are cracks, voids, dislocations and sharp interfaces. In the following, the basic idea of the configurational force concept is given. For comprehensive derivations of the following equations and definitions the reader is referred to [5, 19, 26–28].

From a thermodynamical viewpoint, a configurational force tries to push a defect into a configuration where the total potential energy of the system has its minimum. In general, a configurational force vector **f** can be calculated at each material point in a body. It is defined as the divergence of the configurational stress tensor **C** and becomes non-zero only at positions of a defect in the body:

$$\mathbf{f} = -\nabla \cdot \mathbf{C} = -\nabla \left( \phi \mathbf{I} - \mathbf{F}^{T} \mathbf{S} \right), \tag{40}$$

where

$\phi$ Helmholtz free energy or strain energy density,

$\mathbf{I}$ Identity tensor,

$\mathbf{F}^{T}$ Transposed deformation gradient,

$\mathbf{S}$ 1st Piola-Kirchhoff stress tensor.

If, for example, a two-dimensional homogeneous elastic body with a sharp crack is considered, the crack tip exhibits a configurational force vector $\mathbf{f}_{tip}$, determined by Equation 41

$$\mathbf{f}_{tip} = -\lim_{r \to 0} \int_{\Gamma_r} \left( \phi \mathbf{I} - \mathbf{F}^{T} \mathbf{S} \right) \mathbf{m} dl. \tag{41}$$

Here, $\Gamma_r$ is the contour around the crack tip at the distance $r$ away from the crack tip and **m** denotes the unit normal vector to the contour. The corresponding energy dissipated per unit crack extension is a projection of $\mathbf{f}_{tip}$ in the direction of crack extension **e** and gives

$$J_{tip} = -\mathbf{e} \cdot \mathbf{f}_{tip}. \tag{42}$$

$J_{tip}$ is the scalar near-tip $J$-integral and it represents the crack driving force. The scalar driving force caused by the externally applied load into the body is characterized by the far-field $J$-integral $J_{far}$, which results in

$$J_{tip} = J_{far}, \tag{43}$$

since no other defects are present in the homogeneous body incorporating a sharp crack.

## 3.4 MATERIAL INHOMOGENEITY TERM

If the crack tip is situated in the vicinity of a sharp interface, the crack tip stress field experiences a jump as soon as the material properties change at the interface. In this case the interface imposes a shielding or anti-shielding effect on the crack tip. Anti-shielding occurs if the crack is about to propagate from a material with higher Young's modulus and/or higher yield strength into a material with lower modulus and/or strength. If, however, the crack is approaching an interface to a material with higher Young's modulus and/or higher yield strength the crack tip is shielded by the interface [5, 29]. The latter effect is commonly utilized to arrest a crack in a soft interlayer and prevent its further propagation through the whole structure [19, 30, 31]. The same concept of shielding or anti-shielding can be applied for the effect of compressive or tensile residual stresses in a body, respectively. For instance, compressive residual stresses normally act opposite to the stress field originating from external loading. Those stresses have to be overcome before further crack elongation is possible.

If a body incorporates inhomogeneities, the equality between the near-tip and far-field $J$-integral in Equation 43 does not apply anymore. The total material inhomogeneity term $C_{\mathrm{inh}}$ is introduced, quantifying the sum of all material inhomogeneity effects in the body and is added to the far-field J-integral to form the crack driving force [5, 29]:

$$J_{\mathrm{tip}} = J_{\mathrm{far}} + C_{\mathrm{inh}}. \tag{44}$$

An example of such a body is presented in Figure 8, where $J_{\mathrm{tip}}$ is calculated around $\Gamma_{\mathrm{tip}}$ and $\Gamma_{\mathrm{far}}$ is the contour around $J_{\mathrm{far}}$. The crack tip is shielded by the inhomogeneities if $C_{\mathrm{inh}}$ is negative, and anti-shielding occurs if $C_{\mathrm{inh}}$ has a positive value. Specifically in this investigation, the inhomogeneity sources are the sharp interfaces and the residual stress gradients. That results in two inhomogeneity terms:

- **Interface inhomogeneity term** $C^{\mathrm{IF}}$, describing the effect of the jump of material properties as well as the residual stress jump at the sharp interfaces.
- **Gradient inhomogeneity term** $C^{\mathrm{GR}}$, which accounts for the continuous variation of residual stresses in the interlayers.

The sum of $C^{\mathrm{IF}}$ and $C^{\mathrm{GR}}$ results in the total material inhomogeneity term $C_{\mathrm{inh}}$:

$$C_{\mathrm{inh}} = C^{\mathrm{IF}} + C^{\mathrm{GR}}. \tag{45}$$

The configurational force at a sharp interface $\Sigma$ is calculated from the jump of the configurational stress tensor

$$\mathbf{f}_{\Sigma} = -[\![\mathbf{C}]\!]\mathbf{n}, \tag{46}$$

where $\mathbf{n}$ is the unit normal vector to the interface and the corresponding projection in crack propagation direction is given by

$$C_i^{\mathrm{IF}} = -\mathbf{e} \cdot \int_{\Sigma_i} \left( [\![\phi_i]\!]\mathbf{I} - [\![\mathbf{F}_i^{\mathrm{T}}]\!] \langle \mathbf{S}_i \rangle \right) \mathbf{n}_i dl, \tag{47}$$

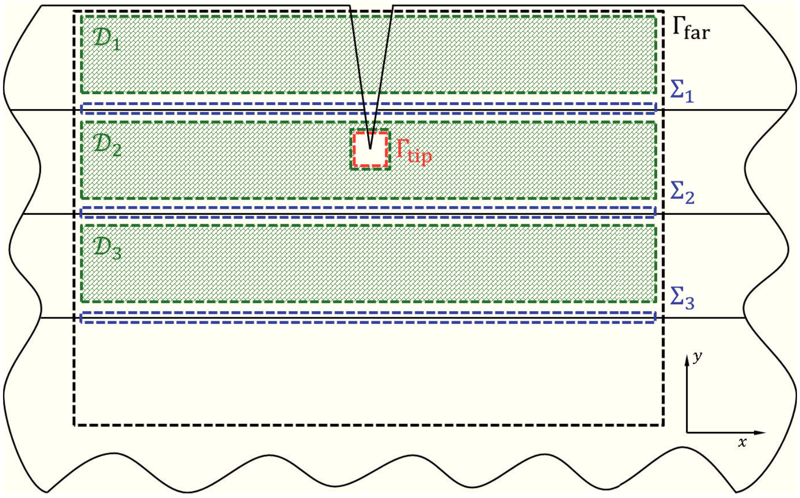

Figure 8: A segment of a tri-layer sample including the contours $\Sigma_i$ and $\Gamma_{\mathtt{far}}$ that are used to calculate the interface term $C^{\mathrm{IF}}$ and far-field $J$-integral $J_{\mathtt{far}}$, respectively. The gradient term $C^{\mathrm{GR}}$ is determined in the regions which incorporate a residual stress gradient denoted by $\mathcal{D}_j$. $\Gamma_{\mathtt{tip}}$ is the crack tip contour where $J_{\mathtt{tip}}$ is calculated and is in this case excluded from $\mathcal{D}_2$.

for a body incorporating $i$ interfaces, with $\Sigma_i$ being the contour around the $i$-th interface, as shown in Figure 8. The summed up contributions from the sharp interfaces give the total interface inhomogeneity term:

$$C^{\mathrm{IF}} = \sum_i C_i^{\mathrm{IF}}. \tag{48}$$

In Equation 47, $\mathbf{n}_i$ denotes the unit normal vector to the $i$-th interface in the body. A jump of a quantity at an interface is designated by $[\![q]\!] = (q^+ - q^-)$ and $\langle q \rangle = (q^+ + q^-)/2$ represents the average of $q$ across the interface. $q^+$ and $q^-$ are the limiting values of $q$ on each side of the interface.

If the residual stress state in the interlayers were constant, $C^{\mathrm{GR}}$ would be zero, as the difference in strain energy density from one material point to the other in the interlayers is vanishing. A study of a ceramic multilayer composite gave only the interface inhomogeneity term $C^{\mathrm{IF}}$ due to the jumps of material properties and residual stresses at the interfaces [32]. In this thesis, the gradient inhomogeneity term $C^{\mathrm{GR}}$ has to be taken into account, since the variation of residual stresses inside the layers leads to an explicit gradient of the strain energy density.

The residual stresses acting parallel to the sharp interfaces exhibit a gradient in $y$-direction. Thus, the stored energy density in the body is experiencing a variation in the same direction. The corresponding configurational force is calculated as the gradient of the strain energy density $\phi = \phi(\mathbf{F}, y)$ in distribution direction, see [5]. The gradient inhomogeneity term for the $j$-th interlayer is derived by Equation 49:

$$C_j^{\mathrm{GR}} = -\mathbf{e} \cdot \int_{\mathcal{D}_j} \nabla_j \phi(\mathbf{F}, y)\, dA. \tag{49}$$

As denoted in Figure 8, the integral is calculated for each region $\mathcal{D}_j$ exposed to a residual stress distribution without considering the adjacent interfaces. If the crack tip contour $\Gamma_{\mathtt{tip}}$ is situated in the layer, the area enclosed by $\Gamma_{\mathtt{tip}}$ must be excluded from the integration area. Summing up the contributions from all the interlayers gives the total gradient inhomogeneity term:

$$C^{\mathrm{GR}} = \sum_j C_j^{\mathrm{GR}}. \tag{50}$$

# 4

# COMPOSITION OF THE INVESTIGATED MATERIALS

## 4.1 THIN FILM TECHNOLOGY

This section is designated to provide a basic understanding about thin film technology and its most common fields of application. It is closely following the book of Adachi and Wasa [33].

For almost 60 years now, thin films are being utilized in the production of electronic devices, optical and protective coatings or just decorative parts. In the very early stages of 1960s, the thin film transistor (TFT) was proposed by Weimer. Due to the instability of the TFTs, the produced devices could not be considered for everyday use. The first practical applications for thin films were centered around passive devices, e. g. thin film capacitors and resistors. In the following years, thin film processing had been implemented in the production of solar cells, such as amorphous silicon (a-Si) sollar cells. a-Si was used to fabricate solar cells for calculators and a liquid crystal television was produced with a-Si TFTs. Ongoing research is dealing with the efficiency of a-Si solar cells, as the energy consumption for the production of single crystal bulk Si solar cells is significantly higher. Thin film technology is also used to produce filters for color displays. Additionally, thin films are used for the realization of sensors, storage devices and new types of random access memory, e. g. ferroelectric dynamic random access memory. The latest applications are mostly concerning the ME industry and are discussed in [33].

Generally, thin films are fabricated by physical and chemical vapor deposition (PVD and CVD) or their combination (PECVD). The growth of thin films can be induced by a thermal process, where a source material is evaporated in a vacuum chamber and the atoms accumulate on a substrate material. A different way to govern thin film growth is via ion processes, i. e. using the irradiation of energetic species or sputtering to create the atom flox for deposition. The variations between the available deposition techniques are further discussed in [33].

Thin films also exhibit unique properties that are related to the way how the thin films are fabricated or grown. Their toughness and strength can be well controlled during the deposition process. Compared to that, strengthening of bulk materials requires additional processing steps.

## 4.2 FABRICATION OF THE INVESTIGATED THIN FILM STACKS

This thesis is focused on the investigation of thin metallic films and their composites deposited on a Si substrate. The materials at hand are primarily tungsten (W) and copper (Cu). Both materials are much desired in the fabrication of modern ME devices. Additional materials processed in the course of fabrication are titanium nitride (TiN) and chromium (Cr), serving as passivation layers on top of the Si wafer. The TiN-layer is considered in the calculations, whereas the ultra-thin Cr-layers are not.

The investigated thin films are deposited on top of Si wafers with a $(100)$ crystallographic orientation. The wafer thicknesses differ between the samples and will be mentioned while they are introduced. Two simple specimens are exclusively used for the residual stress calculations. The first one consists of a $1.58\mu m$ thick Cu film electrodeposited on a $725\mu m$ thick Si substrate. The second sample comprises a W and a TiN film deposited on a Si wafer with a thickness of $700\mu m$. Together, the films are approximately $0.8\mu m$ thick, whereby the TiN-layer is $0.12\mu m$ thick. CVD was used to deposit the TiN as well as the W layer.

More sophisticated thin film stacks were prepared for an in-depth characterization of their mechanical behavior. The samples consist of tri-layer stacks with alternating W- and Cu-layers, i. e. a W-Cu-W and a Cu-W-Cu stack, respectively. The Si substrate is $525\mu m$ thick and all layers have an approximate thickness of $0.5\mu m$ and a globular grain structure. The grain size varies between $60$ and $70nm$ and is determined by a line intercept method from scanning electron microscope (SEM) micrographs, see [34]. For good adhesion, a $10nm$ thick Cr-layer was deposited on Si. Another sample was prepared with a $1.0\mu m$ thick W-layer. The film was not processed in one single step. After depositing about $0.5\mu m$ of W the process was interrupted for $4550s$ before the rest of the layer was completed. The implications of the deposition sequence are explained in Chapter 7. As this thesis is not mainly focusing on the preparation of the material stacks, further information about the deposition conditions and parameters can be taken from [34].

All material systems were produced at room temperature using PVD on a Mantis Sputter System (Mantis, Thame, United Kingdom). While the latter sample is used to determine its residual stress distribution and the flow behavior of W, the W-Cu-W and the Cu-W-Cu stacks are fully characterized. The investigated stacks and the film thicknesses are presented in Table 1.

| Stack | $1^{st}$ Layer [μm] | $2^{nd}$ Layer [μm] | $3^{rd}$ Layer [μm] | Substrate [μm] |
|---|---|---|---|---|
| Cu | Cu 1.58 | – | – | Si 725 |
| W-TiN | W 0.68 | TiN 0.12 | – | Si 700 |
| W-W | W 0.5 | W 0.5 | – | Si 525 |
| W-Cu-W | W 0.5 | Cu 0.5 | W 0.5 | Si 525 |
| Cu-W-Cu | Cu 0.5 | W 0.5 | Cu 0.5 | Si 525 |

Table 1: Investigated thin film stacks with the according film thicknesses.

## 4.3 LINEAR ELASTIC MATERIAL PROPERTIES

The substrate is assumed to behave linear elastically for all stacks which were introduced in the previous section. For Si we use a Young's modulus of 170 GPa and a Poisson's ratio of 0.28, evaluated as a mean value from different sources [35–38]. Additionally, the remaining film materials are assumed to behave linear elastically during the residual stress calculations. A summary of the elastic material behavior for W and TiN was already given in a former article [39]. In the present case for W a Young's modulus of 411 GPa and a Poisson's ratio of 0.28 is used. TiN has a Young's modulus of 390 GPa and a Poisson's ratio equal to 0.34. For the film material Cu the values are 130 GPa and 0.34, respectively, see the values reported in [40–42]. The elastic properties for the materials are given in Table 2.

In order to appropriately determine the failure behavior of the W-Cu-W and Cu-W-Cu stacks, the yield and hardening behavior of W and Cu has to be known in addition to their linear elastic properties. This is part of the current thesis and is investigated in Part iii.

| Material | $E$ [GPa] | $\nu$ [–] |
|---|---|---|
| Si | 170 | 0.28 |
| W | 411 | 0.28 |
| Cu | 130 | 0.34 |
| TiN | 390 | 0.34 |

Table 2: Linear elastic properties of the thin film materials.

# Part II

# RESIDUAL STRESSES IN THIN METALLIC FILMS

In this part of the work, the residual stress state in thin metallic films is studied. In the course of the investigation, the results from numerical calculations were compared to an analytical solution. First results on single-layered specimens were presented in [39, 43]. The analytical approach has proven to be very efficient. Therefore, the residual stress distributions in multi-layered specimens were calculated analytically. The corresponding results were also published in [34].

# 5

# DETERMINING RESIDUAL STRESSES IN THIN FILMS

## 5.1 MOTIVATION

Generally, thin film components for ME applications, such as through silicon vias, are subjected to residual stresses. Residual stresses in thin films cannot be avoided. The reasons for that are variations in the coefficient of thermal expansion or an atomic lattice spacing mismatch between the processed materials. Also, different other factors are influencing the residual stress accumulation in thin films during their deposition [44, 45]. However, in many applications small amounts of residual stresses are tolerable and do not have a significant influence on the performance or reliability of a device. If properly designed, a thin film component can even benefit from the internally generated stresses. In order to be able to describe their mechanical properties, such as fracture behavior, it is important that the residual stress state in thin films and thin film stacks is properly described.

Some literature argues about constant residual stresses in thin films [46–48]. Most of the recent studies, however, show that the residual stresses are locally varying throughout the thin films. X-ray diffraction analysis [49–54] as well as focused ion beam milling (FIB) in combination with digital image correlation (DIC) [51, 55–60] are the most popular techniques for measuring residual stress gradients in thin films. With the latter method a specific region with characteristic features is imaged before and after removal of stressed material. The form of the processed area can have numerous geometrical shapes [57, 60]. After the FIB cut is introduced, the material around the cut deforms due to residual stress relaxation. The corresponding deformation field is determined from scanning electron microscope (SEM) scans taken from the initial and current condition and used to recalculate the initial stress state in the films.

However, the intense FIB milling and forming of different shapes limits the possibilities with FIB-DIC. The complex geometries are not easy to produce and the created FIB cuts can negatively influence the displacement and strain gradient, as the strain relief can lie inside the FIB damaged region [55, 60, 61]. It has been shown that ion damage generally depends on the materials and ions involved in processing as well as the ion current, their incident angle and acceleration voltage [62]. Moreover, the DIC measurements depend on the precision of the imaging system and the utilized correlation algorithm [63, 64]. This does not necessarily mean that FIB milling is not suitable for the evaluation of residual stresses, but that FIB damage, which can compromise the results, has to be minimized. Additionally, simpler analysis tools compared to the DIC method would be beneficial. That being said, the so-called ion beam layer removal (ILR) method is a promising alternative approach to determine residual stress distributions in different thin film stacks [39, 43].

## 5.2 THE ION BEAM LAYER REMOVAL METHOD

### 5.2.1 *Experiments*

As many other approaches, the ILR method combines experimental efforts with analytical or numerical calculations. The experimental part involves cutting of beam shaped micro samples and subsequent milling of thin layers in a designated area as well as SEM imaging. Notably, the method utilizes FIB milling, but the relation between the FIB milled region and sample size suggests that the FIB damage does not have a significant impact on the results. Sample preparation and the milling procedure are not the main part of this thesis and shall be shortly summarized here. Details about the sample fabrication can be found in [34, 65].

The measurements start after the cantilever is prepared as shown in Figure 9, where initially the beam is fixed on both sides, as demonstrated in Figure 9a. As soon as one side of the bridge is cut free (see Figure 9b), the beam deflects in the positive or the negative direction, depending on the residual stresses present in the system. The following steps are necessary to determine the residual stress distribution:

1. The micro-beam dimensions are determined from SEM recordings.
2. The initial deflection of the cantilever is measured at its free end by SEM imaging, as shown in Figure 9b.
3. After that, a thin layer of material is removed in the ILR area (see Figure 9b) by FIB milling. The ion beam penetrates the cantilever from the side which reduces the area influenced by ion bombardment; in the view of Figure 9 it travels in out-of-paper-plane direction.
4. A SEM picture is taken to determine the thickness of the removed layer, in the following termed sublayer, and the current deflection of the micro-beam.
5. Step 3. and 4. are repeated until the whole film is removed from the substrate.

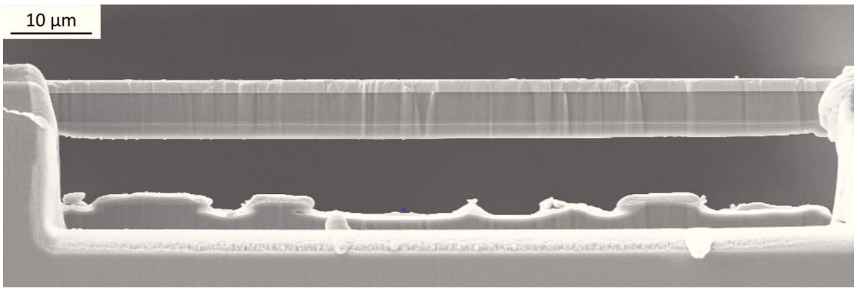

(a) Bridge prepared for FIB milling.

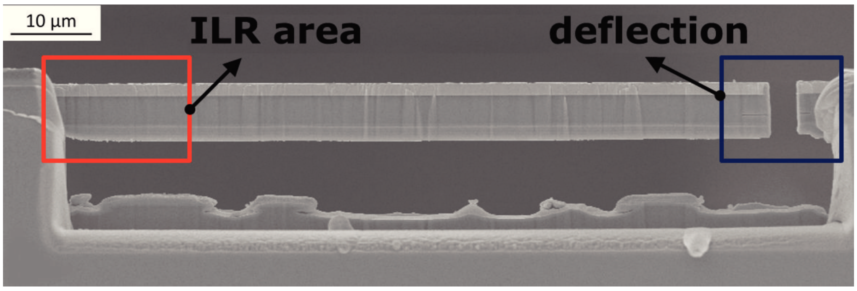

(b) Released beam at the front, where the deflection is measured. The thin layers of material are removed in the ILR area

Figure 9: SEM micrographs of a Cu-Si beam prepared for residual stress calculations with the ILR method.

### 5.2.2 *Analytical solution*

The stress in each sublayer is determined from the current deflection, the elastic properties of the system, given in Table 2, and the dimensions of the cantilever. In order to calculate the residual stresses in the sublayers analytically, the measured deflections as well as the sublayer thicknesses are stored in text files. The analytical approach utilizes the Euler–Bernoulli beam theory [66] and in this work the scheme from Jiang et al. [67] is followed closely. In the following the calculation is explained in detail:

If small elastic deformations are assumed, the curvature $\kappa$ of a cantilever can be calculated from its deflection curve $u(x)$ as

$$\kappa = \frac{d^2u}{dx^2}. \tag{51}$$

The solution of the differential equation relates the initial deflection and the initial curvature of the entire cantilever,

$$\kappa_0 = -\frac{2\delta_0}{l^2}, \tag{52}$$

where $l$ is the cantilever length and $\delta_0$ and $\kappa_0$ denote the deflection and curvature after the micro-beam is cut free, respectively. While the film material in the ILR area is gradually removed, the curvature in this area changes and thus the deflection of the cantilever. Furthermore, the deflection change of the cantilever is a function of the cantilever thickness in the ILR area as well as the initial deflection calculated from Equation 52. In this case, the curvature in the ILR area can only be determined iteratively as

$$\delta_i = \frac{1}{\kappa_i^A}\left(1-\cos\left(\kappa_i^A l^A\right)\right) + \sin\left(\kappa_i^A l^A + \kappa_0 \frac{l^R}{2}\right)\frac{2}{\kappa_0}\sin\left(\kappa_0 \frac{l^R}{2}\right) \tag{53}$$

for each measured deflection $\delta_i$ [65]. In Equation 53, $i = 1, \ldots, n$ labels the remaining material system which consists of the substrate and $n-i$ sublayers and the respective curvature is denoted by $\kappa_i^A$. The length of the ILR area and the remaining cantilever length are denoted by $l^A$ and $l^R$, respectively.

What follows is the calculation of the residual stress on the basis of force and momentum balance in the cantilever. This is done for each removed sublayer by reintroducing them into the system in reverse order, starting with the last removed sublayer. As no external forces are applied to the cantilever, its deflection is caused solely by the preexisting residual stress in each sublayer j. By solving the following force and momentum equilibrium equations, respectively, the residual stress for each sublayer can be determined:

$$P = \int_0^{t_{sub}} \sigma_{x,0}(y)\, dA + \sum_{j=0}^{n} \int_{t_j}^{t_{j+1}} \sigma_{x,j}(y)\, dA = 0, \tag{54}$$

$$M_y = \int_0^{t_{sub}} \sigma_{x,0}(y) \cdot y dA + \sum_{j=0}^{n} \int_{t_j}^{t_{j+1}} \sigma_{x,j}(y) \cdot y dA = 0. \tag{55}$$

In Equation 54 and Equation 55, $\sigma_{x,0}$ represents the stress distribution in $y$-direction in the substrate and $\sigma_{x,j}$ denotes the stress distribution in the sublayers in a relaxed system. $t_{sub}$ and $t_j$ are the substrate thickness and the current distance to the coordinate system origin, which is situated at the bottom of the substrate as shown in Figure 10.

Finally, $dA$ denotes the integration area. Furthermore, it is assumed that the thin film is in a biaxial plane stress state, as the wafer diameter is much larger than its thickness. This means that $\sigma_{x,j}(y) = \sigma_{z,j}(y)$, where the $z$-direction lies perpendicular to the $x$-direction in the same plane. Additionally, it is assumed that the biaxial stress state does not change significantly as the cantilever is prepared. The stresses in Equation 54 and Equation 55 are a summation of the bending stress $\sigma_{x,j}^b(y)$, which is controlled by the cantilever deformation, and the eigenstress or residual stress in each sublayer $\sigma_{x,j}^{res}$. The total stress is calculated in the following way:

$$\sigma_{x,j}(y) = \sigma_{x,j}^b(y) + \sigma_{x,j}^{res} = \left(\varepsilon_{x,j}^b(y) + \varepsilon_{x,j}^{res}\right) \cdot E_{b,j} = \varepsilon_{x,j}(y) \cdot E_{b,j}. \tag{56}$$

In Equation 56, $E_{b,j}$ is the biaxial Young's modulus of each individual sublayer and is calculated as

$$E_{b,j} = \frac{E_j}{1-\nu_j}, \tag{57}$$

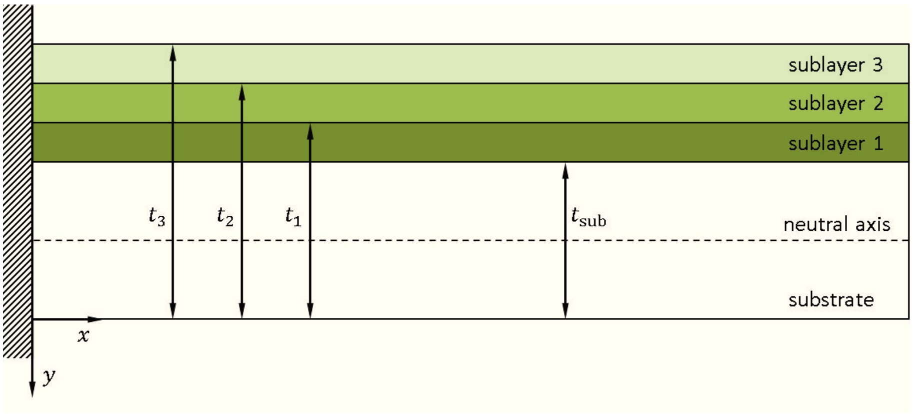

Figure 10: An exemplary sketch of a specimen consisting of a substrate and 3 sublayers. The neutral axis for a Si beam without considering the sublayers is marked by the dashed line. The residual stress for each sublayer is determined by reintroducing them onto the Si beam, starting with sublayer 1.

where $E_j$ is the Young's modulus of the material and $\nu_j$ is its Poisson's ratio. The bending strain is denoted by $\varepsilon^{b}_{x,j}(y)$, the eigenstrain is denoted by $\varepsilon^{res}_{x,j}$ and $\varepsilon_{x,j}(y)$ is the total strain, for the j-th sublayer. There is no material separation during deformation, i. e. the bending strain distribution over the cantilever thickness has to be linear, meaning that

$$\varepsilon^{b}_{x,j}(y) = \kappa_j y + d_j. \tag{58}$$

Here, $\kappa_j$ represents the current curvature determined with Equation 53. Notably, $\kappa_j$ can only be determined relative to the neutral axis, see Figure 10. As Equation 53 by definition refers to the neutral axis the $y$-coordinate has to be offset by $d_j$. Ultimately, this results in a system of equations which has to be solved for each sublayer where $\sigma^{res}_j$ and $d_j$ are the two unknown parameters.

The residual stress calculations in the removed thin film layers are performed with a script, which is realized in the computing software Maple™ (Maplesoft, Waterloo, Canada) [34]. In the preamble the application is provided with input data, such as the cantilever geometries and the elastic properties of the materials. Additionally, the sublayer thicknesses and the corresponding deflections, obtained from the experiments, are read from text files. After providing this initial input, every following sequence in the script is performed automatically. In a first iterative loop, the curvatures for each sublayer are calculated following Equation 53 where, notably, each current curvature depends on the preexisting curvatures. Secondly, the sublayers are re-deposited step by step in another iterative loop, starting with the last removed layer. It is assumed that the substrate is initially stress-free and thus undeformed. The residual stress $\sigma^{res}_j$ and offset $d_j$ for each attached sublayer are calculated by solving the force and momentum balance from Equation 54 and Equation 55, depending on the parameters determined from the previous sublayers and the curvature from the current layer. Finally, the residual stress distribution is returned.

### 5.2.3 *Numerical approach*

The numerical calculations combine finite element (FE) modeling and an inverse optimization algorithm. The FE simulations are performed with the software package ABAQUS (Simulia, Dassault Systems) and the Levenberg-Marquardt algorithm is used for optimization [68, 69]. This is realized within a graphical user interface (GUI) which was designed for this purpose at the MCL (see Figure 11a). Three tabs are designated for the creation of a 3D FE model of the cantilever, as shown in Figure 11b, the calculation as well as the output of the residual stress gradient in the thin film. The Settings tab is designed for the pre-processing part of the complete ABAQUS environment (CAE), where the geometries are assigned to the micro-beam and the mesh requirements and material properties are set up for the model. In the Parameter tab, the FE pre-processing part is completed after defining a parameter vector with an initial residual stress distribution for the film. One continues to prepare the inverse optimization routine, which is realized with Python, by listing the experimental data needed for the optimization; e. g. the sublayer thicknesses and the corresponding deflections. Also, the optimization parameters have to be fixed.

After the cantilevers are prepared and cut free for the residual stress calculations, they are still fixed to the rest of the remaining wafer on their back side, as shown in Figure 9. It is important that the elastic fixation between the actual beam and the remaining or untreated structure is considered in the FE model via a boundary condition, as it was discussed in detail in [39]. It was demonstrated on an example that the so-called box deformed elastically in the vicinity of the elastic junction or fixation, highlighted in Figure 11b. Compared to a rigidly fixed cantilever, the stresses are reduced over the film thickness as the micro-beam with the box can be freely deformed. On the front side, however, the cantilever is initially clamped in all directions. The parameter vector, containing the estimated residual stress field, is applied via an initial condition. When the nodes on the front side are released, the residual stresses inside the film relax, leading to a deflection of the micro-cantilever (see Figure 11b). The direction and magnitude of the deflection depends on the initial choice of the residual stress vector. Subsequently, the FIB milling in the ILR area, highlighted on the FE model in Figure 11b, is performed in the simulation by deleting the element layers corresponding to the sublayers removed in the procedure. By utilizing a modeling technique called "model change" it is possible to change the stiffness of a selected element set to approximately zero. In order to reduce the calculation time, each sublayer is modeled with one row of elements. Loss of precision is avoided by using fully integrated 20—node quadratic brick elements C3D20.

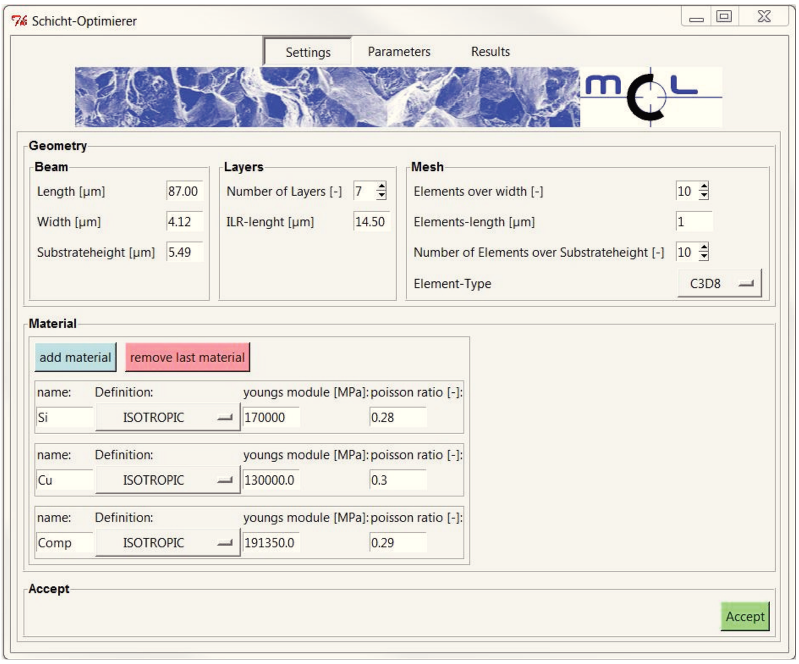

**Geometry**

**Beam**
Length [µm] 87.00
Width [µm] 4.12
Substrateheight [µm] 5.49

**Layers**
Number of Layers [-] 7
ILR-lenght [µm] 14.50

**Mesh**
Elements over width [-] 10
Elements-length [µm] 1
Number of Elements over Substrateheight [-] 10
Element-Type C3D8

**Material**

| name: | Definition: | youngs module [MPa]: | poisson ratio [-]: |
|---|---|---|---|
| Si | ISOTROPIC | 170000 | 0.28 |
| Cu | ISOTROPIC | 130000.0 | 0.3 |
| Comp | ISOTROPIC | 191350.0 | 0.29 |

**Accept**

(a) Example of the graphical user interface. Here, a picture of the Settings tab is presented.

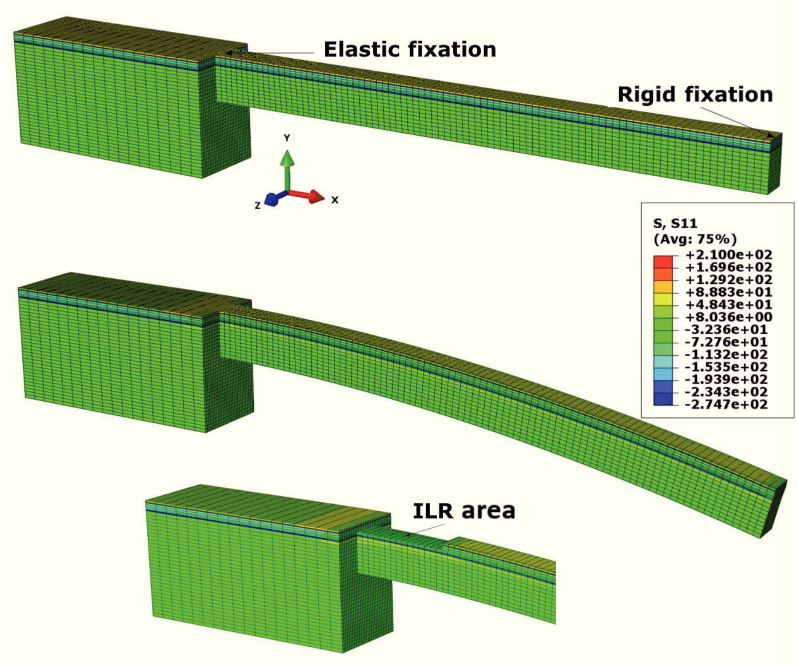

(b) From top to bottom: FE model in its initial state, with intact boundary conditions. The beam is relaxed and equilibrated. Subsequently, the sublayers in the ILR area are removed. After each layer removal an equilibration step is introduced.

Figure 11: Numerical tool for the calculation of the residual stresses.

At this point the Levenberg-Marquardt algorithm enters the calculation. The predefined parameter vector, containing the initial residual stress distribution, is altered systematically with the goal to minimize the deviation between the simulated and experimental deflections. The iterative procedure terminates after a certain threshold deviation is met and the last determined stress vector is considered as the residual stress distribution in the thin film. After the calculations have completed, the functions of the Results tab in the GUI become available, where one has the possibility to visualize the resulting deflections and residual stresses.

## 5.3 RESIDUAL STRESSES IN SIMPLE THIN FILM/SUBSTRATE CONFIGURATIONS

The first residual stress calculations were performed on the Cu film deposited on Si. The second sample consists of the W-layer combined with a very thin TiN-interlayer deposited on Si. The thin film dimensions were already introduced in Table 1 and are not repeated here. As mentioned before, the micro-cantilever beams for the residual stress calculations are prepared by FIB milling. The beam geometries are listed in Table 3 and are denoted according to Figure 12. The elastic constants for the FE simulations are taken from Table 2.

| Specimen | W [μm] | B [μm] | ILR [μm] | L [μm] |
|---|---|---|---|---|
| Cu | 7.07 | 4.12 | 14.50 | 87.00 |
| W-TiN | 5.83 | 7.82 | 14.56 | 90.24 |

Table 3: The dimensions of the micro-cantilevers for the residual stress calculations.

The residual stress distribution through the Cu film calculated analytically and numerically is shown in Figure 13a. In this example the thickness of the removed layers is around 0.15μm. The core part of the film experiences nearly constant residual stresses.

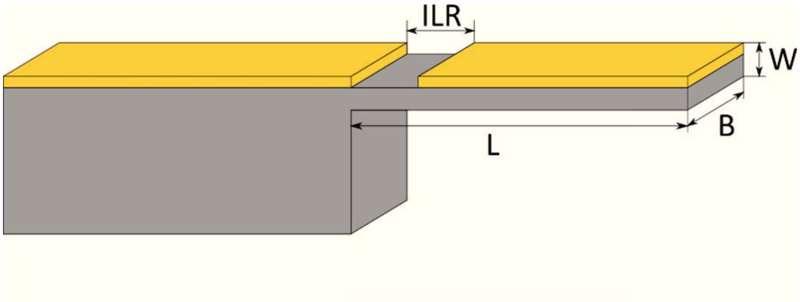

Figure 12: Sketch of a processed specimen for residual stress calculations where the film layer in the ILR area has already been removed.

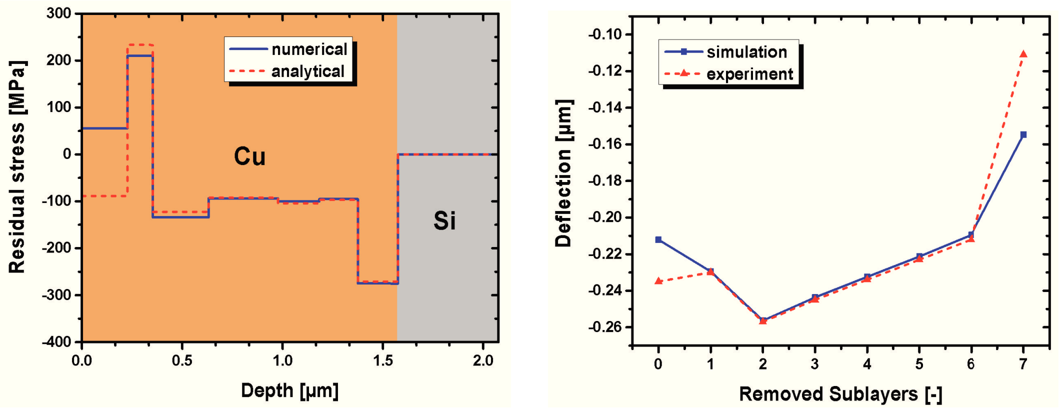

(a) Comparison of the residual stress distributions in the Cu film, calculated numerically and analytically.

(b) Comparison of the experimentally determined and optimized deflections for the Cu-Si sample.

Figure 13: Analytical and numerical results from the residual stress calculations for the Cu-Si micro-cantilever beam.

This behavior is a consequence of a thermo-mechanical treatment for a number of cycles from previously conducted wafer curvature measurements. Moreover, in this process most of the residual stresses caused by the fabrication process are relieved by plastic deformation. The residual stress behavior is confirmed by the predominantly linear behavior of the deflection curve through the middle part of the film, as shown in Figure 13b. In this particular example there are some deviations between the analytical and numerical deflection profiles for the first and last sublayer. It can be safely assumed that the numerically determined stress will become of compressive nature if the simulated deflection approaches the experimental one. In order to minimize these deviations, calculations with different sets of optimization parameters have been performed. However, the system seems to be stuck in a local minimum, where it reaches the desired requirements to stop the optimization loop.

The optimization algorithm performs better for the second example. In Figure 14a the numerical and analytical results are compared for the W-TiN film. The numerically estimated deflections almost match the experimentally measured deflection profile, which is evident from Figure 14b. However, the analytical solution tends to result in higher stress values, especially in the vicinity of the interface between TiN and W. The reason for that is that the analytical approach is more susceptible to irregular deflection profiles. Thus, errors which inevitably occur during the experiments and deflection estimations from the SEM scans can result in higher stress peaks. In the upcoming chapter this issue is appropriately addressed by some improvements to the calculation method. The thickness of the removed layers in this example is significantly smaller compared to the Cu specimen. In order to demonstrate the importance of a higher number of sublayers, the numerical result from Figure 14a is compared to a residual stress distribution with a lower depth resolution in Figure 15. The higher residual stress resolution reveals a residual stress peak of about 3GPa in the vicinity of the W/TiN interface.

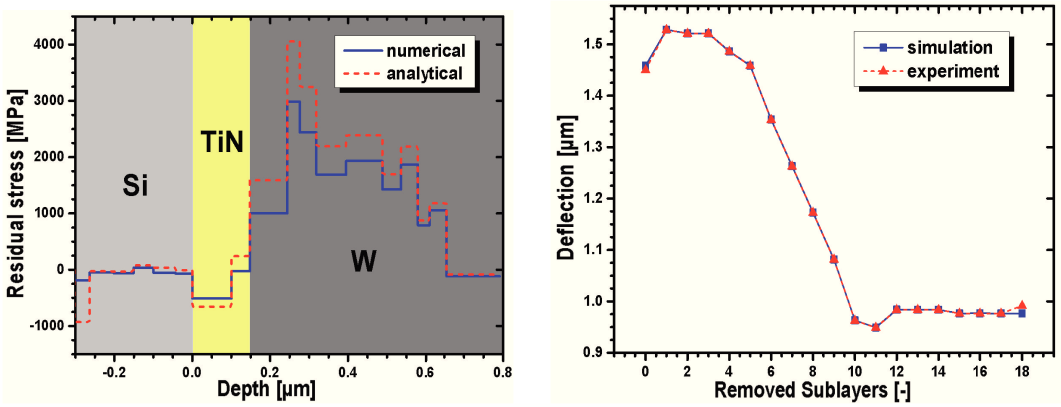

(a) Comparison of the residual stress distributions in the W-TiN stack, calculated numerically and analytically.

(b) Comparison of the experimentally determined and optimized deflections for the W-TiN-Si sample.

Figure 14: Analytical and numerical results from the residual stress calculations for the W-TiN-Si micro-cantilever beam.

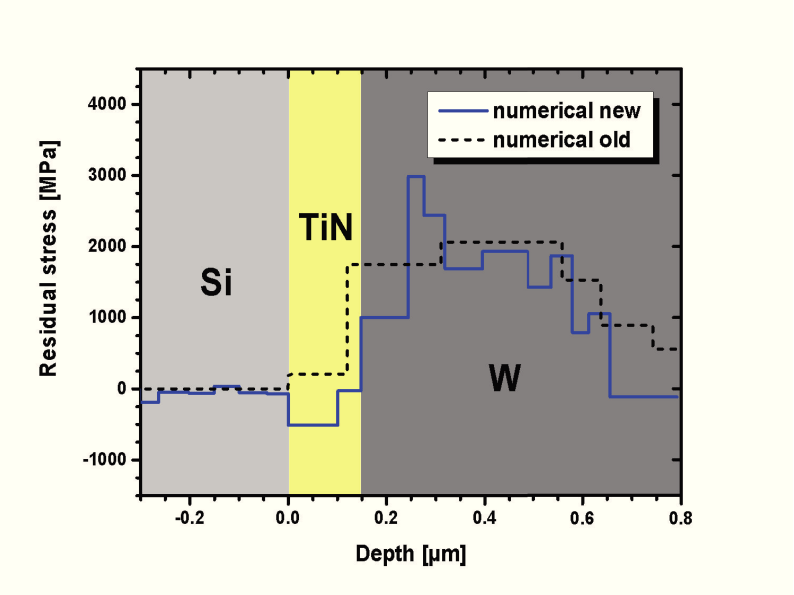

Figure 15: Comparison of the numerically determined residual stresses with a low resolution (black dashed line) and a high resolution (blue solid line).

6

# LOCALLY VARYING RESIDUAL STRESSES IN MULTI-LAYERED STACKS ON A SUBSTRATE

Compared to the analytical solution, the numerical approach becomes increasingly more time consuming as the thickness of the layers removed in the ILR area decreases. In other words, by increasing the number of FIB cuts, the number of elements in the FE model drastically rises and the size of the predefined stress vector for the optimization increases. Thus, the optimization algorithm coupled to the FE simulation needs disproportionally more time to find a suitable match between the experimental and simulated deflection curve. The analytical approach, on the other hand, does not suffer from a drastic increase in computation time. Because of the aim to rigorously resolve the residual stresses in a W-Cu-W and Cu-W-Cu stack deposited on a Si wafer where each individual film has a thickness of $0.5\mu m$, it was decided to improve the precision and automation of the experimental as well as the analytical procedure.

## 6.1 ADJUSTMENTS TO THE EXPERIMENTAL PROCEDURE AND ANALYTICAL SOLUTION

### 6.1.1 *Automatically conducted experiments*

To accurately capture the deflection values after each removal step in the ILR area, the sample has to be properly prepared and the FIB-SEM workstation has to be handled with caution in several steps. In the previous examples from Figure 13 and Figure 14 it was possible to perform this procedure manually. If, however, stacks like the W-Cu-W or Cu-W-Cu tri-layer systems are thoroughly investigated, it is difficult to achieve the expected accuracy of the results; especially if the sublayers are thinner than $0.1\,\mu m$. In order to acquire precise data in the fastest possible way, the cutting and imaging routine was fully automated. Details about the procedure were discussed in [34]. With this approach it is possible to reliably determine when the FIB cut reaches an interface from one film to the other by imaging the ILR area. Previously this was done by an estimate from the deflection profile. Furthermore, by setting up markers on the specimens the stage movement for FIB milling and imaging can be improved. Consequently, the micro-cantilevers can be imaged at the same position several times, e. g. the deflection is recorded three times after each cut. This allows estimating the statistical error made during the deflection measurement. Finally, the machine is set to remove 50nm of material in the ILR area in each step, which corresponds to the grain size and results in approximately ten sublayers per film.

### 6.1.2 *Analysis improvements*

The residual stress profile in a single film is expected to have a smoother gradient if the sublayer thickness is reduced. Due to inevitable errors while determining the cantilever deflections from SEM images, the resulting residual stress distribution can show an unexpected trend through a single film, see e. g. the W-layer in Figure 14a. Because of the improved experimental method, this error can be diminished by building an average deflection profile from the three measured data sets. Additionally, to smoothen out potential runaway residual stress values the averaged data is fitted with higher order polynomial functions. In Figure 16, the average deflection profile and its fitted value are compared. The deflections for each film have to be fitted separately, as the deflection profile in each layer behaves differently.

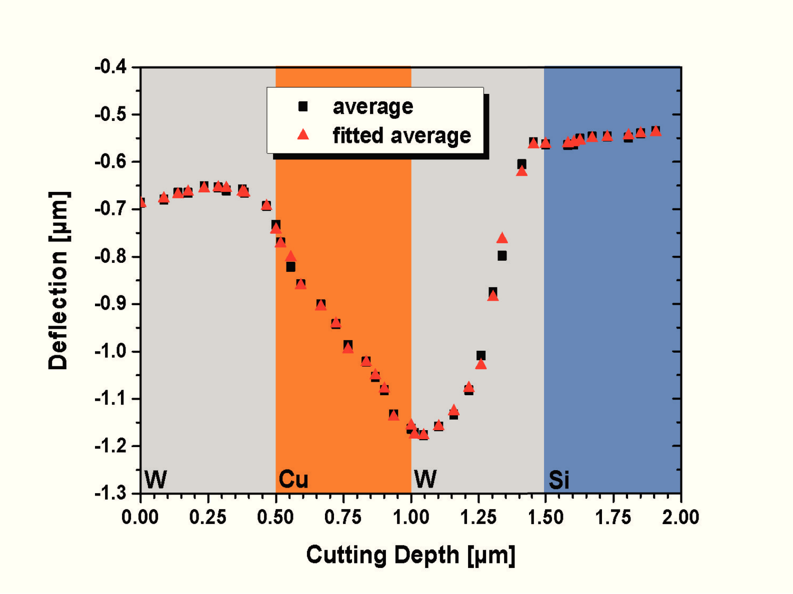

Figure 16: The average value of the three measured deflection profiles for the W-Cu-W stack, marked by the black squares. To further improve the quality of the resulting residual stresses the average value is fitted with higher order polynomials (red triangles).

## 6.2 ANALYTICAL RESULTS FOR TRI-LAYER STACKS ON A SUBSTRATE

As described in the previous chapter, a Maple$^{TM}$ script has been designed to automatically perform the calculations and the residual stresses are readily derived. 40 sublayers

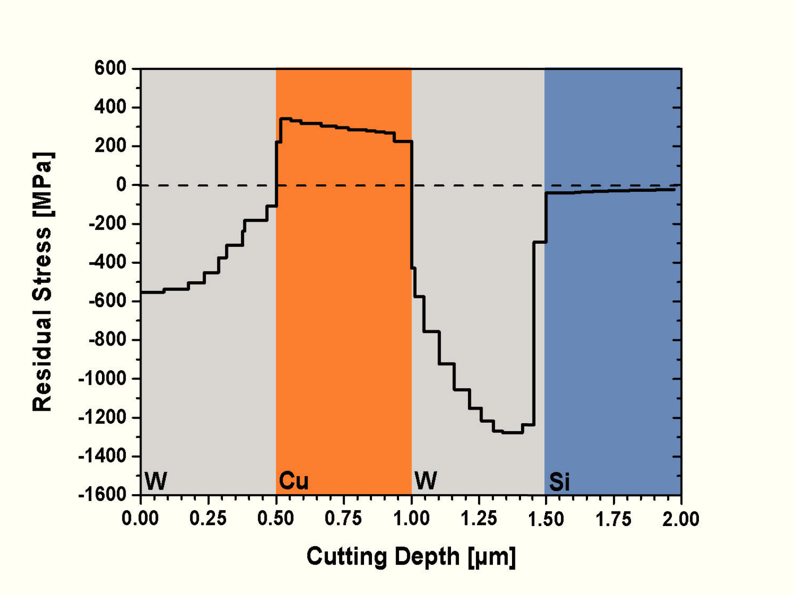

Figure 17: Residual stress distribution in the W-Cu-W stack.

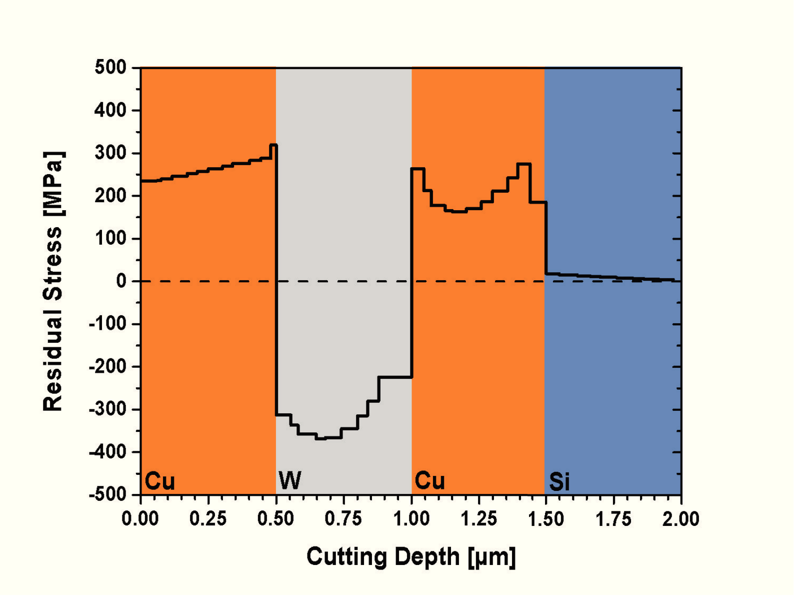

Figure 18: Residual stress distribution in the Cu-W-Cu stack.

have been removed in the ILR area for the W-Cu-W as well as the Cu-W-Cu micro-beams. After the corresponding deflections and sublayer thicknesses have been provided to the script, the corresponding curvatures are calculated and stored in a list. Additionally, a list of biaxial Young's moduli is created according to the number of cuts in each film. Before the routine starts, a list with placeholders for $\sigma_j^{res}$ is defined which are replaced with their corresponding results as the derivation carries on.

The resulting residual stress distributions in the W-Cu-W and Cu-W-Cu stacks are shown in Figure 17 and Figure 18, respectively. Owing to the improved data analysis a smooth residual stress variation is achieved in the respective thin films. Also, the residual stresses exhibit a jump in the stress value at the sharp interfaces. In both stacks the W-layers are subjected to compressive and the Cu-layers exhibit tensile residual stresses, respectively.

## 6.3 SUMMARY AND CONCLUSION

In the present part, the residual stress behavior in thin metallic films deposited on a Si wafer was investigated. Based on the ILR method an analytical and a numerical approach to calculate the residual stress distributions through the films were introduced. The analytical derivation is based on the Euler–Bernoulli beam theory. Here, the residual stress distribution in the thin films is calculated in an iterative procedure from the force and momentum balance in the prepared micro-cantilevers. The more sophisticated numerical approach combines FE simulations and a least-squares optimization (Levenberg-Marquardt algorithm).

For simple film/substrate combinations such as the Cu/Si or W-TiN/Si samples, the residual stress resolution through the films was held relatively low. In this case, the analytical and numerical approach were compared. The results for the Cu/Si show very similar behavior when comparing the analytical and numerical approach. On the other hand, the analytically determined residual stresses overestimate the residual stresses in the W-layer, supposing that the numerical calculation is more accurate. In the example of the W-TiN/Si calculation it was also shown that a higher resolution reveals residual stress peaks never reported before.

The numerical implementation is much more powerful in terms of taking into account complex boundary conditions and material properties. However, the analytical method is much faster. In order to determine residual stresses in the complex W-Cu-W/Si and the Cu-W-Cu/Si samples, the analytical method was preferred. In this case the numerical calculation consumes too much computational time, because of a larger model and a significantly higher number of optimization steps. Anyway, the analytical solution yields very good results, especially after a more sophisticated analysis and a refined experimental approach.

As properly determined residual stresses have an influence on the material and the fracture behavior of the stacks, the presented results are of crucial importance in the upcoming chapters.

# Part III

# MATERIAL BEHAVIOR OF THIN METALLIC FILMS

This part of the thesis covers the study about the material behavior of the thin films. In order to determine the elastic-plastic properties of the materials an appropriate calculation scheme had to be established. Early results were already presented in [70]. Details about the method and final results were published in a recent article [71].

# 7

# FLOW BEHAVIOR OF NANO-SIZED TUNGSTEN AND COPPER FILMS

## 7.1 DISCOVERING FUNCTIONAL MATERIALS

Depending on the requirements for ME components, such as reliability or high functionality, different types, sizes and arrangements of thin films are used in their assembly. However, the strength of such thin films is controlled by their external and internal dimensions, i. e. the grain size and film thickness. Obviously materials on the sub-micron scale behave differently than their bulk counterparts [72–74]. Researchers have been pursuing this topic for a long time now and the two main fields of interest have been single-crystalline materials [72, 75, 76] and polycrystalline materials [77–79]. The behavior of single-crystalline materials is controlled by their external dimensions. On the other hand, the grain size or internal structure is controlling the strength and hardening of polycrystalline materials.

The size effect on the plastic deformation in thin single-crystalline films can be described by the limited movement of dislocations within the film [44, 80]. As the film thickness plays the role of the grain size in this case, the yield strength depends on the film thickness, which is directly related to the extension of at least one dislocation loop which has to fit into the film. The strengthening effect on a material by reducing the dimensions of single-crystalline specimens has also been observed experimentally, e. g. by tensile and compression testing [72, 75, 81, 82] or bending beam experiments [76, 83]. On the other hand, the deformation properties of polycrystalline materials are mainly driven by dislocation pile-up at grain boundaries [10, 73]. Since the size of thin films used in advanced microelectronics ranges between a few $\mathrm{nm}$ and a few $\mathrm{\mu m}$, the most anticipated materials are nanocrystalline [77, 84, 85], i. e. polycrystalline materials with grains on the nanometer scale.

Most recently, studies have been focusing on the research of thin nanocrystalline films which contain only few grains across their thickness. A general consensus about the strengthening effect on such materials has yet to be found, as some researchers are reporting strengthening effects [86] and others are observing weakening of such materials [87]. However, it is clear that the strength of such nanocrystalline materials can be controlled by altering their microstructure while decreasing the external dimensions [73, 86, 87]. In order to properly utilize thin nanocrystalline films in the design of microelectronic components, their material behavior has to be uncovered. For this purpose appropriate experiments have to be conducted and numerical tools have to be developed.

## 7.2 NANOINDENTATION EXPERIMENTS

The flow and hardening behavior of thin nanocrystalline W and Cu films is determined with samples which stem from the same wafers as the specimens prepared for the residual stress investigations. This ensures that the appropriate loading conditions are considered during the calculations. The plastic behavior of W is derived from the W-W specimen, presented in Table 1. As discussed in Section 4.2, a disruption of the deposition process results in a variation of the residual stress state in the film, as shown in Figure 19. The second stack is the W-Cu-W tri-layer, with the film dimensions from Table 1. The residual stresses for this stack were already characterized, see Figure 17.

In order to determine the flow behavior of the W and Cu films, we performed nanoindentation experiments. The experiments were conducted on a platform Nanoindenter G200 (Keysight Tec. Inc, Santa Rosa, CA, USA) at room temperature, equipped with a spherical diamond indentation tip (Synton-MDP AG, Nidau, Switzerland), depicted in Figure 20. The tip has a radius of around 10µm. The nanoindentations were performed in a standard load controlled operating scheme where a maximum load of 100mN at a preset loading time of 30s was reached.

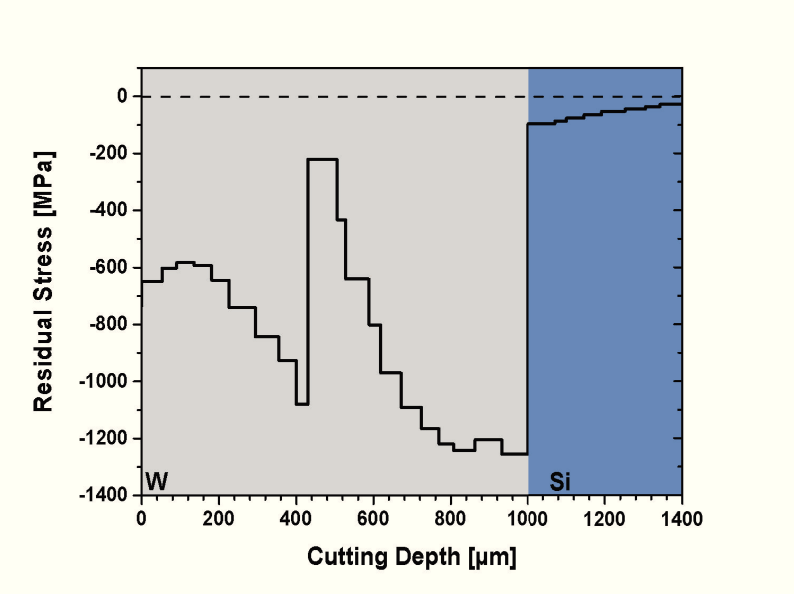

Figure 19: Residual stress distribution in the W-W stack.

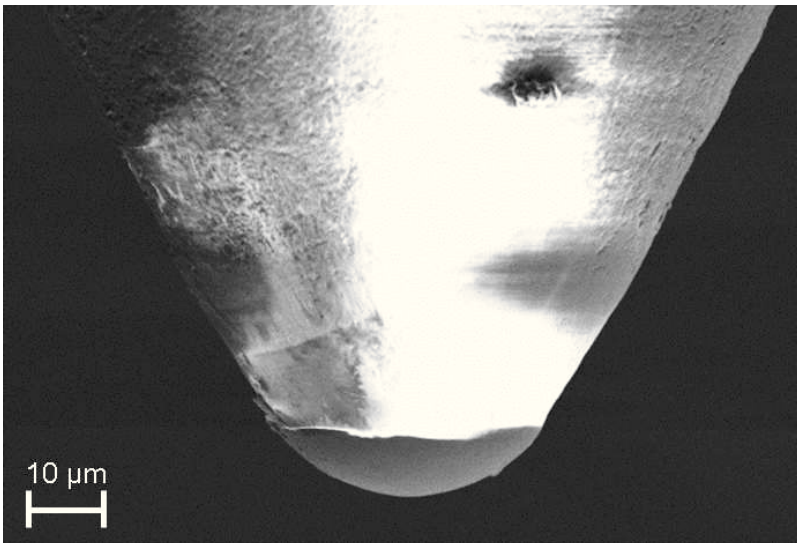

Figure 20: SEM micrograph of the nanoindenter tip, made of diamond.

The force-displacement curves are presented in Figure 21. The six experimental curves for the W-W (solid lines) as well as the W-Cu-W (dashed lines) stack configuration almost coincide and lie within 2% deviation. This is in fact a consequence of the nanocrystalline nature of the investigated films. However, as long as a large enough material volume is examined, the results should not be much different for other materials with different grain structure or material combinations. Because of the softer Cu-interlayer in the W-Cu-W tri-layer system the loading segments of the two stack configurations differ.

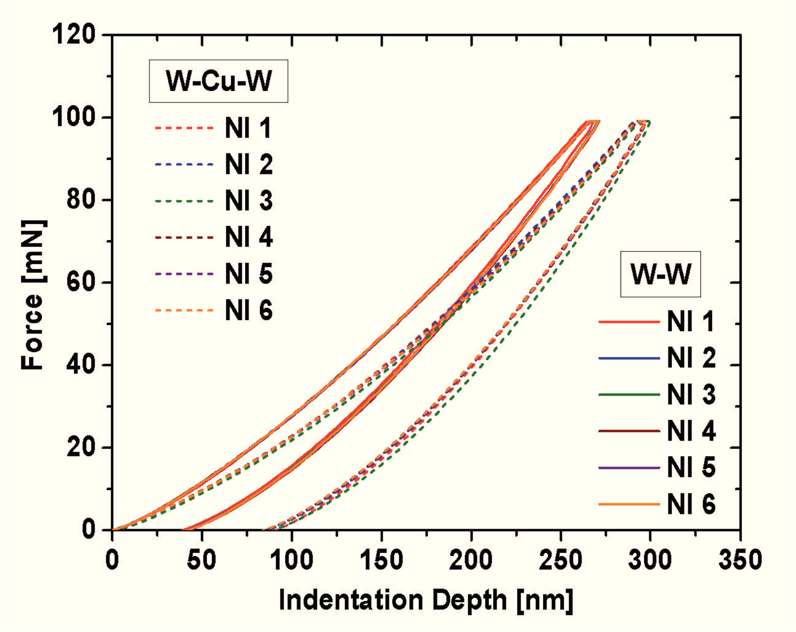

Figure 21: All six experimentally acquired loading curves for the W-W sample (set of solid lines) and the W-Cu-W sample (set of dashed lines).

The nanoindenter tip does not penetrate into the pure W-layer as deep as it does into the layer system with Cu. Similar behavior has been observed in [88], where titanium and chromium interlayers have been introduced into a W-Cu-SiO2-Si system.

The maximum indentation depth for the W-W specimen reaches approximately a fourth of the layer thickness. Moreover, the plastic indentation depth for the W-Cu-W 1.5$\mu m$ thick stack is about 20% of the total layer thickness, meaning that 10% of the film thickness were exceeded. Therefore, potential substrate effects cannot be excluded [89, 90]. However, because the indented volume contains a large number of grains, this effect should not be significant.

## 7.3 NUMERICAL TOOL

### 7.3.1 *Finite element model*

In order to inversely derive the unknown yield strength and inverse hardening parameter, a model of the nanoindentation experiment has to be created. For this purpose a Python script is established which automatically generates a 2D axial symmetric model of the experiment. As an example, the model of the W-Cu-W tri-layer stack on the Si substrate is shown in Figure 22a. The corresponding symmetry axis is the y-axis. The surface directly below the nanoindenter and the face on the outside of the model are unconstrained, which allows the material to move freely in lateral direction, along the x-axis. The nanoindenter tip is assumed to be perfectly spherical and, unlike the material below the tip, sliding of the indenter in x-direction is not allowed. This means that the tip has only the possibility to move in indentation direction, i. e. parallel to the y-axis. The force from the experiment is applied as a concentrated force to a node at the tip of the nanoindenter, denoted by $F$ in Figure 22a. Finally, the bottom of the model is constrained in y-direction.

Additionally, the material behavior of such thin film stacks can be influenced by their inherent residual stress state. Therefore, the residual stress distributions are considered in the models. The residual stress distribution from Figure 17 is indicated in the enlarged area around the indenter tip in Figure 22b. The stresses act perpendicular to the symmetry axis and are prescribed by means of the user subroutine SIGINI. Depending on the distance from the origin in y-direction the residual stresses are induced at the integration points of the elements. The magnitude of the tangential stress is equal to the residual stress component. Thus, a biaxial stress state in the thin films is realized.

The specimens are modeled with 4-node bilinear (CAX4) elements. In order to appropriately resolve the deformed region around the nanoindenter tip, the element size in its vicinity is held at a constant size of 0.05$\mu m$, evident from Figure 22b. The rest of the model is meshed with coarse elements with a maximum size of 0.5µm, ensuring sufficiently low computation times for the simulations.

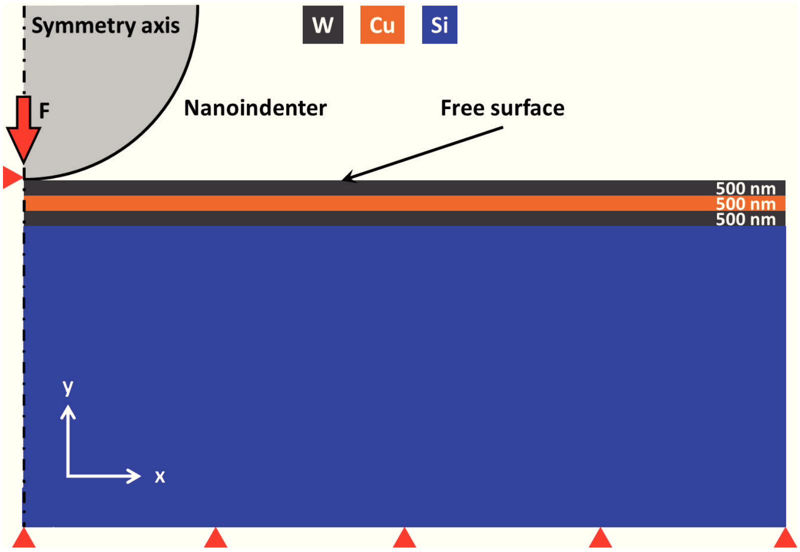

(a) Boundary conditions in the FE model.

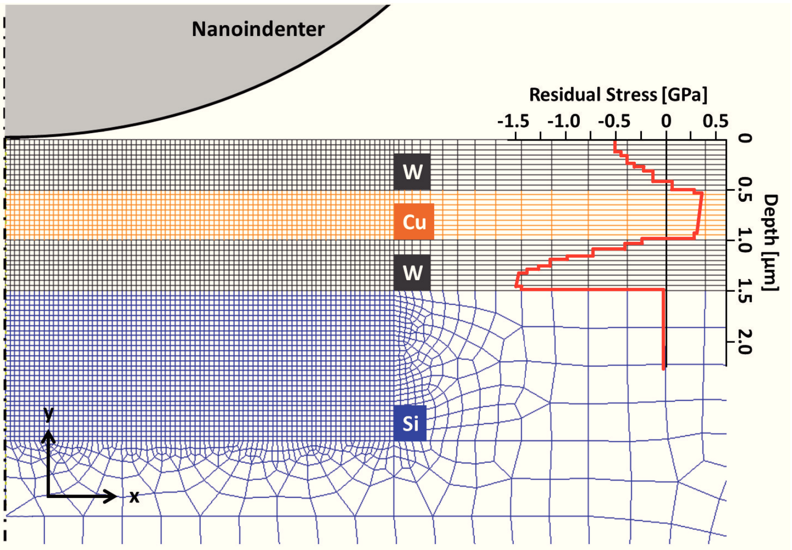

(b) Zoomed in area close to the nanoindenter tip to show the mesh resolution. Also, the residual stress distribution from Figure 17 is projected onto the mesh.

Figure 22: Axial symmetric FE model of the W-Cu-W probe.

### 7.3.2 *Relating the finite element model to the experiment*

After a ”master” model of the nanoindentation experiment has been created, an optimization routine which calculates the inverse hardening parameter $m$ and the yield strength $\sigma_0$, defined in Equation 35, of a given material is initiated. The FE model and the Ramberg-Osgood stress-strain relation are coupled by the Levenberg-Marquardt algorithm. A bounded least-squares optimization is used to assess the difference between the target experimental force-displacement response and the results from the simulations. A Python script reads the master input file and looks for the line where the material properties of the model are generated. Note that the master model is generated with the elastic properties from Table 2 which do not change during the optimization. With the initially defined guess for the parameter set $[\sigma_0, m]$, the script creates a flow curve for the given material and saves it as its first ”slave” file. A simulation is performed with the slave model and the resulting force-displacement response is compared to the corresponding experimental data. The least-squares algorithm decides whether or not the results are within a given tolerance and if the optimization should be continued or terminated. If the result is satisfactory, the optimization is complete and the optimization parameters $\sigma_0$ and $m$ are returned. If, on the other hand, the deviation between the experimental and simulated force-displacement data is too large, the algorithm keeps suggesting new pairs of optimization parameters $[\sigma_0, m]$ and performs simulations with slave models until the desired result is achieved.

In order to calculate an appropriate stress-strain relation for the W as well as the Cu film, the problem is divided into two steps. As a first step the plastic behavior of W in the W-W specimen is optimized. Secondly, the flow behavior of W is used to characterize the Cu film in the W-Cu-W stack. An optimization is performed for each experimental loading curve from Figure 21 and the corresponding optimized load-displacement data is shown in Figure 23. The parameters matching the calculated curves are listed in Table 4.

Just like the experimental curves, the six numerically determined force-displacement curves coincide very well. This allows calculating an average loading behavior for both materials and compare the experimental and numerical results. In Figure 24, the pair of the black solid line and black dots represents the comparison for the W film and the red solid line paired with the red triangles shows the comparison for the Cu film. An average loading behavior corresponds to an average yield and hardening behavior of the six parameter sets in Table 4. The inversely determined $\delta = 0.2\%$ offset parameters are $[\sigma_0, m] = [1.91 \pm 0.03 GPa, 13.3 \pm 0.3]$ for W in the W-W specimen and $[0.65 \pm 0.04 GPa, 2.8 \pm 0.1]$ for the Cu film in the W-Cu-W tri-layer stack configuration.

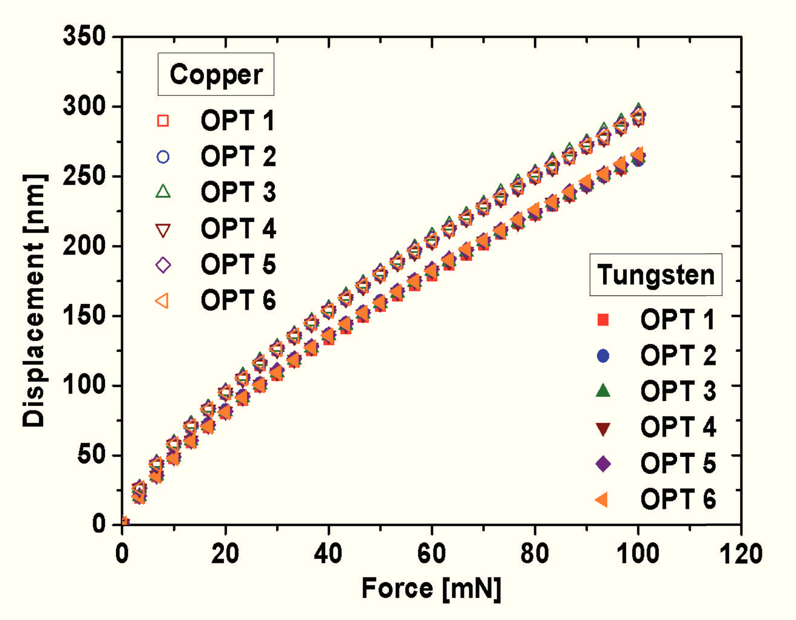

Figure 23: Numerically determined loading data for all six W-W models (closed symbols) and the W-Cu-W models (open symbols).

| Sample | Test | $\sigma_0$ [GPa] | $m$ |
|---|---|---|---|
| W-Si | 1 | 1.91 | 13.0 |
| | 2 | 1.88 | 13.3 |
| | 3 | 1.90 | 13.4 |
| | 4 | 1.91 | 13.5 |
| | 5 | 1.88 | 13.6 |
| | 6 | 1.96 | 12.8 |
| | MV | $1.91 \pm 0.03$ | $13.3 \pm 0.3$ |
| W-Cu-W-Si | 1 | 0.66 | 2.7 |
| | 2 | 0.71 | 2.8 |
| | 3 | 0.59 | 2.9 |
| | 4 | 0.68 | 2.8 |
| | 5 | 0.61 | 2.7 |
| | 6 | 0.65 | 2.7 |
| | MV | $0.65 \pm 0.04$ | $2.8 \pm 0.1$ |

Table 4: Optimized yield strength and inverse hardening parameters. MV denotes the mean value including the standard deviation calculated from the six parameter sets $[\sigma_0, m]$.

## 7.4 FLOW BEHAVIOR OF THE THIN TUNGSTEN AND COPPER FILMS

Finally, the stress-strain behavior calculated according to Equation 35 with the mean parameter sets listed in Table 4 for the two respective materials are shown in Figure 25.

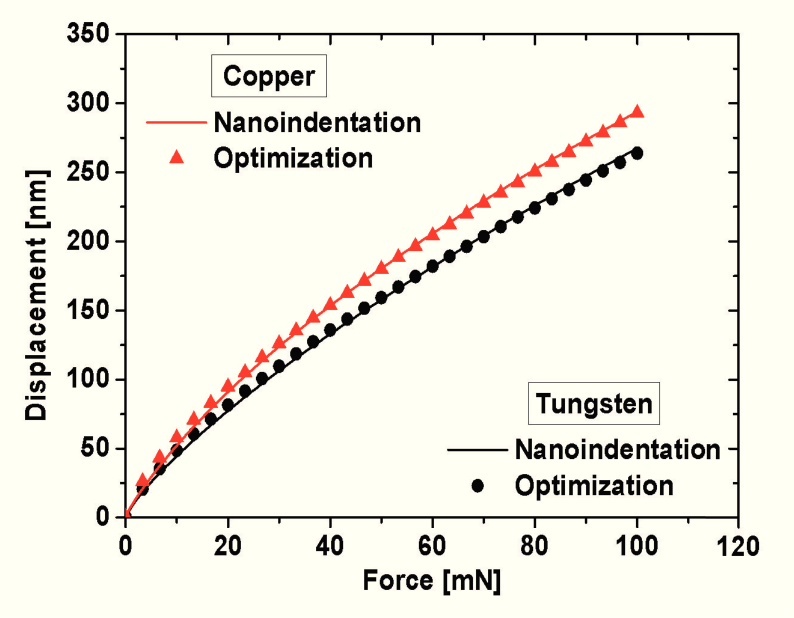

Figure 24: Comparison of the mean simulated and experimental data for the two stack configurations showing excellent agreement. The solid lines represent the experimental curves and the corresponding simulated data is marked with symbols.

The flow curve for W is denoted by the gray solid line and the stress-strain curve for Cu is drawn by the orange dashed-dotted line. For comparison, the optimizations were additionally performed without considering the residual stresses. As denoted by the black dashed line, including or excluding residual stresses in the simulations does not have a significant impact on the resulting flow and hardening behavior of W. The difference between the results lies within the numerical accuracy, which is also evident from Table 4. For Cu, however, this is not the case. By excluding the residual stress gradient in the simulations, the resulting flow curve deviates from the original curve by the average tensile residual stress of about $0.34\,\mathrm{GPa}$ occupying the Cu-layer in the W-Cu-W stack, see Figure 17. Note that the intrinsic strength of a material does not depend on the residual stresses. However, they impose internal loading on the material. These initial stresses influence the overall stress state and therefore have an impact on the flow behavior of the material in the model. Therefore, thin film stacks should be characterized taking into account their internal loading, especially for materials with higher ductility, such as Cu.

## 7.5 DISCUSSION AND SUMMARY

Finally, the results are critically compared and related to results from literature. In a recent publication [81], the experiments on single-crystalline W nanopillars have shown that the compressive and tensile $0.2\%$ offset yield strength lies in the range of $1.3\text{-}1.5\,\mathrm{GPa}$

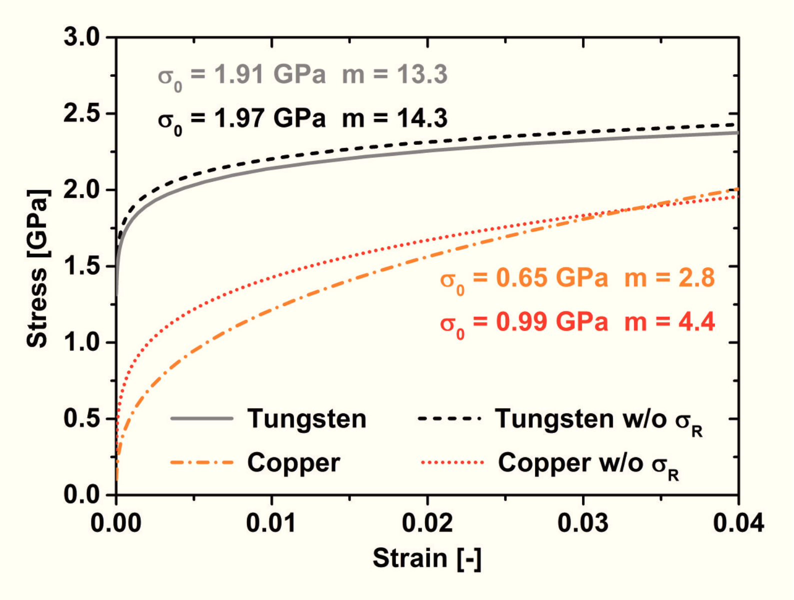

Figure 25: Stress-strain relation for W (grey solid line) and Cu (orange dash-dotted line). Flow curves resulting from the optimization procedure without considering the presence of residual stresses for W (black dashed line) and Cu (red dotted line) are also shown. The curves where the residual stresses are considered correspond to the mean values of the parameter sets $[\sigma_0, m]$ in Table 4.

for roughly $0.5\mu m$ thick samples. It is proposed that the difference to the current result of $1.91 GPa$ can be mainly attributed to the nanocrystalline structure of the films with a grain size between 60 and $70 nm$. Such a grain size effect in thin films was also shown in [91]. On the other hand, previous studies have shown that nanocrystalline Cu can display quite a high yield strength, around $0.76 GPa$ for a mean grain size of about $30 nm$ [85, 92]. In a first estimation, this value agrees well with our result, which is $0.65 GPa$. As the Cu-layer in the present study has somewhat larger grains, a lower yield strength could be expected. An estimation using the classical Hall-Petch relation, where the yield strength depends inversely on the grain size, gives $0.47 GPa$ with the Hall-Petch constants for Cu of $\sigma_r = 25 MPa$ and $k_y = 0.11 MPa\sqrt{m}$ taken from [93]. Here, $\sigma_r$ denotes the starting stress for dislocation movement and $k_y$ is the strengthening coefficient. However, the above yield strength of $0.76 GPa$ from literature was obtained for a bulk nanocrystalline Cu component that was presumably free from residual stress, while in this work a $0.5\mu m$ thin Cu film with at most eight grains over the thickness is investigated. Additionally, the Cu-layer is exposed to residual stresses. It was already shown in recent work that, just like a decreasing grain size, also a reduced film thickness can impose an effect on the yield and hardening behavior of thin films on a substrate [91]. Additionally, the Cu film in the W-Cu-W sample is constrained by two stiff W-layers, which is also contributing to the overall strength of Cu. It appears that a similar strength can be achieved by varying the internal structure, external dimensions and constraints of the same material.

In this part nano-sized W and Cu films were investigated with respect to their flow behavior. On the basis of a continuum mechanical approach a 0.2% yield strength $\sigma_0$ and inverse hardening parameter $m$ were determined for both materials. The calculations were realized by a combination of nanoindentation experiments and numerical modeling. The influence of the microstructure, external dimensions as well as the architecture on the material behavior of the thin W and Cu films was addressed. Additionally, it was shown that a residual stress state has to be considered when calculating the flow behavior of a ductile material, such as Cu. Moreover, the sequence of materials within the stack is important since adjacent layers influence each other with respect to their material behavior. As W is the stiffer material in the W-Cu-W specimen, the deformation behavior of the Cu-layer is influenced by the two constraining W-layers. The presented results were also published in a recent paper [71].

The investigations in the upcoming part about the fracture behavior of thin film stacks is going to show that it is important to consistently consider the internal and external influences in the process of material characterization.

# Part IV

# CRACK DRIVING FORCE IN THIN METALLIC FILM STACKS

In the following part, the influence of the previously calculated residual stress distributions and the material behavior on the crack driving force in thin metallic film systems is investigated. In the framework of the configurational force concept the material inhomogeneity effects due to the residual stress state and the material behavior discrepancy in the stacks are determined. Early results were published in [94, 95] and fracture properties of thin films were reported in [70]. The final results are part of an ongoing investigation and are planned to be published in the near future [96].

# 8

# MODELING FRACTURE OF THIN FILM COMPOSITES

## 8.1 MOTIVATION

As discussed in Part iii, miniaturized materials such as thin films exhibit higher strength compared to their bulk counterparts. In principle designers prefer to work with high strength materials, but it is very important to note that an increase in strength is in most cases accompanied by a limited or lower resistance to fracture. By purposeful utilization of material inhomogeneities, the fracture toughness of components can be significantly improved. The use of material variations to increase the fracture resistance of functional materials has been the topic of several investigations in the past, see [**Kubair2011**, 4, 20, 21, 97–102]. One of the most prominent fields where thin film composites are beneficial is microelectronics [103, 104]. It is very common to fabricate structures with alternating hard and soft layers. For this kind of thin film arrangement, scientists are primarily inspired by natural structures [30, 31, 99, 105–107]. For instance, deep sea sponges have a multi-layered structure consisting of a stiff and strong glass matrix which incorporates thin and soft protein interlayers serving as crack stoppers. What happens in such materials is that the crack driving force is drastically decreased as soon as the crack arrives in the soft layer [31, 107]. Thereby, the fracture toughness of the structure becomes significantly higher without suffering a noticeable loss in stiffness or strength. Other examples of natural composites which exceed the properties of their constituents would be hybrid materials that are highly mineralized (e. g. bone and teeth) or are purely polymeric, such as wood, bamboo or silk. However, examples from nature are often very hard to produce artificially.

Additionally, thin film components are subjected to residual stresses, which was investigated in Part ii of the thesis. Most importantly, the residual stresses are locally resolved, which has implications on the fracture behavior of thin film stacks. Regarding the fracture behavior of functional materials, analysis of experimental results has shown that residual stresses influence the materials crack growth resistance [108–111].

Currently, it is very important to precisely understand the material behavior as well as the magnitude and distribution of residual stresses in thin films. With the appropriate tools, the failure behavior in thin film systems can be properly investigated or even predicted. In the following, the numerical implementation of the configurational force concept, as introduced in Section 3.3, is described. The crack driving force can be calculated by following up on a conventional FE analysis with a post-processing routine based on the configurational force concept.

## 8.2 NUMERICAL MODEL FOR THE CALCULATION OF THE CRACK DRIVING FORCE

### 8.2.1 *Numerical derivation of the crack driving force*

The configurational forces, which determine the crack driving force in the material stacks, are calculated with a post-processing routine written in Python. The basics for the numerical calculation of configurational forces were introduced by Mueller et al. [112, 113]. To calculate the configurational forces the post-processing tool collects the displacement, stress and strain energy fields from the FE simulations in ABAQUS for each node in the model. With this data at hand, the configurational stress tensor **C** from Equation 40 can be readily obtained. In Figure 26 four adjacent elements with their respective integration points (+) are depicted. The nodes are marked by red dots. A configurational force vector in a node $K$ of a single element $e$ is then determined by:

$$\mathbf{g}_K = \int_{V_e} N_K \mathbf{f} dV = \int_{V_e} \mathbf{D}_K^{\mathrm{T}} \cdot \mathbf{C} dV, \tag{59}$$

where

$N_K$ Shape functions,

$\mathbf{D}_K^{\mathrm{T}}$ Transposed derivatives of shape function w.r.t. nodal coordinates,

$V_e$ Element volume.

The integration is performed numerically with Gauß quadrature while considering that $dV = w dA$, and $w$ is the specimen width. Finally, the configurational forces from all elements adjacent to the same node $K$ are summed up to give the resulting configurational force vector in the node:

$$\mathbf{g}_K = \sum_{e=1}^{n_e} \mathbf{g}_K^e, \tag{60}$$

where $n_e$ is the number of adjacent elements $e$. The scalar $J$-integral in a region $\mathcal{D}$ which includes $k$ nodes and is enclosed by a contour $\Gamma$ is calculated as

$$J_\Gamma = \sum_{k \in \mathcal{D}} -(\mathbf{e} \cdot \mathbf{g}_K) \Delta A_k. \tag{61}$$

In Equation 61, $\Delta A_k$ is the area enclosed by $\Gamma$, as shown in Figure 26.

In Figure 27a, a simple model of a loaded compact tension specimen is given. The configurational forces around the crack tip are calculated and presented as vectors in Figure 27b. The largest vector lies at the node directly at the crack tip. According to

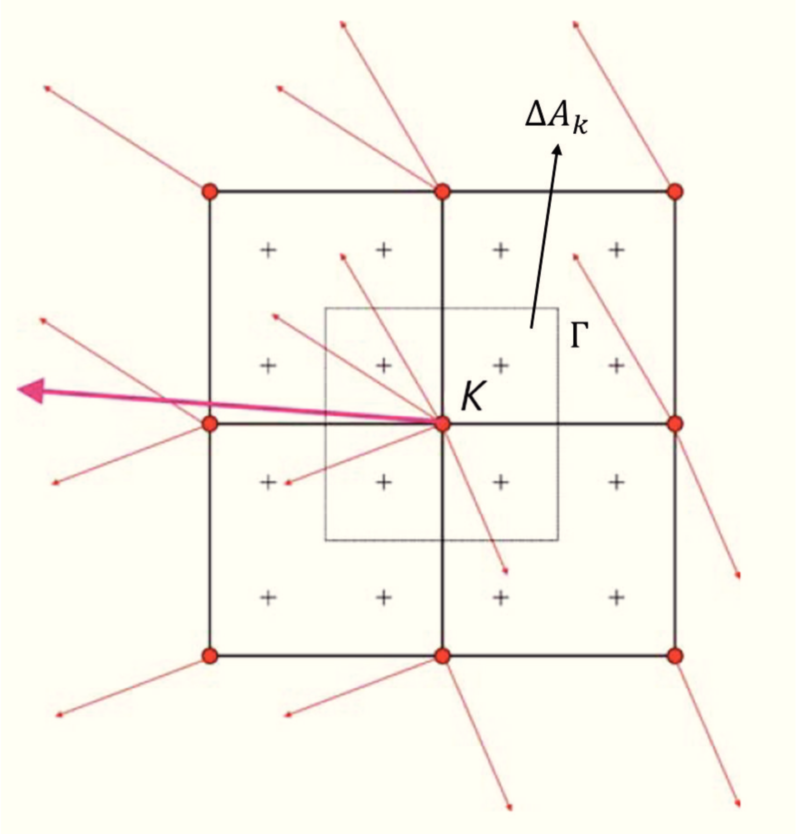

Figure 26: Four adjacent elements with the corresponding integration points (+). The configurational forces assembled at the nodes calculated at their adjacent elements are shown by exemplary vectors (red arrows). Also, the integration area around the node $K$ is depicted.

theory, this should be the only configurational force which appears, as a homogeneous body is considered. However, the nodes surrounding the crack tip node show small configurational forces. They appear due to numerical inaccuracies, since the four-node linear elements, used in this example, cannot completely resemble the singularity at the crack tip, see e. g. [19]. By accordingly refining the mesh in a given model, those inaccuracies can be minimized and reduced to a very narrow area around the crack tip.

As is suggested by Equation 46, the configurational force for a node at an interface is derived from the difference of the configurational stress tensor on one and its adjacent side of the node. To realize this numerically, the post-processing script has to be provided with the concerning node and, separately, the corresponding elements on each side of the node. Finally, the configurational force at the interface node $K$ is determined as

$$\mathbf{g}_{\Sigma,K} = \left(\mathbf{g}^{+}_{\Sigma,K} - \mathbf{g}^{-}_{\Sigma,K}\right)\mathbf{e}, \tag{62}$$

where $\mathbf{g}^{+}_{\Sigma,K}$ represents the configurational force on one side and $\mathbf{g}^{-}_{\Sigma,K}$ the configurational force on the adjacent side. In comparison to Equation 46, the unit normal vector

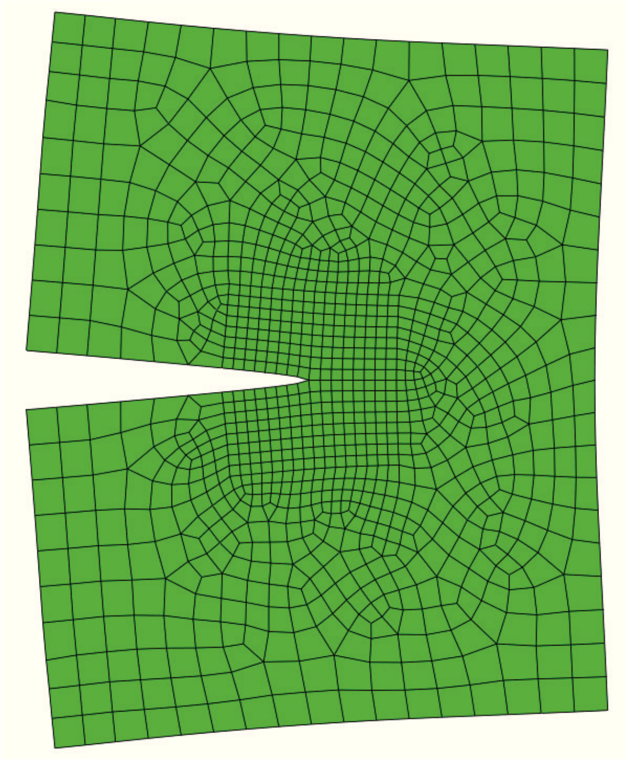

(a) Meshed model of a loaded compact tension specimen.

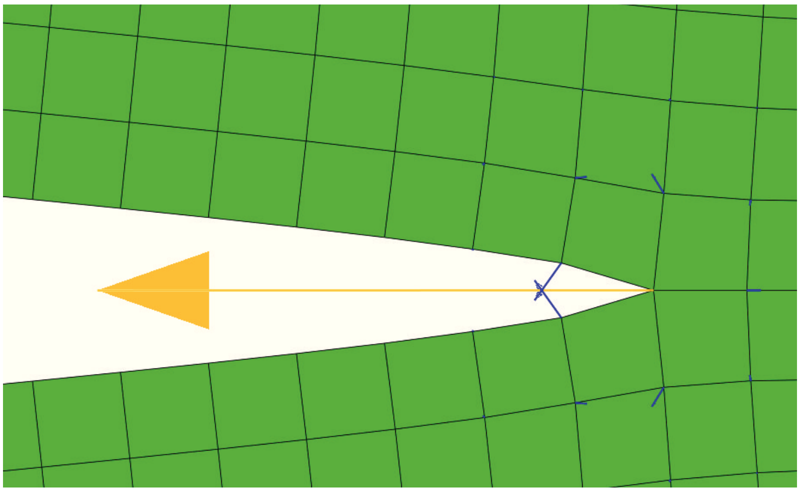

(b) Area around the crack tip with the configurational force at the crack tip (orange arrow) and the configurational forces resulting from mesh resolution (blue arrows).

Figure 27: Simple FE model to demonstrate the calculation of configurational forces.

to the interface is equal to the crack propagation direction. In the models presented in this thesis this is always the case. In a scenario where a crack lies very close to an interface, a part of the configurational force from the interface nodes redistributes to the nodes adjacent to them; again due to numerical inaccuracies. In this case the total configurational force around the interface, $\mathbf{g}_{\Sigma}$, is the sum of the configurational forces at the interface and the nodes adjacent to it.

### 8.2.2 *Finite element model*

The FE models are based on micro-cantilevers prepared for fracture experiments, where the fracture toughness of the thin films in the multilayer stacks under mechanical loading was investigated [70]. As shown in the SEM picture of the W-Cu-W stack in Figure 28a the fracture samples are prepared in a very similar fashion as the samples fabricated for the residual stress calculations. In this way, the residual stress distributions from Part ii are appropriately considered. In order to create a model, the necessary geometries are determined from the SEM pictures. As denoted in Figure 28a, the distance between the crack and beam fixation is $c$ and $l$ is the gap between the loading point L and crack. Moreover, the total beam height $h$, width $w$ and thickness of each thin film are measured from SEM pictures at higher magnification. The geometries for the W-Cu-W and Cu-W-Cu specimen are listed in Table 5, and the film dimensions are given in Table 1.

| Stack | $c$ [μm] | $l$ [μm] | $h$ [μm] | $w$ [μm] |
|---|---|---|---|---|
| W-Cu-W | 6.79 | 20.50 | 4.50 | 3.76 |
| Cu-W-Cu | 3.80 | 21.90 | 4.50 | 4.10 |

Table 5: Micro-beam geometries used for FE modeling.

In the course of the discussion the results of the so-called "bare" model and the "full" model are compared. The bare model behaves exclusively linear elastic and the full model includes the elastic-plastic material behavior, as presented in Figure 25 and the residual stress gradients from Figure 17 and Figure 18, depending on which thin film stack is modeled. The elastic material properties from Table 2 are considered in the models. Figure 28b shows the 2D plane strain model for the W-Cu-W stack with the respective boundary conditions. The exact same model is created multiple times for different crack lengths of a stationary crack. In this way the crack is propagated through the material system for crack lengths between 0.1 and 1.475μm. This is automatically performed with a Python script. The models are meshed with four-node bilinear plane strain elements (CPE4). Special attention is paid to meshing the crack tip. An area around the crack tip, covering the thickness of the layer and double the thickness in lateral direction, is meshed with square shaped elements with a constant size of 0.005μm. The area around the crack tip is shown in Figure 28c. By using this element size, it is possible to accurately model cracks which are a distance of 0.025μm appart from the closest inter-

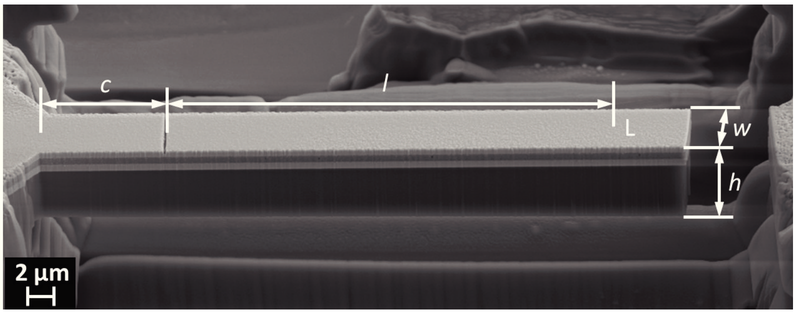

(a) SEM scan of the W-Cu-W fracture specimen.

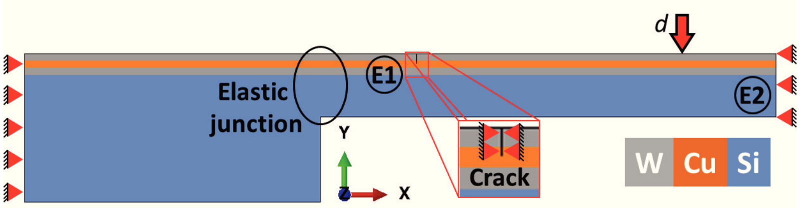

(b) Boundary conditions for the FE model of the W-Cu-W specimen.

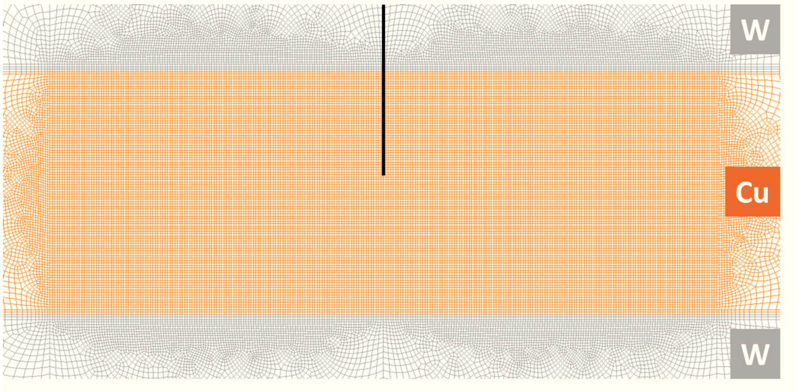

(c) The mesh in the vicinity of the crack tip.

Figure 28: The setup for the FE model of the W-Cu-W micro-cantilever.

face. A free mesh has been put on the remaining area with the constraint that the largest elements do not exceed a size of $0.3\mu m$. In order to properly calculate the material inhomogeneity term at the thin film boundaries, also the mesh around the sharp interfaces is resolved with the smallest elements.

Note that, the residual stresses in the thin film stacks are nto a consequence of a mismatch of the thermal expansion coefficient, as the thin films were deposited at room temperature. In the full model, the residual stresses are imposed on the element integration points of an uncracked specimen in the initial step via the user subroutine SIGINI. The residual stresses act in the lateral cantilever direction. This implementation method was verified by calculating the far-field $J$-integral, $J_{far}$, with the post-processing tool as well as the virtual crack extension (VCE) method provided by ABAQUS. It was confirmed that both approaches yield the same results for $J_{far}$.

A crack in the model is defined by a so-called ”seam”. With this feature, a line of nodes is duplicated, introducing a sharp crack. The crack plane lies transverse to the interfaces and the crack propagation direction is defined by the vector $(0.0, -1.0)$. Initially, the flank nodes are fixed in all directions, as shown in the insert of Figure 28b. Following that, the residual stresses in the full model are equilibrated by releasing the crack flank nodes, denoted by equilibration step E1 in Figure 28b. After that, the front of the beam is released in the second equilibration step E2, redistributing the residual stresses one more time. This procedure resembles the residual stress redistribution after a thin notch is cut into the sample and the subsequent release of the beam on one end by FIB milling.

The micro-beam is monotonically loaded with a constant load line displacement of $d = 1.5\mu\text{m}$ in the loading point L, as shown in Figure 28a and Figure 28b, respectively. While the cantilever is under load, the back side of the beam remains constrained in all directions as the box foot remains unconstrained. By choosing this kind of constraint, the simulated force-displacement behavior shows a good agreement with the mechanical response of the micro-beam compared to the experiment, which was demonstrated in [70].

# 9

# INFLUENCE OF SHARP INTERFACES AND RESIDUAL STRESSES ON THE CRACK DRIVING FORCE

## 9.1 MATERIAL INHOMOGENEITY EFFECT

The material inhomogeneity effect depends on the material properties of the layers, the residual stress distribution and also the film sequence. The interface and gradient terms as well as the total material inhomogeneity terms are presented for the W-Cu-W and Cu-W-Cu stacks in Figure 29 and Figure 30. The different inhomogeneity terms are plotted for stationary cracks with increasing crack length.

### 9.1.1 *W-Cu-W stack*

The first results are obtained for the bare W-Cu-W model, as shown in Figure 29a. As the residual stress state is neglected in the bare model, the gradient inhomogeneity term $C^{\mathrm{GR}}$ is zero for all crack lengths. Thus, the interface inhomogeneity term $C^{\mathrm{IF}}$, drawn as the black solid line with circles, and the total material inhomogeneity term $C_{\mathrm{inh}}$, plotted as the red solid line with squares, overlap. W has a larger Young's modulus $E$ than Cu and Si. Therefore, a crack approaching the W/Cu and W/Si interface experiences an increasing anti-shielding effect. However, as the crack extends through the Cu film, the Cu/W interface is starting to shield the crack tip. Shielding starts after the crack reaches approximately the length of $0.7\mu\mathrm{m}$ and $C^{\mathrm{IF}}$ and in this case also $C_{\mathrm{inh}}$ become negative. Theoretically, $C^{\mathrm{IF}}$ has its minimum exactly at the interface, which is not possible to realize in the FE model.

Figure 29b shows the results of the full model, taking into account the residual stress distribution from Figure 17 and elastic-plastic material behavior from Figure 25. The gradient inhomogeneity term $C^{\mathrm{GR}}$ is plotted as green solid line with triangles. Due to lower residual stresses and a relatively plane stress distribution, the gradient inhomogeneity term $C^{\mathrm{GR}}$ is small in the first W-layer and negligible in the Cu-layer. As soon as the residual stress gradient steepens in the second W-layer and the compressive residual stress exceeds approximately $1\mathrm{GPa}$ at a crack length of $1.1\mu\mathrm{m}$, a strong shielding effect is evident. However, the interface and gradient inhomogeneity term have counteracting effects and the resulting total material inhomogeneity term is small.

The influence of the residual stress distribution is evident from Figure 29c, where the total material inhomogeneity terms for the full model and for the bare model are compared. Here, the red line with squares denotes the result for the full model and the black line with triangles represents the bare model. As the crack tip is noticeably shielded by the negative compressive stress gradient in the bottom W-layer in the full model, most of the anti-shielding present in the bare model is annihilated or even reverted into a slight shielding effect. This will have implications when calculating the crack driving force in Section 9.2.

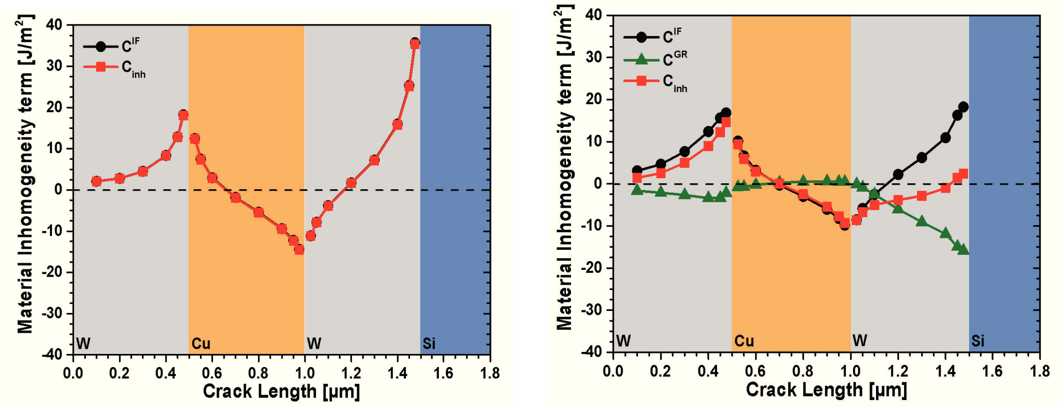

(a) Interface inhomogeneity term $C^{IF}$ (black line with circles) and the total material inhomogeneity term $C_{inh}$ (red line with squares) for the bare model.

(b) Interface inhomogeneity term $C^{IF}$ (black line with circles), gradient inhomogeneity term $C^{GR}$ (green line with triangles) and the total material inhomogeneity term $C_{inh}$ (red line with squares) for the full model model.

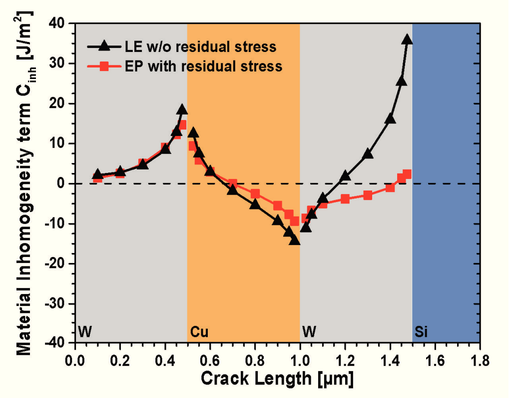

(c) Comparison of the total material inhomogeneity term $C_{inh}$ for the bare model (black line with triangles) and the full model (red line with squares).

Figure 29: Behavior of the material inhomogeneity terms depending on the growing stationary crack for the W-Cu-W model.

### 9.1.2 *Cu-W-Cu stack*

Figure 30a shows the results for the interface inhomogeneity term $C^{IF}$ and the total material inhomogeneity term $C_{inh}$ for the bare model of the Cu-W-Cu specimen. Again, as the bare model does not incorporate a residual stress distribution, the gradient inhomogeneity term is zero.

It is nicely demonstrated, that the Cu/W interface provides a shielding effect to an approaching crack. In addition, the Cu/Si interface is also slightly shielding the crack from propagation very close to the interface. In contrast, the W/Cu interface has an

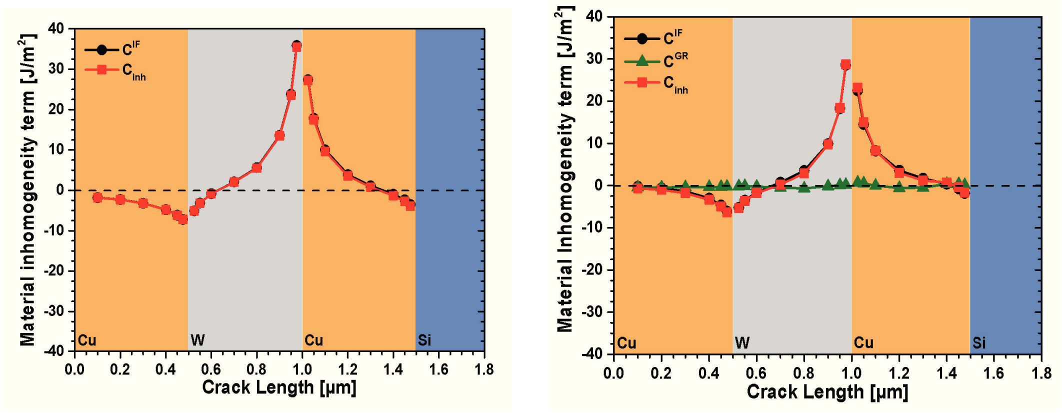

(a) Interface inhomogeneity term $C^{IF}$ (black line with circles) and the total material inhomogeneity term $C_{inh}$ (red line with squares) for the bare model.

(b) Interface inhomogeneity term $C^{IF}$ (black line with circles), gradient inhomogeneity term $C^{GR}$ (green line with triangles) and the total material inhomogeneity term $C_{inh}$ (red line with squares) for the full model model.

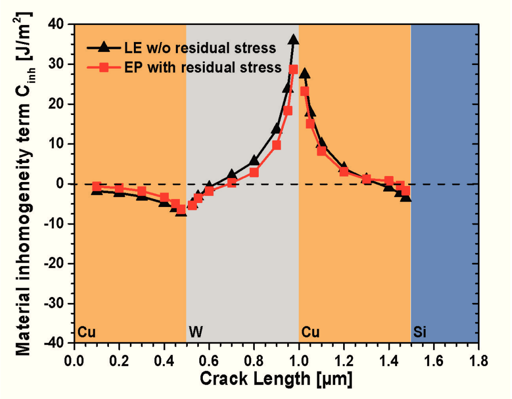

(c) Comparison of the total material inhomogeneity term $C_{inh}$ for the bare model (black line with triangles) and the full model (red line with squares).

Figure 30: Behavior of the material inhomogeneity terms depending on the growing stationary crack for the Cu-W-Cu model.

anti-shielding effect on the crack tip.

After introducing the residual stress gradient from Figure 18 and the elastic-plastic material behavior from Figure 25, the material inhomogeneities for the full model are calculated. The corresponding results are presented in Figure 30b. Notably, the residual stresses in the Cu-W-Cu stack on average never exceed $0.3\mathrm{GPa}$ in tensile or compressive direction, which can be readily calculated from Figure 18. Thus, the gradient inhomogeneity term $C^{\mathrm{GR}}$, plotted as the green solid line with triangles, is zero and does not have any influence on the total material inhomogeneity term $C_{\mathrm{inh}}$, presented as red solid line with squares, which is almost identical to the interface inhomogeneity term $C^{\mathrm{IF}}$, marked as black solid line with circles. Furthermore, we compare the total material inhomogeneity terms from the bare model and the full model in Figure 30c. As the effect from the residual stress distribution is neglectable, the total material inhomogeneity terms are comparable.

## 9.2 EFFECTIVE CRACK DRIVING FORCE

### 9.2.1 *W-Cu-W stack*

The effective crack driving forces for stationary cracks with increasing length are calculated according to Equation 44. The bare model and the full model for the W-Cu-W film distribution are compared in Figure 31. It is shown how the $J_{\mathrm{tip}}$ values compare to a stress intensity factor under critical conditions from experiments. In [70] the critical stress intensity factor $K_C = 3.3\mathrm{MPa}\sqrt{\mathrm{m}}$ was calculated for the top W-layer in the W-Cu-W film system. This was realized by combining fracture mechanics testing and FE modeling. Further details can be found in [70]. We consider that the critical crack driving force $J_C$ is determined by

$$J_C = K_C^2 \cdot \frac{1-\nu^2}{E}, \tag{63}$$

where $E$ is the Young's modulus and $\nu$ is the Poisson's ratio. Inserting $K_C$ into Equation 63, $J_C$ amounts to $24.3\mathrm{J/m^2}$. A crack in W can propagate if the crack driving force equals or exceeds this critical value. In this case, the top W-layer would fail at a crack length $a = 0.45\mu\mathrm{m}$ for the bare model and the full model, as marked by the encircled points in Figure 31. Furthermore, it is assumed that the critical stress intensity factor is also valid for the second W-layer and that the crack is situated in this layer. As highlighted by the circle around the black triangle in the W-layer on top of Si, $J_{\mathrm{tip}}$ exceeds $J_C$ for $a = 1.1\mu\mathrm{m}$ in the bare model. This crack length shifts to $1.3\mu\mathrm{m}$ in the full model. Thus, a cracked micro-cantilever beam which seems to fail in the bare model is shielded from propagation by the residual stress state. Therefore, it is obviously important that the residual stress distribution is taken into account in the FE model. Otherwise, wrong predictions about the critical conditions for components with a similar structure would be the consequence.

Moreover, imagine a specimen which contains only a single W-layer deposited on top of the Si wafer. In principle, the $J_{tip}$ value would increase linearly and for any crack length surpassing 0.45µm the specimen would fail. As evident from Figure 31, in the multilayer stack the soft Cu-interlayer offers an arresting environment for a crack propagating from the surface of the cantilever. After the top W-layer fails and the crack enters the Cu-interlayer the crack driving force decreases due to the repelling effect of the Cu/W interface, while the load line displacement remains the same and the crack length increases. Therefore, in order to achieve further crack propagation, the external load on the micro-beam has to be strongly increased. Moreover, the inherent fracture toughness of Cu is higher compared to W, which requires the load to be even higher.

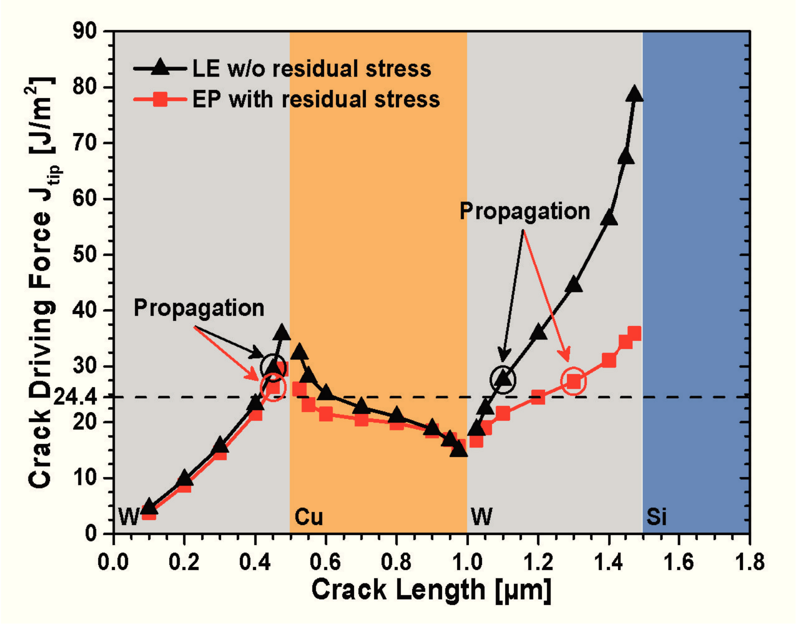

Figure 31: The crack driving forces $J_{tip}$ in the W-Cu-W stack for the bare model (black line with triangles) and the full model (red line with squares) are compared. The critical crack positions in the W-layers are encircled.

### 9.2.2 *Cu-W-Cu stack*

As the gradient inhomogeneity term $C^{GR}$ does not play a role in the Cu-W-Cu film stack, see Figure 30b, the effective crack driving force $J_{tip}$ is driven by the sum of the far-field $J$-integral and the interface inhomogeneity term $C^{IF}$. Considering the same loading conditions as for the W-Cu-W models, the crack driving force in the top Cu-layer does not even reach the critical $J_C$ value, as shown in Figure 32. Since Cu has a lower yield strength and behaves more ductile than W, it can be assumed that $J_C$ is significantly higher for Cu. Thus, $J_{\mathrm{tip}}$ is far from reaching the critical $J_C$ for Cu which is necessary for crack propagation. However, it is safe to assume that $J_C = 24.3\mathrm{J/m^2}$ is also valid for the W-interlayer in the Cu-W-Cu stack. If a crack were present through the first Cu-layer into the W-interlayer, the crack length where the W-interlayer fails in the bare as well as the full model is $a = 0.7\mu\mathrm{m}$. Moreover, for both models, the crack driving force strongly increases as the crack is further extended through the W-interlayer. Although $J_{\mathrm{tip}}$ decreases after the crack enters the Cu-layer, it remains relatively high compared to the crack driving force calculated for the full model of the W-Cu-W thin film stack, see Figure 31. As we do not have any results on the critical stress intensity factor for the thin Cu film, we cannot predict if the conditions in the second Cu-layer are critical or not. However, in the experiments fracture in the Cu-layers was not observed. Thus, the experiments indicate that $J_C$ for Cu should be much higher than for W. Altogether, for material systems which behave similar to the Cu-W-Cu stack, a very good estimation about the critical conditions can already be made by means of the bare model, i. e. a linear elastic model.

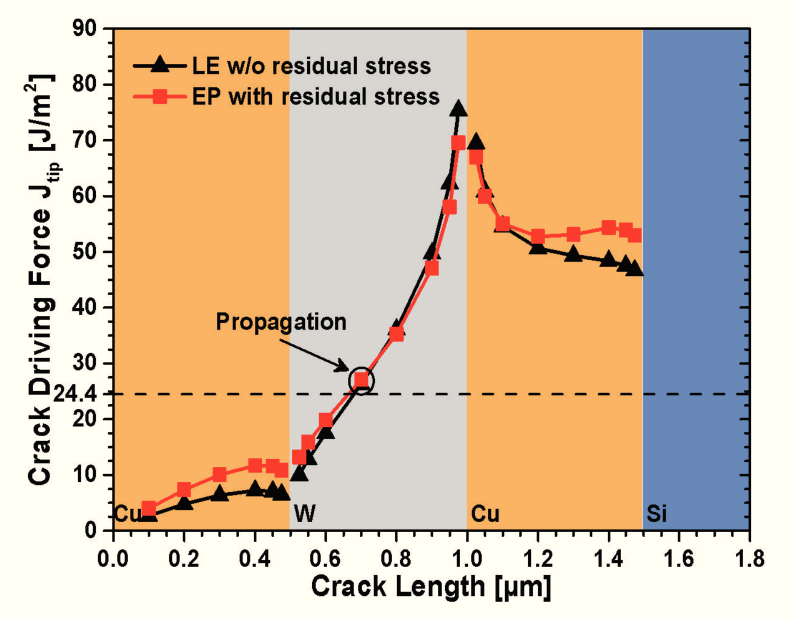

Figure 32: The crack driving forces $J_{\mathrm{tip}}$ in the Cu-W-Cu stack for the bare model (black line with triangles) and the full model (red line with squares) are compared.

## 9.3 SUMMARY

The crack arresting capabilities of two thin film systems have been investigated exemplarily for a W-Cu-W stack configuration and a Cu-W-Cu stack configuration. In summary, our work demonstrated that:

1. The soft Cu interlayer provides the W-Cu-W material system with the ability to diminish crack driving forces. Ultimately, the crack can be arrested at the transition from the softer to the harder material in the W-Cu-W stack.
2. It was demonstrated that a compressive residual stress gradient can significantly decrease the crack driving force in front of a crack tip. In the case of the W-Cu-W stack, the crack experiences a strong shielding effect from the compressive residual stresses in the bottom W-layer, as soon as they reach and increase beyond $1\,\mathrm{GPa}$. Certainly, this is not a threshold value that should be considered for any material system. The influence of the residual stress state on the crack driving force in a thin film stack depends on the external loading conditions and also the dimensions and composition of a stack.
3. It was shown that the anti-shielding effect of an interface can be countered by the shielding effect of the compressive residual stress state. The consequence is that the initially stressed component with a given crack withstands failure, in contrast to an originally stress free one. This was demonstrated by comparing the bare model with a full model.
4. Despite experiencing a low crack driving force in the top Cu-layer, the Cu-W-Cu stack does not benefit from a favorable residual stress distribution.
5. Due to the crack arresting effect of the Cu-interlayer and an appropriate compressive residual stress gradient in the bottom W-layer, it can be ensured that the crack driving force in the W-Cu-W stack remains relatively low for a crack growing through the whole structure.

# Part V

# EPILOGUE

# 10

# CONCLUSION AND OUTLOOK

The processing of thin films in microelectronic components can be beneficial for the functionality and reliability of a device. Furthermore, thin films occupy a very small volume in the assembly, which makes the realization of 3D integrated circuits much easier. Nonetheless, an arbitrarily fabricated thin film component will not automatically meet the requirements concerning its reliability and persistent functionality. The design concept of a component raises questions about the internal as well as the external dimensions and also the arrangement of the incorporated thin films.

This thesis was conducted to fully characterize the mechanical properties of thin W and Cu films and their stacks deposited on Si wafers. With the appropriate methods it was possible to determine the state of internal loading in the film systems even before any external load was applied to the structures. With a rather simple but very effective analytical method, which was prefaced by sophisticated experiments, the residual stresses in the thin metal layers, i. e. the W-Cu-W and Cu-W-Cu tri-layer stacks, were calculated with high precision. In a separate publication, the results were compared to X-ray diffraction measurements, see [34].

Additionally, the thin films were characterized with respect to their material behavior. Due to the nanocrystalline nature of the investigated metal layers, we were able to numerically determine the yield and hardening behavior of W and Cu with the help of spherical nanoindentation experiments within a continuum mechanical framework. The stress-strain relation of the materials was defined by the yield strength $\sigma_0$ and the inverse hardening parameter $m$. In an optimization loop, the parameter set $[\sigma_0, m]$ was optimized to fit the resulting force-displacement curve from FE simulations to the loading data from the experiments. The results were discussed with respect to the Hall-Petch relation and critically compared to other studies. It was concluded that the grain structure, external dimensions and the constraints acting on the thin films dictate their material behavior.

Finally, the residual stress distribution and the elastic–plastic material properties of the thin W and Cu films were implemented in a model with the goal to determine the fracture behavior of the W-Cu-W and the Cu-W-Cu stacks. Using the concept of configurational forces, it was possible to explicitly distinguish between the influence of the interfaces and the residual stress gradient in the individual layers on the crack driving force. It was shown that the sequence of materials strongly dictates the crack driving force, e. g. the crack is arrested in the Cu-interlayer in the W-Cu-W stack. Furthermore, residual stresses can prevent a crack from further propagation, e. g. the resistance to failure of the W-Cu-W stack is improved by the compressive residual stress gradient in the bottom W-layer. It was discussed that, compared to the Cu-W-Cu stack, the W-Cu-W film system has a higher mechanical stability due to the thin film arrangement and the residual stress state in the W-Cu-W stack.

The fracture behavior of thin film stacks can further be improved by optimizing the relationship between the elastic and plastic properties of the involved materials. Of course, the behavior of a material can be altered through its internal and external structure, i. e. by adjusting the grain size and film thickness. On the other hand, the residual stress state is not only dependent on the sequence and dimensions of the thin films. It can easily be manipulated by the deposition process in a beneficial way.

The tools developed in this thesis give the possibility to investigate the impact of internal loading and material properties on the fracture behavior of thin film stack configurations under loading. In this context, our findings can be readily applied to an effective design of thin film material systems. In Table 6 the purpose of each tool is summarized. Additionally, the tools are collected on a compact disc and attached to the thesis.

| Name | Programing environment, Software | Purpose |
|---|---|---|
| resid_stress | Maple$^{TM}$ | Calculation of residual stress profiles in thin film stacks. |
| nanoindent | Python, ABAQUS | Inverse determination of the stress-strain behavior of thin films. |
| fract_sim | Python, ABAQUS | Calculation of the crack driving force in thin film stacks dependent on the residual stress state and material properties. |

Table 6: Set of tools developed for the full mechanical characterization of thin film stacks.

# BIBLIOGRAPHY

[1] G. E. Moore. "Cramming More Components Onto Integrated Circuits, Electronics, April 19, 1965." In: *Electronics* 38.8 (1965), pp. 82–85. ISSN: 0018-9219. DOI: 10.1109/JPROC.1998.658762.

[2] P. Lindner, T. Glinsner, T. Uhrmann, V. Dragoi, T. Plach, T. Matthias, E. Pabo, and M. Wimplinger. "Key enabling processes for more-than-moore technologies." In: *2012 IEEE International SOI Conference (SOI)*. IEEE, 2012, pp. 1–2. ISBN: 978-1-4673-2691-9. DOI: 10.1109/SOI.2012.6404360.

[3] O. Kolednik. "Fracture Mechanics." In: *Wiley Encyclopedia of Composites*. John Wiley and Sons, Inc., 2011. ISBN: 9781118097298. DOI: 10.1002/9781118097298.weoc096.

[4] R. O. Ritchie. "Mechanisms of fatigue crack propagation in metals, ceramics and composites: Role of crack tip shielding." In: *Materials Science and Engineering* 103.1 (1988), pp. 15–28. ISSN: 00255416. DOI: 10.1016/0025-5416(88)90547-2.

[5] N. K. Simha, F. D. Fischer, O. Kolednik, and C. R. Chen. "Inhomogeneity effects on the crack driving force in elastic and elastic-plastic materials." In: *Journal of the Mechanics and Physics of Solids* 51.1 (2003), pp. 209–240. ISSN: 00225096. DOI: 10.1016/S0022-5096(02)00025-X.

[6] J. Bonet and R.D. Wood. *Nonlinear Continuum Mechanics for Finite Element Analysis*. Cambridge University Press, 2008. ISBN: 9781139467544. URL: https://books.google.at/books?id=V5Zf1rVeeEsC.

[7] P. Chadwick. *Continuum Mechanics: Concise Theory and Problems*. Dover books on physics. Dover Publications, 1999. ISBN: 9780486401805. URL: https://books.google.de/books?id=QSXIHQsus6UC.

[8] L. E. Malvern. *Introduction to the mechanics of a continuous medium*. Prentice-Hall series in engineering of the physical sciences. Prentice-Hall, 1969. URL: https://books.google.at/books?id=IIMpAQAAMAAJ.

[9] R. Abeyaratne. *Continuum Mechanics*. 2012. URL: http://web.mit.edu/abeyaratne/lecture_notes.html.

[10] J. Lubliner. *Plasticity Theory*. third ed. Vol. 15. 5. New York: Dover Publications, 2006, p. 528. ISBN: 9780486462905. URL: http://www.getcited.org/pub/102800120.

[11] W. Ramberg and W. R. Osgood. "Description of stress - strain curves by three parameters." In: *National Advisory Committee for Aeronautics, Washington D.C* (1943), Technical Note No. 902.

[12] T.L. Anderson. *Fracture Mechanics: Fundamentals and Applications, Second Edition*. Taylor and Francis, 1994. ISBN: 9780849342608. URL: https://books.google.at/books?id=K_0hiig1co4C.

[13] M. Kuna. *Finite Elements in Fracture Mechanics: Theory - Numerics - Applications*. Solid Mechanics and Its Applications. Springer Netherlands, 2015. ISBN: 9789400798731. URL: https://books.google.at/books?id=OdIXswEACAAJ.

[14] X. K. Zhu and J. A. Joyce. “Review of fracture toughness (G, K, J, CTOD, CTOA) testing and standardization.” In: *Engineering Fracture Mechanics* 85 (2012), pp. 1–46. ISSN: 00137944. DOI: 10.1016/j.engfracmech.2012.02.001.

[15] G.R. Irwin. “Analysis of Stresses and Strains Near the End of a Crack Traversing a Plate.” In: *Journal of Applied Mechanics* 24.3 (1957), pp. 361–364. ISSN: 04306252. DOI: noDOI.

[16] A. A. Griffith. “The Phenomena of Rupture and Flow in Solids.” In: *Philosophical Transactions of the Royal Society A: Mathematical, Physical and Engineering Sciences* 221.582-593 (1921), pp. 163–198. ISSN: 1364-503X. DOI: 10.1098/rsta.1921.0006.

[17] J. R. Rice. “A Path Independent Integral and the Approximate Analysis of Strain Concentration by Notches and Cracks.” In: *Journal of Applied Mechanics* 35.2 (1968), pp. 379–386. ISSN: 00218936. DOI: 10.1115/1.3601206.

[18] N. K. Simha, F. D. Fischer, G. X. Shan, C. R. Chen, and O. Kolednik. “J-integral and crack driving force in elastic-plastic materials.” In: *Journal of the Mechanics and Physics of Solids* 56.9 (2008), pp. 2876–2895. ISSN: 00225096. DOI: 10.1016/j.jmps.2008.04.003.

[19] O. Kolednik, R. Schöngrundner, and F. D. Fischer. “A new view on J-integrals in elastic–plastic materials.” In: *International Journal of Fracture* 187.1 (2014), pp. 77–107. ISSN: 1573-2673. DOI: 10.1007/s10704-013-9920-6.

[20] R. O. Ritchie, W. Yu, and R. J. Bucci. “Fatigue crack propagation in ARALL® LAMINATES: Measurement of the effect of crack-tip shielding from crack bridging.” In: *Engineering Fracture Mechanics* 32.3 (1989), pp. 361–377. ISSN: 00137944. DOI: 10.1016/0013-7944(89)90309-3.

[21] O. Kolednik, J. Zechner, and J. Predan. “Improvement of fatigue life by compliant and soft interlayers.” In: *Scripta Materialia* 113 (2016), pp. 1–5. ISSN: 13596462. DOI: 10.1016/j.scriptamat.2015.10.021.

[22] Y. Sugimura, P. G. Lim, C. F. Shih, and S. Suresh. “Fracture normal to a bimaterial interface: Effects of plasticity on crack-tip shielding and amplification.” In: *Acta Metallurgica Et Materialia* 43.3 (1995), pp. 1157–1169. ISSN: 09567151. DOI: 10.1016/0956-7151(94)00295-S.

[23] J. Predan, N. Gubeljak, and O. Kolednik. “On the local variation of the crack driving force in a double mismatched weld.” In: *Engineering Fracture Mechanics* 74.11 (2007), pp. 1739–1757. ISSN: 00137944. DOI: 10.1016/j.engfracmech.2006.09.015.

[24] O. Kolednik, J. Predan, N. Gubeljak, and F. D. Fischer. “Modeling fatigue crack growth in a bimaterial specimen with the configurational forces concept.” In: *Materials Science and Engineering A* 519.1-2 (2009), pp. 172–183. ISSN: 09215093. DOI: 10.1016/j.msea.2009.04.059.

[25] N. K. Simha, O. Kolednik, and F. D. Fischer. “Material force models for cracks - influences of eigenstrains, thermal strains & residual stresses.” In: *ICF XI - 11th International Conference on Fracture*. 1. 2005. ISBN: 9781617820632. URL: http://www.icf11.com/proceeding/EXTENDED/5329.pdf.

[26] J. D. Eshelby. “Energy Relations and the Energy-Momentum Tensor in Continuum Mechanics BT - Fundamental Contributions to the Continuum Theory of Evolving Phase Interfaces in Solids: A Collection of Reprints of 14 Seminal Papers.” In: ed. by John M Ball, David Kinderlehrer, Paulo Podio-Guidugli, and Marshall Slemrod. Berlin, Heidelberg: Springer Berlin Heidelberg, 1999, pp. 82–119. ISBN: 978-3-642-59938-5. DOI: 10.1007/978-3-642-59938-5_5.

[27] M. E. Gurtin. *Configurational forces as basic concepts of continuum physics*. 1st ed. Springer-Verlag New York, 2000, p. 250. ISBN: 978-0-387-98667-8. DOI: 10.1007/b97847.

[28] G. A. Maugin. *Configurational Forces: Thermodynamics, Physics, Mathematics, and Numerics*. CRC Press Inc, 2010, p. 562. ISBN: 978-1439846124.

[29] N. K. Simha, F. D. Fischer, O. Kolednik, J. Predan, and G. X. Shan. “Crack Tip Shielding or Anti-shielding due to Smooth and Discontinuous Material Inhomogeneities.” In: *International Journal of Fracture* 135.1 (2005), pp. 73–93. ISSN: 1573-2673. DOI: 10.1007/s10704-005-3944-5.

[30] O. Kolednik, J. Predan, F. D. Fischer, and P. Fratzl. “Bioinspired design criteria for damage-resistant materials with periodically varying microstructure.” In: *Advanced Functional Materials* 21.19 (2011), pp. 3634–3641. ISSN: 1616301X. DOI: 10.1002/adfm.201100443. arXiv: 0706.1062v1.

[31] M. Sistaninia and O. Kolednik. “Improving strength and toughness of materials by utilizing spatial variations of the yield stress.” In: *Acta Materialia* 122 (2017), pp. 207–219. ISSN: 13596454. DOI: 10.1016/j.actamat.2016.09.044.

[32] C. R. Chen, J. Pascual, F. D. Fischer, O. Kolednik, and R. Danzer. “Prediction of the fracture toughness of a ceramic multilayer composite - Modeling and experiments.” In: *Acta Materialia* 55.2 (2007), pp. 409–421. ISSN: 13596454. DOI: 10.1016/j.actamat.2006.07.046.

[33] H. Adachi and K. Wasa. “1 - Thin Films and Nanomaterials BT - Handbook of Sputtering Technology (Second Edition).” In: Oxford: William Andrew Publishing, 2012, pp. 3–39. ISBN: 978-1-4377-3483-6. DOI: `https://doi.org/10.1016/B978-1-4377-3483-6.00001-2`.

[34] R. Treml, D. Kozic, J. Zechner, X. Maeder, B. Sartory, H. P. Gänser, R. Schöngrundner, J. Michler, R. Brunner, and D. Kiener. “High resolution determination of local residual stress gradients in single- and multilayer thin film systems.” In: *Acta Materialia* 103 (2016), pp. 616–623. DOI: `10.1016/j.actamat.2015.10.044`.

[35] J. J. Wortman and R. A. Evans. “Young’s modulus, shear modulus, and poisson’s ratio in silicon and germanium.” In: *Journal of Applied Physics* 36.1 (1965), pp. 153–156. ISSN: 00218979. DOI: `10.1063/1.1713863`.

[36] S. W. Bedell, A. Reznicek, K. Fogel, J. Ott, and D. K. Sadana. “Strain and lattice engineering for Ge FET devices.” In: *Materials Science in Semiconductor Processing* 9.4-5 SPEC. ISS. (2006), pp. 423–436. ISSN: 13698001. DOI: `10.1016/j.mssp.2006.08.001`.

[37] K. Matoy, H. Schönherr, T. Detzel, T. Schöberl, R. Pippan, C. Motz, and G. Dehm. “A comparative micro-cantilever study of the mechanical behavior of silicon based passivation films.” In: *Thin Solid Films* 518.1 (2009), pp. 247–256. ISSN: 00406090. DOI: `10.1016/j.tsf.2009.07.143`.

[38] M. A. Hopcroft, W. D. Nix, and T. W. Kenny. “What is the Young’s modulus of silicon?” In: *Journal of Microelectromechanical Systems* 19.2 (2010), pp. 229–238. ISSN: 10577157. DOI: `10.1109/JMEMS.2009.2039697`.

[39] R. Schöngrundner, R. Treml, T. Antretter, D. Kozic, W. Ecker, D. Kiener, and R. Brunner. “Critical assessment of the determination of residual stress profiles in thin films by means of the ion beam layer removal method.” In: *Thin Solid Films* 564 (2014), pp. 321–330. DOI: `10.1016/j.tsf.2014.06.003`.

[40] P. G. Sanders, J. A. Eastman, and J. R. Weertman. “Elastic and tensile behavior of nanocrystalline copper and palladium.” In: *Acta materialia* 45.10 (1997), pp. 4019–4025. ISSN: 13596454. DOI: `http://dx.doi.org/10.1016/S1359-6454(97)00092-X`.

[41] S. R. Agnew and J. R. Weertman. “The influence of texture on the elastic properties of ultrafine-grain copper.” In: *Materials Science and Engineering: A* 242.1-2 (1998), pp. 174–180. ISSN: 09215093. DOI: `10.1016/S0921-5093(97)00504-2`.

[42] H. Huang and F. Spaepen. “Tensile testing of free-standing Cu, Ag and Al thin films and Ag/Cu multilayers.” In: *Acta Materialia* 48.12 (2000), pp. 3261–3269. ISSN: 13596454. DOI: `10.1016/S1359-6454(00)00128-2`.

[43] D. Kozic, R. Treml, R. Schöngrundner, R. Brunner, D. Kiener, T. Antretter, and H.-P. Gänser. “Evaluation of the residual stress distribution in thin films by means of the ion beam layer removal method.” In: *2014 15th International Conference on*

*Thermal, Mechanical and Multi-Physics Simulation and Experiments in Microelectronics and Microsystems, EuroSimE 2014*. 2014. ISBN: 9781479947904. DOI: 10.1109/EuroSimE.2014.6813785.

[44] W. D. Nix. "Mechanical properties of thin films." In: *Metallurgical Transactions A* 20.11 (1989), pp. 2217–2245. ISSN: 03602133. DOI: 10.1007/BF02666659.

[45] A. Moridi, H. Ruan, L. C. Zhang, and M. Liu. "Residual stresses in thin film systems: Effects of lattice mismatch, thermal mismatch and interface dislocations." In: *International Journal of Solids and Structures* 50.22-23 (2013), pp. 3562–3569. ISSN: 00207683. DOI: 10.1016/j.ijsolstr.2013.06.022.

[46] F. Takali, A. Njeh, H. Fuess, and M. H. Ben Ghozlen. "X-ray diffraction measurement of residual stress in epitaxial ZnO/alpha-Al2O3 thin film." In: *Mechanics Research Communications* 38.3 (2011), pp. 186–191. ISSN: 00936413. DOI: 10.1016/j.mechrescom.2011.02.008.

[47] V. Hauk. "Structural and residual stress analysis by nondestructive methods." In: *Institute of Materials, London, UK* (1997), p. 655. ISSN: 1098-6596. DOI: http://dx.doi.org/10.1016/B978-044482476-9/50000-1.

[48] L.B. Freund and S. Suresh. *Thin Film Materials: Stress, Defect Formation and Surface Evolution*. Cambridge University Press, 2008. ISBN: 9780521529778.

[49] X. Zheng, J. Li, and Y. Zhou. "X-ray diffraction measurement of residual stress in PZT thin films prepared by pulsed laser deposition." In: *Acta Materialia* 52.11 (2004), pp. 3313–3322. ISSN: 13596454. DOI: 10.1016/j.actamat.2004.02.047.

[50] C. H. Ma, J. H. Huang, and Haydn Chen. "Residual stress measurement in textured thin film by grazing-incidence X-ray diffraction." In: *Thin Solid Films* 418.2 (2002), pp. 73–78. ISSN: 00406090. DOI: 10.1016/S0040-6090(02)00680-6.

[51] E. Bemporad, M. Brisotto, L. E. Depero, M. Gelfi, A. M. Korsunsky, A. J G Lunt, and M. Sebastiani. "A critical comparison between XRD and FIB residual stress measurement techniques in thin films." In: *Thin Solid Films*. Vol. 572. 2014, pp. 224–231. DOI: 10.1016/j.tsf.2014.09.053.

[52] M. Tkadletz, J. Keckes, N. Schalk, I. Krajinovic, M. Burghammer, C. Czettl, and C. Mitterer. "Residual stress gradients in alpha-Al2O3 hard coatings determined by pencil-beam X-ray nanodiffraction: The influence of blasting media." In: *Surface and Coatings Technology* 262 (2015), pp. 134–140. ISSN: 02578972. DOI: 10.1016/j.surfcoat.2014.12.028.

[53] M. Stefenelli, R. Daniel, W. Ecker, D. Kiener, J. Todt, A. Zeilinger, C. Mitterer, M. Burghammer, and J. Keckes. "X-ray nanodiffraction reveals stress distribution across an indented multilayered CrN-Cr thin film." In: *Acta Materialia* 85 (2015), pp. 24–31. ISSN: 13596454. DOI: 10.1016/j.actamat.2014.11.011.

[54] M. Deluca, R. Hammer, J. Keckes, J. Kraft, F. Schrank, J. Todt, O. Robach, J.-S. Micha, and S. Defregger. "Integrated experimental and computational approach for residual stress investigation near through-silicon vias." In: *Journal of Applied Physics* 120.19 (2016), p. 195104. ISSN: 0021-8979. DOI: `10.1063/1.4967927`.

[55] A. J. G. Lunt and A. M. Korsunsky. "A review of micro-scale focused ion beam milling and digital image correlation analysis for residual stress evaluation and error estimation." In: *Surface and Coatings Technology* 283 (2015), pp. 373–388. ISSN: 02578972. DOI: `10.1016/j.surfcoat.2015.10.049`.

[56] X. Song, K. B. Yeap, J. Zhu, J. Belnoue, M. Sebastiani, E. Bemporad, K. Y. Zeng, and A. M. Korsunsky. "Residual stress measurement in thin films using the semi-destructive ring-core drilling method using Focused Ion Beam." In: *Procedia Engineering*. Vol. 10. 2011, pp. 2190–2195. DOI: `10.1016/j.proeng.2011.04.362`.

[57] X. Song, K. B. Yeap, J. Zhu, J. Belnoue, M. Sebastiani, E. Bemporad, K. Zeng, and A. M. Korsunsky. "Residual stress measurement in thin films at sub-micron scale using Focused Ion Beam milling and imaging." In: *Thin Solid Films* 520.6 (2012), pp. 2073–2076. ISSN: 00406090. DOI: `10.1016/j.tsf.2011.10.211`.

[58] J. Keller, A. Gollhardt, D. Vogel, E. Auerswald, N. Sabate, J. Auersperg, and B. Michel. "FibDAC - Residual Stress Determination by Combination of Focused Ion Beam Technique and Digital Image Correlation." In: *Materials Science Forum* 524-525 (2006), pp. 121–126. ISSN: 1662-9752. DOI: `10.4028/www.scientific.net/MSF.524-525.121`.

[59] A. M. Korsunsky, M. Sebastiani, and E. Bemporad. "Residual stress evaluation at the micrometer scale: Analysis of thin coatings by FIB milling and digital image correlation." In: *Surface and Coatings Technology* 205.7 (2010), pp. 2393–2403. ISSN: 02578972. DOI: `10.1016/j.surfcoat.2010.09.033`.

[60] M. Krottenthaler, C. Schmid, J. Schaufler, K. Durst, and M. Göken. "A simple method for residual stress measurements in thin films by means of focused ion beam milling and digital image correlation." In: *Surface and Coatings Technology* 215 (2013), pp. 247–252. ISSN: 02578972. DOI: `10.1016/j.surfcoat.2012.08.095`.

[61] M. Sebastiani, C. Eberl, E. Bemporad, and G. M. Pharr. "Depth-resolved residual stress analysis of thin coatings by a new FIB-DIC method." In: *Materials Science and Engineering A* 528.27 (2011), pp. 7901–7908. ISSN: 09215093. DOI: `10.1016/j.msea.2011.07.001`.

[62] D. Kiener, C. Motz, M. Rester, M. Jenko, and G. Dehm. "FIB damage of Cu and possible consequences for miniaturized mechanical tests." In: *Materials Science and Engineering A* 459.1-2 (2007), pp. 262–272. ISSN: 09215093. DOI: `10.1016/j.msea.2007.01.046`.

[63] B. Pan, K. Qian, H. Xie, and A. Asundi. “Two-dimensional digital image correlation for in-plane displacement and strain measurement: a review.” In: *Measurement Science and Technology* 20.6 (2009), p. 062001. ISSN: 0957-0233. DOI: `10.1088/0957-0233/20/6/062001`.

[64] B. Pan, L. Yu, D. Wu, and L. Tang. “Systematic errors in two-dimensional digital image correlation due to lens distortion.” In: *Optics and Lasers in Engineering* 51.2 (2013), pp. 140–147. ISSN: 01438166. DOI: `10.1016/j.optlaseng.2012.08.012`.

[65] S. Massl, J. Keckes, and R. Pippan. “A direct method of determining complex depth profiles of residual stresses in thin films on a nanoscale.” In: *Acta Materialia* 55.14 (2007), pp. 4835–4844. ISSN: 13596454. DOI: `10.1016/j.actamat.2007.05.002`.

[66] S. Timoshenko. *History of Strength of Materials*. 1983, p. 452. ISBN: 0486611876. DOI: `10.1016/0022-5096(54)90010-1`.

[67] L. M. Jiang, J. Peng, Y. G. Liao, Y. C. Zhou, J. Liang, H. X. Hao, and C. Lu. “A modified layer-removal method for residual stress measurement in electrodeposited nickel films.” In: *Thin Solid Films* 519.10 (2011), pp. 3249–3253. ISSN: 00406090. DOI: `10.1016/j.tsf.2011.01.260`.

[68] K. Levenberg. “A Method for the Solution of Certain Problems in Least Squares.” In: *Quart. Appl. Math.* Vol. 2. 2. 1944, pp. 164–168. DOI: `citeulike-article-id:2946351`.

[69] D. W. Marquardt. “An Algorithm for Least-Squares Estimation of Nonlinear Parameters.” In: *Journal of the Society for Industrial and Applied Mathematics* 11.2 (1963), pp. 431–441. ISSN: 0368-4245. DOI: `10.1137/0111030`.

[70] R. Treml, D. Kozic, R. Schöngrundner, O. Kolednik, H.-P. Gänser, R. Brunner, and D. Kiener. “Miniaturized fracture experiments to determine the toughness of individual films in a multilayer system.” In: *Extreme Mechanics Letters* 8 (2016), pp. 235–244. ISSN: 23524316. DOI: `10.1016/j.eml.2016.01.004`.

[71] D. Kozic, V. Maier-Kiener, R. Konetschnik, H.-P. Gänser, T. Antretter, R. Brunner, and D. Kiener. “Extracting flow curves from nano-sized metal layers in thin film systems.” In: *Scripta Materialia* 130 (2017), pp. 143–147. ISSN: 13596462. DOI: `10.1016/j.scriptamat.2016.11.008`.

[72] M. D. Uchic, D. M. Dimiduk, J. N. Florando, and W. D. Nix. “Sample dimensions influence strength and crystal plasticity.” In: *Science* 305.5686 (2004), pp. 986–989. ISSN: 1095-9203. DOI: `10.1126/science.1098993`.

[73] J. R. Greer and J. T. M. De Hosson. “Plasticity in small-sized metallic systems: Intrinsic versus extrinsic size effect.” In: *Progress in Materials Science*. Vol. 56. 6. 2011, pp. 654–724. ISBN: 00796425 (ISSN). DOI: `10.1016/j.pmatsci.2011.01.005`.

[74] A. Pineau, A. Amine Benzerga, and T. Pardoen. “Failure of metals III: Fracture and fatigue of nanostructured metallic materials.” In: *Acta Materialia* 107 (2016), pp. 508–544. ISSN: 13596454. DOI: `10.1016/j.actamat.2015.07.049`.

[75] J. R. Greer, W. C. Oliver, and W. D. Nix. “Size dependence of mechanical properties of gold at the micron scale in the absence of strain gradients.” In: *Acta Materialia* 53.6 (2005), pp. 1821–1830. ISSN: 13596454. DOI: `10.1016/j.actamat.2004.12.031`.

[76] D. Kiener, C. Motz, W. Grosinger, D. Weygand, and R. Pippan. “Cyclic response of copper single crystal micro-beams.” In: *Scripta Materialia* 63.5 (2010), pp. 500–503. ISSN: 13596462. DOI: `10.1016/j.scriptamat.2010.05.014`.

[77] C. S. Pande and K. P. Cooper. “Nanomechanics of Hall-Petch relationship in nanocrystalline materials.” In: *Progress in Materials Science* 54.6 (2009), pp. 689–706. ISSN: 00796425. DOI: `10.1016/j.pmatsci.2009.03.008`.

[78] E. O. Hall. “The deformation and ageing of mild steel III Discussion of results.” In: *Proceedings of the Physical Society. Section B* 64.9 (1951), p. 747. ISSN: 0370-1301. DOI: `10.1088/0370-1301/64/9/303`.

[79] N. J. Petch. “The cleavage strength of polycrystals.” In: *J. Iron Steel Inst* 174.19 (1953), pp. 25 –28. ISSN: 00354511. DOI: `10.1007/BF01972547`.

[80] E. Arzt. “Size Effects in Materials Due To Microstructural and Dimensional Constraints : a Comparative Review.” In: *Acta Materialia* 46.16 (1998), pp. 5611–5662. ISSN: 13596454. DOI: `10.1016/S0957-5820(99)70836-0`.

[81] J. Y. Kim, D. Jang, and J. R. Greer. “Tensile and compressive behavior of tungsten, molybdenum, tantalum and niobium at the nanoscale.” In: *Acta Materialia* 58.7 (2010), pp. 2355–2363. ISSN: 13596454. DOI: `10.1016/j.actamat.2009.12.022`.

[82] M. Hommel and O. Kraft. “Deformation behavior of thin copper films on deformable substrates.” In: *Acta Materialia* 49.19 (2001), pp. 3935–3947. ISSN: 13596454. DOI: `10.1016/S1359-6454(01)00293-2`.

[83] C. Motz, T. Schöberl, and R. Pippan. “Mechanical properties of micro-sized copper bending beams machined by the focused ion beam technique.” In: *Acta Materialia* 53.15 (2005), pp. 4269–4279. ISSN: 13596454. DOI: `10.1016/j.actamat.2005.05.036`.

[84] M. A. Meyers, A. Mishra, and D. J. Benson. “Mechanical properties of nanocrystalline materials.” In: *Progress in Materials Science* 51.4 (2006), pp. 427–556. ISSN: 00796425. DOI: `10.1016/j.pmatsci.2005.08.003`.

[85] Y. M. Wang, K. Wang, D. Pan, K. Lu, K. J. Hemker, and E. Ma. “Microsample tensile testing of nanocrystalline copper.” In: *Scripta Materialia* 48.12 (2003), pp. 1581–1586. ISSN: 13596462. DOI: `10.1016/S1359-6462(03)00159-3`.

[86] A. Rinaldi, P. Peralta, C. Friesen, and K. Sieradzki. "Sample-size effects in the yield behavior of nanocrystalline nickel." In: *Acta Materialia* 56.3 (2008), pp. 511–517. ISSN: 13596454. DOI: `10.1016/j.actamat.2007.09.044`.

[87] D. Jang and J. R. Greer. "Size-induced weakening and grain boundary-assisted deformation in 60 nm grained Ni nanopillars." In: *Scripta Materialia* 64.1 (2011), pp. 77–80. ISSN: 13596462. DOI: `10.1016/j.scriptamat.2010.09.010`.

[88] M.D. Kriese, N.R. Moody, and W.W. Gerberich. "Effects of annealing and interlayers on the adhesion energy of copper thin films to SiO2/Si substrates." In: *Acta Materialia* 46.18 (1998), pp. 6623–6630. ISSN: 13596454. DOI: `10.1016/S1359-6454(98)00277-8`.

[89] N.I. Tymiak, A.A. Volinsky, M.D. Kriese, S.A. Downs, and W.W. Gerberich. "The role of plasticity in bimaterial fracture with ductile interlayers." In: *Metallurgical and Materials Transactions A: Physical Metallurgy and Materials Science* 31.3 (2000). DOI: `10.1007/s11661-000-0030-5`.

[90] R. Saha and W. D. Nix. "Effects of the substrate on the determination of thin film mechanical properties by nanoindentation." In: *Acta Materialia* 50.1 (2002), pp. 23–38. ISSN: 13596454. DOI: `10.1016/S1359-6454(01)00328-7`.

[91] J. N. Florando and W. D. Nix. "A microbeam bending method for studying stress-strain relations for metal thin films on silicon substrates." In: *Journal of the Mechanics and Physics of Solids* 53.3 (2005), pp. 619–638. ISSN: 00225096. DOI: `10.1016/j.jmps.2004.08.007`.

[92] M. A. Tschopp, H. A. Murdoch, L. J. Kecskes, and K. A. Darling. *Bulk nanocrystalline metals: Review of the current state of the art and future opportunities for copper and copper alloys*. 2014. DOI: `10.1007/s11837-014-0978-z`.

[93] F. W. Smith and J. Hashemi. *Foundations of Materials Science and Engineering*. fourth ed. New York: McGraw Hill, 2006. ISBN: 9780072921946.

[94] D. Kozic, R. Treml, R. Schöngrundner, R. Brunner, D. Kiener, J. Zechner, T. Antretter, and H.-P. Gänser. "Fracture mechanics of thin film systems on the sub-micron scale." In: *2015 16th International Conference on Thermal, Mechanical and Multi-Physics Simulation and Experiments in Microelectronics and Microsystems, EuroSimE 2015*. 2015. ISBN: 9781479999507. DOI: `10.1109/EuroSimE.2015.7103088`.

[95] D. Kozic, R. Treml, V. Maier-Kiener, R. Schöngrundner, R. Brunner, D. Kiener, T. Antretter, and H.-P. Gänser. "Fracture and material behavior of thin film composites." In: *2016 17th International Conference on Thermal, Mechanical and Multi-Physics Simulation and Experiments in Microelectronics and Microsystems, EuroSimE 2016*. 2016. ISBN: 9781509021062. DOI: `10.1109/EuroSimE.2016.7463352`.

[96] D. Kozic, H.-P. Gänser, R. Brunner, D. Kiener, T. Antretter, and O. Kolednik. "Crack arresting abilities of thin metalic films stacks due to the influence of material and residual stress inhomogeneities." In: *TBA* (2018).

[97] S. Suresh, Y. Sugimura, and T. Ogawa. "Fatigue cracking in materials with brittle surface coatings." In: *Scripta Metallurgica et Materiala* 29.2 (1993), pp. 237–242. ISSN: 0956716X. DOI: `10.1016/0956-716X(93)90315-J`.

[98] R. Pippan, K. Flechsig, and F. O. Riemelmoser. "Fatigue crack propagation behavior in the vicinity of an interface between materials with different yield stresses." In: *Materials Science and Engineering A* 283.1-2 (2000), pp. 225–233. ISSN: 09215093. DOI: `10.1016/S0921-5093(00)00703-6`.

[99] P. Fratzl, H. S. Gupta, F. D. Fischer, and O. Kolednik. "Hindered crack propagation in materials with periodically varying young's modulus - Lessons from biological materials." In: *Advanced Materials* 19.18 (2007), pp. 2657–2661. ISSN: 09359648. DOI: `10.1002/adma.200602394`.

[100] J. Zechner and O. Kolednik. "Paper multilayer with a fracture toughness of steel." In: *Journal of Materials Science* 48.15 (2013), pp. 5180–5187. ISSN: 00222461. DOI: `10.1007/s10853-013-7304-y`.

[101] F. Keulemans, P. Palav, M. M. N. Aboushelib, A. van Dalen, C. J. Kleverlaan, and A. J. Feilzer. "Fracture strength and fatigue resistance of dental resin-based composites." In: *Dental Materials* 25.11 (2009), pp. 1433–1441. ISSN: 01095641. DOI: `10.1016/j.dental.2009.06.013`.

[102] L. S. Dimas, G. H. Bratzel, I. Eylon, and M. J. Buehler. "Tough composites inspired by mineralized natural materials: Computation, 3D printing, and testing." In: *Advanced Functional Materials* 23.36 (2013), pp. 4629–4638. ISSN: 1616301X. DOI: `10.1002/adfm.201300215`.

[103] Q. H. Qin and X. Zhang. "Crack deflection at an interface between dissimilar piezoelectric materials." In: *International Journal of Fracture* 102.4 (2000), pp. 355–370. ISSN: 03769429. DOI: `10.1023/A:1007601312977`.

[104] L. Guo, T. Kitamura, Y. Yan, T. Sumigawa, and K. Huang. "Fracture mechanics investigation on crack propagation in the nano-multilayered materials." In: *International Journal of Solids and Structures* 64 (2015), pp. 208–220. ISSN: 00207683. DOI: `10.1016/j.ijsolstr.2015.03.025`.

[105] P. Fratzl, O. Kolednik, F. D. Fischer, and M. N. Dean. "The mechanics of tessellations – bioinspired strategies for fracture resistance." In: *Chem. Soc. Rev.* 45 (2015), pp. 252–267. ISSN: 0306-0012. DOI: `10.1039/C5CS00598A`.

[106] U. G. K. Wegst, H. Bai, E. Saiz, A. P. Tomsia, R. O. Ritchie, C. Ortiz, and M. Boyce. "Bioinspired structural materials." In: *Nature Materials* 14.1 (2014), pp. 23–36. ISSN: 1476-1122. DOI: `10.1038/nmat4089`.

[107] M. Sistaninia and O. Kolednik. "Effect of a single soft interlayer on the crack driving force." In: *Engineering Fracture Mechanics* 130 (2014), pp. 21–41. ISSN: 00137944. DOI: `10.1016/j.engfracmech.2014.02.026`.

[108] R. Bermejo, Y. Torres, A. J. Sanchez-Herencia, C. Baudin, M. Anglada, and L. Llanes. "Residual stresses, strength and toughness of laminates with different layer thickness ratios." In: *Acta Materialia* 54.18 (2006), pp. 4745–4757. ISSN: 13596454. DOI: 10.1016/j.actamat.2006.06.008.

[109] X. B. Ren, Z. L. Zhang, and B. Nyhus. "Effect of residual stresses on ductile crack growth resistance." In: *Engineering Fracture Mechanics* 77.8 (2010), pp. 1325–1337. ISSN: 00137944. DOI: 10.1016/j.engfracmech.2010.03.007.

[110] C. D. M. Liljedahl, J. Brouard, O. Zanellato, J. Lin, M. L. Tan, S. Ganguly, P. E. Irving, M. E. Fitzpatrick, X. Zhang, and L. Edwards. "Weld residual stress effects on fatigue crack growth behaviour of aluminium alloy 2024-T351." In: *International Journal of Fatigue* 31.6 (2009), pp. 1081–1088. ISSN: 0142-1123. DOI: 10.1016/j.ijfatigue.2008.05.008.

[111] J. Maierhofer, R. Pippan, and H.-P. Gänser. "Modified NASGRO Equation for Short Cracks and Application to the Fitness-for-purpose Assessment of Surface-treated Components." In: *Procedia Materials Science* 3 (2014), pp. 930–935. ISSN: 2211-8128. DOI: http://dx.doi.org/10.1016/j.mspro.2014.06.151.

[112] R. Mueller, S. Kolling, and D. Gross. "On configurational forces in the context of the finite element method." In: *International Journal for Numerical Methods in Engineering* 53.7 (2002), pp. 1557–1574. ISSN: 1097-0207. DOI: 10.1002/nme.351. URL: http://dx.doi.org/10.1002/nme.351.

[113] R. Mueller, D. Gross, and G. A. Maugin. "Use of material forces in adaptive finite element methods." In: *Computational Mechanics* 33.6 (2004), pp. 421–434. ISSN: 1432-0924. DOI: 10.1007/s00466-003-0543-z. URL: http://dx.doi.org/10.1007/s00466-003-0543-z.